Ersatz

Internal Report
DESY F35D-94-01
February 1994

A Measurement of the Total Photon-Proton Cross Section in the Center of Mass Energy Range 167 to 194 GeV

by

B. D. Burow

"Die Verantwortung für den Inhalt dieses
Internen Berichtes liegt ausschließlich beim Verfasser"

A Measurement of the Total Photon-Proton Cross Section in the Center of Mass Energy Range 167 to 194 GeV

by

Burkhard D. Burow

A thesis submitted in conformity with the requirements
for the degree of Doctor of Philosophy
Graduate Department of Physics
University of Toronto

A Measurement of the Total Photon-Proton Cross Section in the Center of Mass Energy Range 167 to 194 GeV

by

Burkhard D. Burow

A thesis submitted in conformity with the requirements
for the degree of Doctor of Philosophy
Graduate Department of Physics
University of Toronto

Abstract

The thesis is a complete presentation of a total photon-proton (γp) cross section measurement using the ZEUS detector at the recently commissioned HERA electron-proton (ep) collider. A measurement of γp interactions using the exchanged virtual photon of ep collisions is shown to be justified and the correct flux of photons is determined. HERA and ZEUS are introduced, with an emphasis on the components used in the measurement. The data was collected during the fall of 1992 for which the experimental conditions are described, including the determination of the 13 nb^{-1} of integrated ep luminosity which provided the event sample. The treatment of background events is described, as are event losses due to inefficiencies in their identification by the trigger and in their subsequent analysis. The observed number of events is corrected for the acceptance of the experiment using Monte Carlo simulations of γp interactions tuned to match characteristics of the observed events. Radiative corrections to the measurement are shown to be small and the calculation is corroborated by a measurement of the number of radiative events. In the γp center of mass energy range $167 < W < 194$ GeV, the total γp cross section is $\sigma_{tot}^{\gamma p} = 143 \pm 3$ (stat.) ± 18 (syst.) μb.

Table of Contents

List of Figures

List of Tables

1 Introduction

Particle physics is the study of the ultimate constituents of matter and their interactions. A large fraction of the present understanding has been gained from observations on the interaction between two particles in collision. Following a decade of preparation, 1992 marked the beginning of a novel and promising experimental era with the first results from the ZEUS[1] and H1[2] collaborations at the electron-proton (ep) collider HERA[3] at DESY (Deutsches Elektronen-SYnchrotron), Hamburg, Germany. By colliding a beam of 26.7 GeV electrons head-on with one of 820 GeV protons, HERA creates ep interactions with a center of mass energy $\sqrt{s} = 296$ GeV, an order of magnitude higher than observed previously. As introduced in Section 1.1, a fraction of the ep interactions have a straightforward interpretation as photon-proton (γp) interactions and may have a center of mass energy up to $W \sim \sqrt{s}$, again an order of magnitude higher than those of previous observations.

Measurements of γp interactions have indicated a hadronlike behavior for the photon. An overview of the γp data is given in [4], as are examples of the similarities between γp and hadron-hadron collisions. These include the energy dependence of the total cross section and the angular distribution of the products of the interaction. Regge theory [5] provides a simple and economical description of the energy dependence of the total hadron-hadron cross sections [6]. Below $W \sim 10$ GeV, the total γp cross section ($\sigma_{tot}^{\gamma p}$) decreases with energy, as do the total hadron-hadron cross sections (σ_{tot}^{hh}) in this energy range. Above $W \sim 10$ GeV, σ_{tot}^{hh} rises with energy and as expected, $\sigma_{tot}^{\gamma p}$ follows this behavior [7]. At the highest energy of previous measurements, $W = 18$ GeV, $\sigma_{tot}^{\gamma p} = 118$ μb [7].

Considerable interest in $\sigma_{tot}^{\gamma p}$ for $W \gtrsim 100$ GeV has arisen in the search for an explanation of the anomalously high muon content in cosmic ray air showers associated with an astrophysical point source such as Cygnus X-3[8], Hercules X-1[9] or the Crab Nebula[10]. Although numerous experiments each provide some evidence that particles with energy greater than 100 TeV are emitted from these and other extraterrestrial point sources, none of the individual experiments provides unambiguous proof [11]. Even less conclusive is the present experimental ability to measure the air shower characteristics and thus determine the identity of the emitted particle [11]. If the observations are valid, the original particle emitted by the point source must be uncharged in order to traverse the galactic magnetic field undeflected and thus produce a shower in the direction of the source. The original particle must obviously have a long life time. The showers are observed with a precise period. This requires the original particle to travel very close to the speed of light, regardless of energy, and thus to have little to no mass, for example, < 60 MeV [9]. Neutrinos are ruled out due to their low cross section, leaving the photon as the only known candidate. The photon is expected to have an electromagnetic shower in the atmosphere, producing mainly electrons and photons. Instead, the showers due to these point sources are observed with a large muon content,

very similar to the usual high energy cosmic rays, which are hadrons. Therefore, a yet unknown type of particle may originate from the point sources. But, if $\sigma_{tot}^{\gamma p}$ is very large at high W, approaching the cross section of the electromagnetic shower, $\sigma_{\gamma p \to e^+e^-p} \sim 10^4$ μb, the γp interactions can produce enough pions, which decay to muons, to explain the observed showers [12]. Thus, the point sources may indeed be emitting photons.

Mini-jets models [13] of hadron-hadron interactions (see Sections 3.2.4 and 3.3) offer the possibility that $\sigma_{tot}^{\gamma p}$ rises rapidly as W increases beyond the 18 GeV of previous measurements. The discussion in [14] summarizes the mini-jet possibilities, including predictions that $\sigma_{tot}^{\gamma p} \approx 200$ μb at HERA energies. The possible rise for $\sigma_{tot}^{\gamma p}$ with W is tempered by the measured total proton-antiproton cross section which rises with energy at only a moderate rate up to a center of mass energy of 1800 GeV [6].

In addition to the previously observed hadronlike behavior of the photon (see Section 3.2), the increase in W over that of previous experiments may allow γp interactions at HERA to show significant contributions from the anomalous (see Section 3.3) and/or the direct (see Section 3.4) parts of the pointlike photon.

Therefore, among the eagerly awaited results from the first running period of HERA, in the summer of 1992, were 97 ep events observed by the ZEUS detector which allowed the total photon-proton cross section to be determined as $\sigma_{tot}^{\gamma p} = 154 \pm 16$ (stat.) ± 32 (syst.) μb in the γp center of mass energy range $186 < W < 233$ GeV [14]. The corresponding measurement by the H1 collaboration is $\sigma_{tot}^{\gamma p} = 159 \pm 7$ (stat.) ± 20 (syst.) μb with $\langle W \rangle = 195$ GeV [15]. Despite large statistical and systematic errors, the ZEUS and H1 measurements rule out a major increase in $\sigma_{tot}^{\gamma p}$ at HERA energies. The measurement is consistent with the DL[16] and ALLM[17] models, both inspired by Regge theory, which predict a moderate rise for $\sigma_{tot}^{\gamma p}$, as observed in the highest energy proton-antiproton collisions [6].

With the mini-jet models restricted to a moderate rise for $\sigma_{tot}^{\gamma p}$ at HERA energies, they appear to be unable to explain the anomalous muon content in cosmic ray air showers associated with astrophysical point sources [18]. The nature of these observations remains unresolved.

This thesis presents a more precise measurement of $\sigma_{tot}^{\gamma p}$ for $167 < W < 194$ GeV, using data collected by ZEUS during the fall 1992 running period of HERA. The basis for the measurement is introduced below. The full presentation then proceeds as outlined in the abstract. A glossary of terms and acronyms is appended.

1.1 Photon-Proton Interactions at HERA

In ep collisions which scatter the electron by only a small angle, the electron and proton exchange a photon (γ^*) which is only slightly virtual. The interaction may be expressed as

$$ep \rightarrow e' + \gamma^* p \tag{1-1}$$

$$\text{with } \gamma^* p \rightarrow H. \tag{1-2}$$

Since (1-1) is well understood, (1-2) can be used to measure the properties of photoproduction interaction $\gamma p \rightarrow H$, if the behavior of the exchanged virtual photon γ^* can be shown to be the same as that of a real photon γ.

In this thesis, the nature of the final hadronic system (H) is examined using the energy distribution of the event observed by the calorimeter (CAL divided into FCAL, BCAL and RCAL) of the central ZEUS detector. As demonstrated in Figure 1-1, a suitable sample of **tagged photoproduction** events was collected by requiring the scattered electron (e') to be observed in the electron calorimeter (LUMIE) of the luminosity monitor and energy from the final hadronic system to be observed in RCAL.

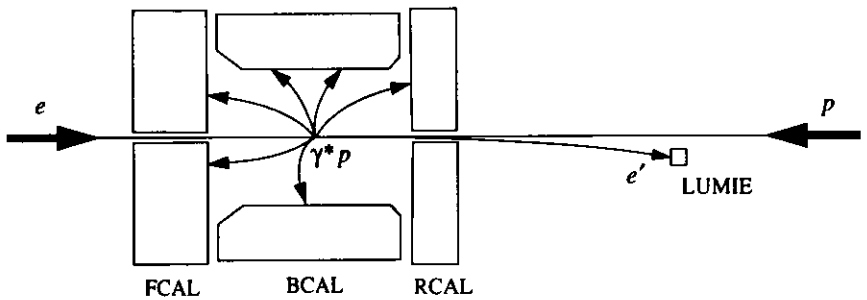

Figure 1-1 Schematic view of tagged photoproduction at ZEUS.
The colliding e- and p-beams of HERA produce the interaction $ep \rightarrow e' + \gamma^* p$. The lightly scattered electron (e') escapes the ZEUS central detector via the beam pipe and is observed by LUMIE. The particles of the virtual $\gamma^* p$ interaction are observed in FCAL, BCAL, and RCAL of the central detector. In this thesis, the tagged photoproduction events are required to have energy deposited in RCAL.

The measurement of the scattered electron energy (E_{LUMIE}) tags the energy of the exchanged photon as

$$E_{\gamma^*} = E_e - E_{LUMIE}, \tag{1-3}$$

where E_e = 26.7 GeV is the electron beam energy. The cross section measurement is restricted to tagged photoproduction events with $15.2 < E_{LUMIE} < 18.2$ GeV, corresponding to 8.5 – 11.5 GeV photons, which collide with the 820 GeV protons at a center of mass energy of $167 < W < 194$ GeV.

1.2 The Total Photoproduction Cross Section

A cross section expresses the probability for an interaction to occur. The measured cross section for $ep \rightarrow e'H$ is given by

$$\sigma^{ep}_{measured} = \frac{N_{tagged\ php.} / [A_{LUMIE} A_{RCAL} (1+\Delta)(1+\delta)]}{L_{int}}. \tag{1-4}$$

The numerator is the number of measured ep interactions, including corrections for experimental effects. The denominator is a measure of the number of possible interactions from all the examined crossings of the HERA electron and proton beams. The number of tagged photoproduction events ($N_{tagged\ php.}$) observed has a corresponding integrated luminosity (L_{int}) delivered by HERA. The acceptance of e' and H in LUMIE and RCAL is A_{LUMIE} and A_{RCAL}, respectively. The correction Δ is for the known effects of backgrounds and inefficiencies. The radiative corrections are given by δ.

The measured ep cross section, referring to the complete interaction of (1-1) and (1-2), may be interpreted as

$$\sigma^{ep}_{measured} = F^{e}_{\gamma} \sigma^{\gamma p}_{tot}, \tag{1-5}$$

where F^{e}_{γ} and $\sigma^{\gamma p}_{tot}$ correspond to the separate probabilities of the interactions in (1-1) and (1-2), respectively. F^{e}_{γ} may be considered to be the flux of photons accompanying the electron. It may be calculated from theory, and thus $\sigma^{\gamma p}_{tot}$ may be determined.

2 Relating Electron-Proton and Photon-Proton Cross Sections

Photoproduction, where a target particle is struck by a photon, can be measured in electroproduction, where the target is struck by an electron.

> "The close relation between the interactions produced by a moving charged particle and those due to incident electromagnetic waves was first pointed out in 1924 by Fermi [19], who related stopping power for α particles to the electromagnetic properties of the material. Weizsäcker and Williams [20] later considered particularly the case of relativistic electrons. By making a Fourier analysis of the field produced at a given point by a passing electron ..., they showed that this field contained predominantly transverse components and concluded that an incident electron would produce the same effects as a beam of photons with spectrum ..." [21]

Therefore the electromagnetic interaction, to lowest order via an exchanged virtual photon, between a colliding electron and proton can be reduced to the interaction of the proton with a photon from the electron.

After introducing electron-proton (ep) interactions and kinematics, the relationship between electroproduction and photoproduction will be derived using approximations valid at HERA.

2.1 Electron-Proton Interactions

In quantum theory, the interaction between two particles is viewed in terms of the exchange of specific quanta (gauge bosons) associated with the particular type of interaction. In the Standard Model (SM) of elementary particle physics, ep interaction occur to first order via an exchanged gauge boson as illustrated in Figure 2-1. The incoming electron, e, and proton, P, exchange the

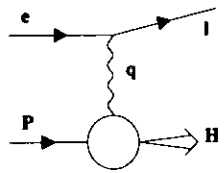

Figure 2-1 The Born term for inelastic ep scattering.

boson, q, thus producing the outgoing scattered lepton, l, and final hadronic system, H. From the conservation of each lepton type in the SM, the scattered lepton may be either an electron or an electron neutrino.

In this text, the symbol used to identify a particle is also used to denote its four-momentum. In ep scattering, the boson transfers a momentum q from the electron to the proton. The four-momentum of the boson is defined by $q \equiv e - l \equiv H - P$ following energy and momentum conservation at each vertex involving the boson. The exchanged boson is **virtual** since it violates energy and momentum conservation as permitted by the Heisenberg Uncertainty Principle during the limited time of the interaction. The degree of virtuality is given by the difference between the mass of the exchanged particle and that of the real particle. For example, an exchanged virtual photon (γ^*) has mass squared

$$m_q^2 \equiv q^2 \equiv \mathrm{E}_q^2 - \vec{p}_q^{\,2} \neq 0 = m_\gamma^2, \tag{2-1}$$

given by the difference in squared energy and momentum, as for any other particle.

The lowest order term of an interaction is known as the Born term, since in the Born approximation the interaction is assumed to be weak, allowing only a single scattering to be considered. The effect of higher order terms for ep scattering is examined in Chapter 12.

2.2 Kinematics

Only two independent variables are needed to define the event kinematics of an ep interaction, given the identity of the scattered lepton. For example, it is sufficient and in the HERA laboratory frame convenient, to refer to the energy, E_l, and angle, ϑ_l, of the scattered lepton. Similarly, the cross section is usually discussed as a double differential. Additional variables are required to describe the details of the final hadronic system.

A short description of a few of the derived kinematic quantities is in order. The ep center of mass energy, $\sqrt{s}$, is the total energy of the ep collision in its rest frame and is therefore the maximum energy available to any process in the collision. The sum of the beam energies minus the center of mass energy, $\mathrm{E}_e + \mathrm{E}_p - \sqrt{s}$, is the kinetic energy of the ep collision. Therefore, in the HERA laboratory frame, the collision and its products are boosted in the direction of the proton beam. The invariant mass of the hadronic system, W, is the center of mass energy of the boson-proton vertex. The Lorentz invariant Bjorken-x and y variables conveniently define the event kinematics. These so-called scaling variables cover the plane $0 \leq (x, y) \leq 1$ for all possible event kinematics. If the ep collision is viewed in a frame where the proton has infinite momentum, x is the fraction of proton momentum involved in the interaction. In a frame where the proton is at rest, y is the fraction of energy lost by the electron in the interaction. The virtuality of the exchanged boson is usually expressed in terms of Q^2, defined by $Q^2 \equiv -q^2 > 0$. At HERA, it is given by $Q^2 = xy\bar{s}$, where the reduced center of mass energy squared $\bar{s}$ is very well approximated by s.

A quick appreciation of the kinematic reach at HERA for $ep \to e'H$ can be gained from Figure 2-2, displaying the values of the variables x, y, and ϑ_l in Q^2, W phase space.

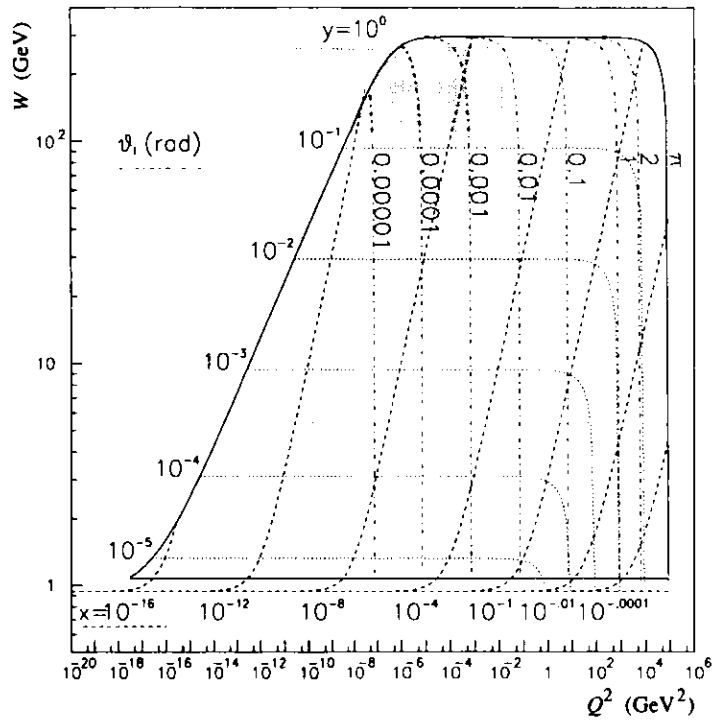

Figure 2-2 Kinematic range for inelastic ep scattering at HERA.
The horizontal dashed line at $W = m_p = 0.938GeV$ is elastic ep scattering. The region for inelastic ep scattering, $ep \rightarrow e'H$, at HERA is surrounded by the solid line, including the horizontal line at $W = m_p + m_{\pi^0}$ for $ep \rightarrow e'p\,\pi^0$. The dotted lines are contours of constant Bjorken-y. The dashed lines are contours of constant Bjorken-x. The dash-dotted lines are contours of constant ϑ_l, the scattering angle of the outgoing electron. The ϑ_l contours follow (2-27), but have ignored the Q^2_{min} term. For example, $\vartheta_l = 0$ when $Q^2 = Q^2_{min}$.
The shaded area shows the geometrical acceptance for the scattered electron in LUMIE (see Section 7.2.1).

Particles from the ep collision with $0.03 \lesssim \theta \lesssim \pi - 0.05$ rad are accepted by the ZEUS central detector (see Section 7.1). Theoretical prejudice (see Section 3.1) divides the interpretation of ep scattering into deep inelastic scattering (DIS) for $Q^2 \gtrsim 1$ GeV and photoproduction for $Q^2 \lesssim 1$ GeV. Following theory and the relationship between Q^2 and ϑ_l (see Figure 2-1 or (2-31)), the events observed at ZEUS are generally assigned to one of two classes: DIS events, with a scattered electron observed in the central detector, and photoproduction events, where the slightly

scattered electron escapes down the beampipe and may be accepted in the ZEUS luminosity monitor (see Figure 1-1).

The kinematics of ep interactions are summarized in Table 2-1. Great care has been taken to show clearly where approximations have been made. The key to the approximations is given in Table 2-2. If read top to bottom, each expression of Table 2-1 only makes use of definitions and expressions encountered previously. The approximations most often encountered for tagged photoproduction, with $\vartheta_l \sim 0$, are given in (2-29), (2-30) and (2-31) near the bottom of Table 2-1.

Q^2_{min} defines the minimum possible Q^2 allowed by kinematics and plays an important role in measuring photoproduction using electroproduction, as shown in Section 4.4. For $ep \rightarrow e'H$ at HERA, Q^2_{min} is the left hand boundary of the kinematic range shown in Figure 2-2. Q^2_{min} arises from energy and momentum conservation at the electron-boson-lepton vertex. The outgoing lepton has angle ϑ_l with respect to the incoming electron.

$$Q^2 = -(e-l)^2 = -m_e^2 - m_l^2 + 2e \cdot l \text{ with } e \cdot l = E_e E_l - \vec{p}_e \vec{p}_l = E_e E_l - p_e p_l \cos\vartheta_l. \quad (2\text{-}35)$$

Thus, Q^2, via $e \cdot l$, is at a minimum when $\cos\vartheta_l = 1$. Q^2 can therefore be expressed as Q^2_{min} plus the remaining terms (see (2-13) and (2-14)). Using the relationship between energy, mass and momentum,

$$Q^2_{min} = -m_e^2 - m_l^2 + 2E_e E_l\left(1 - \sqrt{1 - m_e^2/E_e^2}\sqrt{1 - m_l^2/E_l^2}\right) \quad (2\text{-}36)$$

and with the approximations $m_e^2 \ll E_e^2$ and $m_l^2 \ll E_l^2$,

$$Q^2_{min} \simeq -m_e^2 - m_l^2 + 2E_e E_l(1 - 1 + m_e^2/2E_e^2 + m_l^2/2E_l^2). \quad (2\text{-}37)$$

Since $\vartheta_l = 0$, (2-29) provides $Q^2_{min} \simeq m_l^2 \frac{y}{1-y} - m_e^2 y$.

2.3 Electroweak Interactions

In the electroweak theory of the SM, the exchanged gauge boson in an ep interaction may be the photon (γ), the neutral weak vector boson (Z^0) or the charged weak vector boson ($W^\pm$). The γ, Z^0, γ/Z^0 exchanges are referred to as the neutral current interactions, while the $W^\pm$ exchanges are the charged current interactions. The weak vector bosons have the same coupling strength as the photon, ignoring the multiplier $4\sqrt{2}\sin^2\theta_w \sim 1$ due to numerical factors and the mixing angle θ_w. The cross section for a process involving the exchange of a boson of mass m contains a factor G^2 with $G(m) \propto 1/(q^2 - m^2)$. Therefore, although the electromagnetic ep interaction, via the massless photon, is not the only ep interaction, for tagged photoproduction at ZEUS, with $-q^2 \ll 1$ GeV^2 (see Figure 2-1), the relative cross sections allow the interactions via the neutral weak vector bosons, with $m_{Z^0} = 91$ GeV, to be safely ignored.

Trigonometric identities	$1-\cos\vartheta = 2\sin^2\frac{\vartheta}{2},\ 1+\cos\vartheta = 2\cos^2\frac{\vartheta}{2}.$ (2-2)
Energy and mass of the incoming proton	$E_p, m_p.$ (2-3)
4-momentum of the incoming proton	$P \equiv (E_p, 0, 0, \sqrt{E_p^2 - m_p^2}) \equiv (E_p, 0, 0, E_p).$ (2-4)
Energy, mass, scalar momentum of the incoming electron	$E_e, m_e, p_e.$ (2-5)
4-momentum of the incoming electron	$e \equiv (E_e, 0, 0, -\sqrt{E_e^2 - m_e^2}) \equiv (E_e, 0, 0, -E_e).$ (2-6)
Energy, angle, orientation of the scattered lepton	$E_l, \pi - \vartheta_l, \varphi_l.$ (2-7)
Scalar momentum of the scattered lepton	$p_l \equiv \sqrt{E_l^2 - m_l^2} \approx E_l.$ (2-8)
4-momentum of the scattered lepton	$l = (E_l, p_l\sin\vartheta_l\cos\varphi_l, p_l\sin\vartheta_l\sin\varphi_l, -p_l\cos\vartheta_l).$ (2-9)
Center of mass energy squared or total invariant mass squared	$s \equiv (e+P)^2 = m_e^2 + m_p^2 + 2e\cdot P \cong 4E_eE_p.$ (2-10)
Reduced center of mass energy squared	$\tilde{s} \equiv 2e\cdot P = s - m_e^2 - m_p^2 \cong s.$ (2-11)
4-momentum, energy of the exchanged vector boson for the neutral or charged current	$q \equiv e - l,\ E_q \equiv E_e - E_l.$ (2-12)
Momentum transfer variable	$Q^2 \equiv -q^2 = Q^2_{min} + 2p_ep_l(1-\cos\vartheta_l)$ with (2-13)
	$Q^2_{min} = -m_e^2 - m_l^2 + 2(E_eE_l - p_ep_l).$ (2-14)
	$Q^2 \approx Q^2_{min} + 4E_eE_l\sin^2\frac{\vartheta_l}{2}.$ (2-15)
	$Q^2 \sim 4E_eE_l\sin^2\frac{\vartheta_l}{2}$ when $Q^2 \gg Q^2_{min}.$ (2-16)
Energy of the current in the proton rest frame	$\nu \equiv \frac{P\cdot q}{m_p} \approx \frac{2E_p}{m_p}(E_e - E_l\cos^2\frac{\vartheta_l}{2}).$ (2-17)
Maximum possible energy of the current	$\nu_{max} \equiv \frac{\tilde{s}}{2m_p}.$ (2-18)
Bjorken-y scaling variable, $0 \le y \le 1$	$y \equiv \frac{P\cdot q}{P\cdot e} = \frac{2P\cdot q}{\tilde{s}} = \frac{\nu}{\nu_{max}} \approx 1 - \frac{E_l}{E_e}\cos^2\frac{\vartheta_l}{2}.$ (2-19)

Table 2-1 Symbols and kinematic variables for ep interactions at HERA.

Bjorken-x scaling variable, $0 \le x \le 1$	$x \equiv \frac{Q^2}{2P\cdot q} = \frac{Q^2}{2m_p\nu}.$ (2-20)
	$x \sim \frac{E_eE_l\sin^2\frac{\vartheta_l}{2}}{E_p(E_e - E_l\cos^2\frac{\vartheta_l}{2})}$ when $Q^2 \gg Q^2_{min}.$ (2-21)
Squared invariant mass of the hadronic system, $m_p^2 \le W^2 < \tilde{s}$	$W^2 \equiv (q+P)^2 = 2\nu m_p - Q^2 + m_p^2 = \tilde{s}y - Q^2 + m_p^2 = Q^2\frac{1-x}{x} + m_p^2$ (2-22)
Additional relations	$Q^2 = xy\tilde{s}.$ (2-23)
	$Q^2_{min} \approx m_l^2(\frac{y}{1-y}) - m_e^2y.$ (2-24)
	If the outgoing lepton is an electron $Q^2_{min} \approx m_e^2\frac{y^2}{1-y}$, (2-25)
	with $Q^2_{min} \sim m_e^2\frac{(W^2-m_p^2)^2}{s^2}$ when $y \ll 1.$ (2-26)
	$y \approx 1 - \frac{Q^2 - Q^2_{min}}{4E_e^2\tan^2\frac{\vartheta_l}{2}}.$ (2-27)
	$Q^2 - Q_{min} \sim 4E_e^2\tan^2\frac{\vartheta_l}{2}$ when $y \ll 1.$ (2-28)
For tagged photoproduction where $\vartheta_l \sim 0$	$y \sim 1 - E_l/E_e \sim E_q/E_e.$ (2-29)
	$W \sim 2\sqrt{E_qE_p} \sim 2\sqrt{yE_eE_p}$ when $W \gg m_p.$ (2-30)
	$Q^2 - Q^2_{min} \sim (1-y)E_e^2\vartheta_l^2 \sim E_eE_l\vartheta_l^2 \sim 4xE_qE_p.$ (2-31)
Convenient relations for evaluating ep matrix elements	$P^2 \equiv m_p^2,\ e^2 \equiv m_e^2,\ l^2 \equiv m_l^2.$ (2-32)
	$e\cdot P \equiv \tilde{s}/2,\ P\cdot l \equiv e\cdot P(1-y),\ P\cdot q \equiv -q^2/2x.$ (2-33)
	When the outgoing lepton is an electron, $q^2/2 = m^2 - l\cdot e = -q\cdot l = e\cdot q.$ (2-34)

Table 2-1 Symbols and kinematic variables for ep interactions at HERA.

$\equiv$	denotes definitions of variables.
$=$	denotes the results of evaluations.
$\cong$	denotes the excellent approximations at HERA using $m_p^2 \ll s$ and/or $m_e \ll E_e$.
$\approx$	denotes the approximations, perhaps in addition those above, using $m_l \ll E_l$, which only fails for scattered electrons with $y \approx 1$ or for exotica such as excited electrons.
$\sim$	denotes approximations, perhaps in addition those above, with additional requirements.

HERA collides electrons head-on with protons.
Following the ZEUS coordinate system, the protons travel in the direction of the positive z-axis.
In the ZEUS coordinate system (see Section 6.1) the polar angle of the electron θ_l is related to the electron scattering angle ϑ_l by $\theta_l = \pi - \vartheta_l$.

Table 2-2 Key to Table 2-1.

2.4 The Electromagnetic Electron-Proton Cross Section

Any cross section can be expressed as

$$d\sigma = \frac{1}{F}\overline{|M|^2}\,dLips. \tag{2-38}$$

F is the flux of particles available for the interaction, and in a collinear collision between particles A and B,

$$F = 4\left(|\vec{p}_A|E_B + |\vec{p}_B|E_A\right) = 4\left((p_A \cdot p_B)^2 - m_A^2 m_b^2\right)^{1/2}. \tag{2-39}$$

The Lorentz invariant phase space factor ($dLips$) describes the number of available final states for the interaction. The ep interactions will be described in terms of the scattered lepton, and for a single particle in the final state

$$dLips = \frac{d^3l}{(2\pi)^3 2E_l}. \tag{2-40}$$

The invariant amplitude M describes the physics of the interaction. In order to calculate the unpolarized cross section, $\overline{|M|^2}$ denotes the square of the invariant amplitude, averaged over the spins of the incoming particles and summed over the spins of the particles in the final state. To lowest order, ep interactions occur via the exchange of a single photon, for which $\overline{|M|^2}$ can be expressed in terms of the leptonic tensor $L_{\mu\nu}$ and the hadronic tensor $W_{\mu\nu}$ describing the electron and proton vertices with the exchanged photon, respectively:

$$\overline{|M|^2} = \frac{16\pi^2\alpha^2}{q^4} L^{\mu\nu} 4\pi m_p W_{\mu\nu}. \tag{2-41}$$

The fraction $16\pi^2\alpha^2/q^4$ is due to the photon propagator. The term $4\pi m_p$ arises from the standard normalization of $W_{\mu\nu}$. The leptonic tensor for the point-like electron is given by

$$L_{\mu\nu} = 2\left[l_\mu e_\nu + l_\nu e_\mu + \frac{q^2}{2} g_{\mu\nu}\right]. \tag{2-42}$$

The hadronic tensor parametrizes the interaction of the photon. Beginning with the most general form possible for $W_{\mu\nu}$, it is simplified by various constraints. Conservation of the proton current requires $q_\mu W^{\mu\nu} = q_\nu W^{\mu\nu} = 0$. For the unpolarized cross section, $L_{\mu\nu}$ is symmetric, and hence only symmetric terms in $W_{\mu\nu}$ can contribute to $\overline{|M|^2}$. The electromagnetic interaction is parity conserving and time-reversal invariant and since $\overline{|M|^2}$ must be a real quantity, $W_{\mu\nu}$ can be reduced to an expression involving two independent functions W_1 and W_2:

$$W_{\mu\nu} = \frac{W_2}{m_p^2}\left[P_\mu - \frac{P\cdot q}{q^2} q_\mu\right]\left[P_\nu - \frac{P\cdot q}{q^2} q_\nu\right] + W_1\left[-g_{\mu\nu} + \frac{q_\mu q_\nu}{q^2}\right]. \tag{2-43}$$

The functions are given in terms of any two variables describing the event kinematics, for example $W_1 = W_1(y, Q^2)$ and $W_2 = W_2(y, Q^2)$.

Evaluating $L^{\mu\nu}W_{\mu\nu}$, making use of (2-34), the term multiplying $2W_1$ is

$$\left[l^\mu e^\nu + l^\nu e^\mu + \frac{q^2}{2} g^{\mu\nu}\right]\left[-g_{\mu\nu} + \frac{q_\mu q_\nu}{q^2}\right] = -2l\cdot e - 2q^2 + \frac{2}{q^2} q\cdot l\, q\cdot e + \frac{q^2}{2}$$
$$= Q^2\left(1 - \frac{2m_e^2}{Q^2}\right). \tag{2-44}$$

Similarly, making use of (2-23), (2-32), (2-33) and (2-34), the term multiplying $2W_2/m_p^2$ is

$$\left[l^\mu e^\nu + l^\nu e^\mu + \frac{q^2}{2} g^{\mu\nu}\right]\left[P_\mu P_\nu + \frac{1}{2x}(P_\mu q_\nu + P_\nu q_\mu) + \frac{1}{4x^2} q_\mu q_\nu\right]$$

$$= 2P\cdot l P\cdot e + \frac{m_p^2 q^2}{2} + \frac{1}{2x}(2P\cdot l\, q\cdot e + 2P\cdot e\, q\cdot l + P\cdot q\, q^2)$$
$$+ \frac{1}{4x^2}\left(2l\cdot q e\cdot q + \frac{q^4}{2}\right), \tag{2-45}$$

for which the two expressions in parentheses can be shown to be 0, leaving

$$\frac{\bar{s}^2}{2}\left(1 - y + \frac{m_p^2 xy}{\bar{s}}\right), \tag{2-46}$$

where $\bar{s}$ is the square of the reduced center of mass energy (see (2-11)).

For ep collisions at HERA, $F = 2\tilde{s}$ is an excellent approximation and $dLips$ can be written in terms of the variables introduced in Table 2-1. Rewriting $\overline{|M|^2}$ using the results of (2-44) and (2-46) allows the ep cross section to be expressed as

$$d^2\sigma_{ep} = \frac{1}{2\tilde{s}} \frac{16\pi^2\alpha^2}{Q^4} 4\pi m_p \left[2W_1 Q^2 \left(1 - \frac{2m_e}{Q^2}\right) + \frac{W_2 \tilde{s}^2}{m_p^2} \left(1 - y + \frac{m_p^2 xy}{\tilde{s}}\right) \right] \frac{1}{4(2\pi)^2} dQ^2 dy \,. \quad (2\text{-}47)$$

Introducing the proton structure functions defined as

$$F_1(y, Q^2) \equiv m_p W_1(y, Q^2) \qquad F_2(y, Q^2) \equiv \nu W_2(y, Q^2) \equiv \frac{\tilde{s}y}{2m_p} W_2(y, Q^2), \quad (2\text{-}48)$$

provides

$$\frac{d^2\sigma_{ep}(y, Q^2)}{dydQ^2} = \frac{4\pi\alpha^2}{Q^4} \left[y\left(1 - \frac{2m_e^2}{Q^2}\right) x F_1(y, Q^2) + \frac{1}{y}\left(1 - y - \frac{xym_p^2}{\tilde{s}}\right) F_2(y, Q^2) \right]. \quad (2\text{-}49)$$

The above equation is the usual expression for the parity conserving neutral current double differential ep cross section, with the exception that the mass terms have explicitly been kept.

2.5 Expressing Electroproduction in Terms of Photoproduction

The term Equivalent Photon Expression (EPE) is introduced here to name the technique of reducing the collision of fast charged particles to the collision of one of the particles with a photon from the other. Electron-proton scattering, as shown in Figure 2-1, is reduced to photoproduction as shown in Figure 2-3.

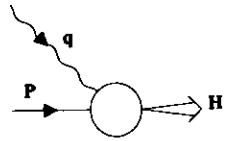

Figure 2-3 Basic diagram for photoproduction.

A short description of the photon is required at this point. Photons have spin $J = 1$, so quantum mechanics allows for $2J + 1 = 3$ possible substates, $J_z = -1, 0, +1$. J_z determines the **polarization** vector, the direction of the electromagnetic field associated with the photon. The photon travels in direction $\hat{q}$. For $J_z = -1, +1$ the field is **transverse** to $\hat{q}$, for $J_z = 0$ it is **longitudinal** to $\hat{q}$. The **helicity**, λ, is the spin component of the particle in its direction of motion. For the photon, $\lambda = J \cdot \hat{q}$, and J is defined such that $\lambda = J_z$. Lorentz invariance allows only two substates

for massless particles of spin J: $J_z = -J, +J$. Therefore, real photons are only transversely polarized. Virtual photons (γ^*), being massive, can be longitudinally or transversely polarized. The helicity of a particle is not parity conserving. Under space inversion, the helicity changes sign. Since the electromagnetic interaction is parity conserving, the $J_z = -1$ and the $J_z = +1$ photons must always occur with equal amplitude. Therefore the transverse polarization of the photon refers to the sum of the two transverse terms.

The ep cross section can be expressed in terms of the photon-proton cross section as

$$d\sigma_{ep}(y, Q^2) = \sigma_T(y, Q^2)\, dn_T + \sigma_L(y, Q^2)\, dn_L. \quad (2\text{-}50)$$

The photoproduction cross section is divided into σ_T and σ_L for transverse and longitudinal photons respectively. The quantity dn, defined for both longitudinal and transverse photons, is called the equivalent photon number or spectrum and is defined by the $e \to lq$ vertex in Figure 2-1. Equation (2-50) is an exact expression of the electromagnetic ep cross section and is simply an alternative to writing the cross section in terms of the proton structure functions F_1 and F_2. Instead of evaluating dn_T and dn_L directly, σ_T and σ_L are first evaluated in terms of F_1 and F_2, (2-49) is then used to express the ep cross section in terms of σ_T and σ_L.

2.6 The Photon-Proton Cross Section

The total photon-proton (γp) cross section for real photons can be extended to define a total $\gamma^* p$ cross section for virtual photons. In this section, the $\gamma^* p$ collisions are examined in the proton rest frame, which provides considerable simplification.

The total γp cross section for the collision of real photons with protons is given by

$$\sigma_\lambda(\gamma p) = \frac{4\pi^2\alpha}{K} \varepsilon_\lambda^\mu \varepsilon_\lambda^{\nu *} W_{\mu\nu}, \quad (2\text{-}51)$$

where the photon has energy or momentum K and polarization ε_λ. The total cross section for virtual photons is also given by (2-51), but with additional considerations for the photon flux factor and for the polarization.

Real photons have a flux factor $4m_p K$ in (2-51). For virtual photons, the flux and thus the cross section, is not a well defined concept. In one approach, due to Gilman [22], the virtual photon is treated as any other particle. The flux is then proportional to $K = |\vec{q}| = (\nu^2 + Q^2)^{1/2}$, the momentum of the virtual photon. In a second (and the conventional) approach, due to Hand [23], K is required to be the energy of a real photon needed to create the equivalent hadronic system. Therefore, using (2-22) with $Q^2 = 0$ for the real photon, $W^2 = m_p^2 + 2Km_p$ or $K = (W^2 - m_p^2)/(2m_p)$. Both approaches reduce to $K = \nu$ in the limit $Q^2 \to 0$ as required for

real photons. The similarity between the two approaches to the flux is best appreciated by rewriting them as

$$K_{GILMAN} = \nu\left(1+\frac{Q^2}{\nu^2}\right)^{1/2} = \nu\left(1+\frac{m_p^2}{yE_eE_p}x\right)^{1/2}, \tag{2-52}$$

which has made use of (2-18) through (2-20) and (2-10). Using (2-22) provides

$$K_{HAND} = \frac{-Q^2+2m_p\nu}{2m_p} = \nu(1-x). \tag{2-53}$$

Real photons can only be transversely polarized, while virtual photons can also have longitudinal polarization. Taking the z-axis along $\hat{q}$ of the photon, the polarization vectors ε_λ^μ for the virtual photons (helicity λ) are

$$\lambda = 1 : \quad \varepsilon_\pm = \mp\frac{1}{\sqrt{2}}(0;1,\pm i,0), \tag{2-54}$$

$$\lambda = 0 : \quad \varepsilon_0 = \frac{1}{\sqrt{Q^2}}(\sqrt{\nu^2+Q^2};0,0,\nu). \tag{2-55}$$

Therefore, taking the polarization and flux into consideration, (2-51) can be evaluated, using (2-43), for the total γp transverse and longitudinal cross sections:

$$\sigma_T = \frac{\sigma_+ + \sigma_-}{2} = \frac{4\pi^2\alpha}{K}W_1, \tag{2-56}$$

$$\sigma_L = \sigma_0 = \frac{4\pi^2\alpha}{K}\left[\left(1+\frac{\nu^2}{Q^2}\right)W_2 - W_1\right]. \tag{2-57}$$

As already seen in (2-52), $\nu^2/Q^2 = (E_eE_p/m_p^2)\,y/x$. At HERA, $\nu^2/Q^2 = 2.5\times10^4 y/x \gg 1$ for the entire kinematic range (see Figure 2-1), excluding a very small and safely ignored region of quasi-elastic scattering with $y/x < 10^{-4}$ at $W \sim m_p + m_{\pi 0_l}$ and $m_{\pi 0} \le Q^2 \le 4m_p$ (see (2-22)). Rewriting the cross section in terms of the structure functions defined in (2-48) results in

$$\sigma_T = \frac{4\pi^2\alpha}{m_pK}F_1, \tag{2-58}$$

$$\sigma_L = \frac{4\pi^2\alpha}{m_pK}\left[m_p\frac{\nu^2}{Q^2}\frac{F_2}{\nu} - F_1\right] = \frac{4\pi^2\alpha}{m_pK}\left[\frac{F_2}{2x} - F_1\right] = \frac{4\pi^2\alpha}{m_pK}\frac{F_L}{2x}, \tag{2-59}$$

where σ_L has motivated and used the longitudinal structure function defined as

$$F_L \equiv F_2 - 2xF_1. \tag{2-60}$$

2.7 The Equivalent Photon Expression

The ep cross section as given by (2-49) can rewritten as

$$\frac{d^2\sigma_{ep}(y,Q^2)}{dydQ^2} = \frac{4\pi\alpha^2}{Q^4}\left[\left(\frac{1+(1-y)^2}{y} - 2\frac{(1-y)}{y}\frac{Q^2_{min}}{Q^2}\right)xF_1(y,Q^2) + \frac{1}{y}(1-y)F_L(y,Q^2)\right] \tag{2-61}$$

by using F_L defined in (2-60), Q^2_{min} of (2-25), and ignoring the $m_p^2/\tilde{s}$ term in (2-49).

For the γ^*p scattering at small Bjorken-x, $K = \nu$ for the flux, in either the Gilman or Hand convention (see (2-52) and (2-53)). Solving (2-58) and (2-59) for F_1 and F_L yields

$$xF_1 = \frac{1}{4\pi^2\alpha}\frac{Q^2}{2}\sigma_T, \qquad F_L = \frac{1}{4\pi^2\alpha}\frac{Q^2}{2}2\sigma_L. \tag{2-62}$$

The restriction to small Bjorken-x for (2-62) provides simplification, but one could also proceed without this restriction.

Finally, following (2-50), the electromagnetic ep cross section is expressed in terms of the γ^*p cross section

$$\frac{d^2\sigma_{ep}(y,Q^2)}{dydQ^2} = \frac{\alpha}{2\pi}\frac{1}{Q^2}\left[\left(\frac{1+(1-y)^2}{y} - 2\frac{(1-y)}{y}\frac{Q^2_{min}}{Q^2}\right)\sigma_T(y,Q^2) + 2\frac{(1-y)}{y}\sigma_L(y,Q^2)\right]. \tag{2-63}$$

The above equation is the EPE for inelastic ep scattering at small Bjorken-x.

3 Photon-Proton Interactions

The total photoproduction cross section implicitly refers to the hadronic interactions of the photon and the proton. In addition to the gauge bosons, the particles observed in nature are either hadrons or leptons. Leptons are considered to be elementary particles, since there are no experimental indications of internal structure. Hadrons have an internal structure made out of quarks and gluons. Quarks are considered to be elementary particles. Gluons are the gauge bosons of the strong force. Unlike the leptons and the other gauge bosons, the quarks and gluons, carrying the color charge of the strong force, do not exist freely in nature. The strong force is constant at large distances, so free quarks and gluons would require arbitrarily large amounts of potential energy. Instead they are confined as the parton constituents of uncolored hadrons. With any combination of flavors, quark-antiquark ($q\bar{q}$) pairs form mesons, while triplets of quarks form baryons, such as the proton (uud) or neutron (udd). Due to the strong force, the two or three valence quarks of the hadron are in a sea of virtual partons. The theory of the strong force is quantum chromodynamics (QCD).

All possible hadronic $\gamma^* p$ interactions must be considered in a measurement of the total photoproduction cross section. High energy $\gamma^* p$ interactions may be described by three basic event categories. The majority of interactions are due to the interaction of the proton with the hadronic structure of the photon, which is well described by the Vector Meson Dominance (VMD) model [24]. Additional events are due to the direct coupling of the photon with a parton of the proton. The third category of interactions arises from the resolution of the photon at high energies into a quark-antiquark pair, one of which interacts with the partons of the proton. The latter behavior is the so-called anomalous photon contribution. With the ansatz that an incoherent sum of the three parts can be used [25], the total photoproduction cross section is given by

$$\sigma_{\text{tot}}^{\gamma^* p}(W, Q^2) = \sigma_{\text{VMD}}^{\gamma^* p}(W, Q^2) + \sigma_{\text{direct}}^{\gamma^* p}(W, Q^2) + \sigma_{\text{anomalous}}^{\gamma^* p}(W, Q^2) \qquad (3\text{-}1)$$

for a photon of virtuality Q^2 in a collision with a proton at a center of mass energy W. A complete description of photoproduction, based on the above ansatz, is proposed in [26].

The incoherent sum can be used since the phase space of the individual processes in (3-1), including the 4 classes of VMD hadron-proton scattering introduced below, have little overlap. The exception of (semi-) hard VMD scattering (see Section 3.2.4) and the anomalous photon interactions is dealt with by using a photon structure function which combines the two contributions (see Section 3.3).

Though the electromagnetic interactions, such as electron pair production $\gamma^* p \to e^+ e^- p$, have larger cross sections [27] than the above hadronic interactions, they are a background that can

be safely ignored. The outgoing particles rarely have enough transverse momentum to exit the beampipe and be observed in the ZEUS detector [28].

3.1 Comparison with DIS

In deep inelastic scattering (DIS), where the momentum transfer carried by the photon between the electron and proton is high, $Q^2 \gtrsim 1\ \text{GeV}^2$, the photon is considered to couple directly to the parton content, the quarks and gluons, of the proton. In DIS, the photon is treated as a point particle. The high Q^2 allows the quark parton model and perturbative QCD to describe the interaction in terms of the structure of the proton. At low Q^2, another technique is required.

For real photons, $Q^2 = 0$, or photons of low virtuality, $Q^2 \lesssim 1\ \text{GeV}^2$, high energy interactions with the proton are well described by treating the photon as a particle which may have hadronic structure. A photon need not be a point particle.

While the distinction between low and high Q^2 photons has been successful, it is not fundamental, and is under increasing study. Of special interest is the transition region, Q^2 of order $1\ \text{GeV}^2$, where results are expected from HERA using the ZEUS beamline calorimeter (see Section 6.1).

3.2 Vector Meson Dominance

Photon-proton interactions have experimental signatures remarkably similar to hadron-proton interactions. See [4] for references to measurements and an introduction to VMD:

> "At a very crude level this can be understood if the physical photon were a superposition of two types of states: a bare photon $|\gamma_B\rangle$, which at high energies accounts for a small, or perhaps negligible, portion of the interaction; and a small - of order $\sqrt{\alpha}$ - hadronic component $\sqrt{\alpha}\,|h\rangle$ which undergoes conventional hadronic interactions. That is, we expect the important part of the physical photon state to be expressible as
>
> $$|\gamma\rangle = \sqrt{Z_3}\,|\gamma_B\rangle + \sqrt{\alpha}\,|h\rangle\ , \qquad (3\text{-}2)$$
>
> where Z_3 is introduced to assure the proper normalization of $|\gamma\rangle$; all states in (3-2) have the same 3-momentum **k**. Invariance conditions dictate that $|h\rangle$ should have the same symmetry quantum numbers as the photon, i.e., $J^{PC} = 1^{--}$, $Q = B = S = 0$. The copious production of the vector mesons ρ^0, ω, and ϕ suggests that they provide very important contributions to $|h\rangle$. The restrictive assertion that these three mesons are the sole hadronic constituents of the photon, and that the bare component $|\gamma_B\rangle$ cannot interact with hadrons, is the hypothesis of vector-meson dominance (VMD) in its most naive and clear-cut form."

The bare photon components are the anomalous and direct contributions discussed in Sections 3.3 and 3.4, respectively.

For $\gamma^* p$ collisions, VMD [24] predicts

$$\sigma_T^{\gamma^* p}(W, Q^2) = \sum_{V=\rho^0, \omega, \phi} \frac{e^2}{f_V^2}\left(\frac{m_V^2}{m_V^2+Q^2}\right)^2 \sigma_T^{Vp}(W)$$

$$\sigma_L^{\gamma^* p}(W, Q^2) = \sum_{V=\rho^0, \omega, \phi} \frac{e^2}{f_V^2}\left(\frac{m_V^2}{m_V^2+Q^2}\right)^2 \sigma_T^{Vp}(W)\frac{\xi_V Q^2}{m_V^2} \qquad (3\text{-}3)$$

for the transverse and longitudinal components of the cross section at a center of mass energy W and photon virtuality Q^2. The total cross sections $\sigma_T^{Vp}(W)$ of the transversely polarized vector mesons $V = \rho, \omega, \phi$ are required. The photon-vector meson coupling constants, f_V, are assumed and have so far been measured to be independent of the photon energy and Q^2 [4]. The coupling constants are in fact determined from e^+e^- annihilation, where $Q^2 = -m_V^2$. Further tests of the assumption that the f_V are constant will be made at HERA with W and Q^2 larger than previous measurements.

The factor ξ_V, defined by $\xi_V(W) = \sigma_L^{Vp}(W)/\sigma_T^{Vp}(W)$ with the expectation $0 \le \xi_V \le 1$, is introduced because longitudinally and transversely polarized hadrons may not have the same cross section. VMD requires ξ_V be constant or to vary only slowly with W. The value and behavior of ξ_V remains uncertain. For example, a recent measurement claims that the data requires $\xi_V \approx 0$ [29]. A re-examination of the data disputes this finding and makes arguments for $\xi_V \approx 1$, as observed in other experiments and as expected by arguments based on the additive quark model or based on models of the Pomeron [30]. Because the determination of ξ_V requires a finite Q^2, the maximum Q^2 at which VMD is expected to be applicable must also be considered, though this limit is not well understood. HERA will measure ξ_V for at least some range of Q^2 and perhaps W, as determined by the scattered electron observed in LUMIE or in CAL.

The $\gamma^* p$ interactions due to the hadronic photon are thus described by Vp interactions. The four classes of interaction are shown in Figure 3-1 and are discussed in the following subsections.

3.2.1 Elastic Diffraction

In photoproduction, elastic scattering refers to the VMD reaction

$$\gamma^* p \to Vp, \qquad (3\text{-}4)$$

as shown in Figure 3-1 a). Truly elastic Compton scattering $\gamma^* p \to \gamma p$, for tagged photoproduction where the outgoing γ may be seen in the central ZEUS detector, occurs at a negligible rate.

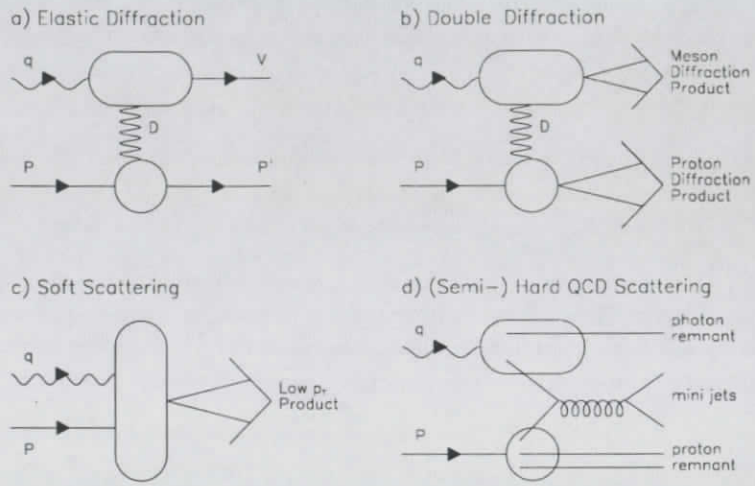

Figure 3-1 Photon-proton interactions according to VMD.
The incoming photon q is assumed to transform into a vector meson before interacting with the incoming proton P.
An example is given from each of the four classes of hadron-hadron interactions.
a) Elastic Diffraction: *The vector meson V and proton P′ are intact following the scattering.*
b) Double Diffraction: *Both the vector meson and the proton are scattered into more massive states.*
c) Soft Scattering: *The vector meson and the proton combine in a soft hadronic interaction resulting in a final state with little transverse momentum.*
d) (Semi-) Hard QCD Scattering: *A parton in the vector meson has a hard scattering with a parton in the proton, producing so-called mini-jets.*

The theory of diffractive interactions draws analogies and its name from the diffraction of light by a circular aperture. An introduction to the experimental results and their description by the theory is given in [31].

Elastic scattering is the simplest type of diffractive scattering and fits the analogy with classical diffraction best. The intensity of scattered light with wave number k, beyond a circular aperture, radius R, as a function of angle ϑ is given by

$$\frac{I}{I_o} = 1 - \frac{R^2}{4}(k\vartheta)^2. \qquad (3\text{-}5)$$

For elastic scattering

$$\frac{d\sigma/dt}{(d\sigma/dt)_{t=0}} = e^{bt} \approx 1 - b\,(p\vartheta)^2, \tag{3-6}$$

where p is the momentum of the diffracting particle, in a frame where the target particle is at rest. The square of the four momentum transfer between the scattered hadrons is $t \equiv D^2 < 0$. The boson D of diffractive scattering, shown in Figure 3-1 a) and b), need not be interpreted as a physical particle, though such an interpretation is often convenient. The boson denotes an exchange of energy and momentum between the hadrons of the scattering without the exchange of any quantum numbers. Applying the optics analogy and solving for the slope parameter yields

$$b = R^2/4. \tag{3-7}$$

The radius of strong interactions can be estimated as the mass of the pion yielding $b = 12.5\ \mathrm{GeV}^{-2}$, which is within the range of measured slope parameters. Therefore, as in the diffraction of light, the slope of the elastic peak is related to the size of the scattering object. The measured slope has a slow dependence on the center of mass energy of the scattering. Preliminary results, consistent with the above description and measurements at lower energies, for $\gamma^* p \to \rho p$ with $20 < W < 80\ \mathrm{GeV}^2$ have been given by the other experiment at HERA, H1 [32].

3.2.2 Diffractive Scattering

Inelastic diffractive scattering has three types:

$$\text{proton diffraction: } \gamma^* p \to V X_p \tag{3-8}$$

$$\text{photon diffraction: } \gamma^* p \to X_V p \tag{3-9}$$

$$\text{double diffraction: } \gamma^* p \to X_V X_p \tag{3-10}$$

determined by which of the incoming particles diffracts into a higher mass state X, $M_{X_{p,V}} > m_{p,V}$. Double diffraction is shown in Figure 3-1 c). Momentum transfer arguments predict the cross section to have an approximate $1/M_X^2$ dependence such that

$$\frac{d^2\sigma}{dt\,dM_X^2} \propto \frac{e^{bt}}{(M_X^2)^a}, \tag{3-11}$$

where $a \sim 1$. This has been observed in many hadron-hadron experiments [31] and in $\gamma p \to Xp$ [33]. In the resonance region, $M_{X_p} \lesssim 5$ GeV for the proton [31] and $M_{X_V} \lesssim 2$ GeV for the VMD photon [33], the slope parameter b is observed to fall to roughly half the elastic value and then remain constant for higher M_X.

3.2.3 Soft Scattering

Non-diffractive hadron-hadron interactions are divided into a soft part and a hard part. The soft part consists of events with little transverse momentum (p_T) which are due to neither diffraction nor hard scattering.

The internal energy scale of the soft scattering is too low to allow the dynamics of the event to be described by perturbative QCD. Unlike the diffractive events, no analogies to other physical processes are known to help guide the description of the soft events. Hence no mechanism for the soft scattering is shown in Figure 3-1 c). The soft part can only be modelled, usually making heavy use of parametrizations based on previous experimental measurements.

3.2.4 (Semi-) Hard Scattering

All hadrons, including the VMD photon, are made out of quarks and gluons. In a high energy $\gamma^* p$ collision, this structure of the hadrons can be resolved and the point-like parton constituents can interact directly in a hard scattering, as shown in Figure 3-1 d). The scattered partons balance each other with transverse momentum p_T. The partons are highly virtual, thus each produces a so-called parton shower consisting of partons of lower virtuality. Partons carry the QCD color charge and are thus not observed as free particles. Partons are confined within hadrons which carry no net color charge. Therefore, at the end of the shower, the partons are "dressed" as hadrons in a process called hadronization. The outgoing partons from the original hard scattering are thus observed as jets of particles. Although the fundamental properties of the hadron are determined by its two or three valence quarks, the internal structure is dominated by a sea of virtual gluons and quark-antiquark pairs, each carrying only a very small fraction of the momentum of the hadron. Thus in hard $\gamma^* p$ scatterings, the majority of parton-parton collisions involve only a small fraction of the total center of mass energy, hence the name mini-jets.

The photon and proton remnants are each QCD color charged following the hard scattering. Therefore the fragmentation of partons into jets described above, is actually carried out for the global event. In the process, the remnants gain some transverse energy and hence may be observed away from the original beam direction.

Evidence that a sizable fraction of the hadron-hadron total cross section may be due to mini-jets was first presented by UA1 observations of proton-antiproton collisions [34]. The mini-jets are claimed to be observed with transverse momentum as low as 5 GeV.

Due to three uncertainties, the mini-jet model gave a wide range of predictions for the value of the total photoproduction cross section at high energies [13]. The first unknown is the density of partons in the proton and the photon. These are respectively given by the proton structure functions (F_2^p), called F_2 in the previous chapter, and the photon structure function (F_2^γ). The second

uncertainty is the transverse momentum cutoff $p_T^{\min}$ in the parton-parton hard scattering cross section,

$$\sigma_{\text{hard}}(p_T^{\min}) \sim \int_{(p_T^{\min})^2}^{W/4} \frac{H(F_2^p, F_2^\gamma)}{p_T^4} dp_T^2, \tag{3-12}$$

where $H(F_2^p, F_2^\gamma)$ depends on the structure functions. The third uncertainty is the possibility of multiple parton-parton scatterings above $p_T^{\min}$ within a single $\gamma^* p$ collision.

Due to the steep p_T dependence of (3-12), $p_T^{\min}$ provides for the largest uncertainty in the cross section. Although $p_T^{\min}$ is not a calculable quantity, it is reasonable to argue that the partons must have a wavelength $\lambda \sim 1/p_T$ short enough to see the each other, and not just the uncolored hadron [35]. Therefore, the cutoff can be estimated by the size R of the interacting hadrons, $p_T^{\min} \sim 1/R \sim 1-2$ GeV.

3.2.5 The Additive Quark Model

Vector mesons, being short lived particles, are not available as a beam or target for high energy collisions. VMD would be of very limited use for describing $\gamma^* p$ collisions, if Vp collisions could not be determined by means other than a direct measurement. Fortunately, the additive quark model [36] states that the behavior of hadron-hadron collisions are determined by their valence quark constituents. The Vp collisions, for $V = \rho, \omega, \phi$, can thus be determined from πp and Kp data.

3.3 Anomalous

The anomalous photon part of the cross section is very similar to the VMD (semi-) hard scattering described above; compare Figure 3-1 d) and Figure 3-2. They differ only by the parton

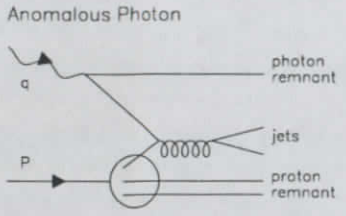

Figure 3-2 The anomalous photon interaction with the proton.
The photon can split into a quark-antiquark pair, allowing a parton from each of the photon and proton to interact in a hard scattering producing jets.

distributions for the photon. For the VMD photon, the distribution is that of the vector mesons. For the anomalous photon the structure of partons originates from the photon to quark-antiquark pair splitting. The latter is calculable in perturbative QCD, and deserves the name anomalous since the result differs greatly from that expected by the quark parton model [37]. This can be contrasted to the case of the proton, where the quark parton model provides the correct parton distribution to within logarithmic factors.

The cross section for the anomalous photon part of hard scattering is also given by (3-12). Therefore, the photon structure function may be thought of as being divided in two parts:

$$F_2^\gamma = F_2^{\text{VDM}} + F_2^{\text{anomalous}}. \tag{3-13}$$

Due to its origin as a quark-antiquark pair, the parton distribution of the anomalous photon is much harder than that of the vector mesons. Therefore, high p_T jets, with a photon remnant, are expected to be dominantly due to the anomalous photon, not the VMD photon.

The anomalous photon is determined by QCD and hence is governed by the QCD mass scale $\Lambda_{\text{QCD}} \sim 200$ MeV. Virtual photons with $Q^2 \ll \Lambda_{QCD}^2$ are therefore treated as real photons to good approximation. This issue, also for high Q^2 photons, is examined in [38].

3.4 Direct

The photon can also couple directly to the parton constituents of the proton as shown in Figure 3-3. With the full energy of the photon involved in the collision, direct photoproduction is the dominant process for the highest p_T jets from photoproduction. The direct events with jets are also distinguished by their lack of a photon remnant.

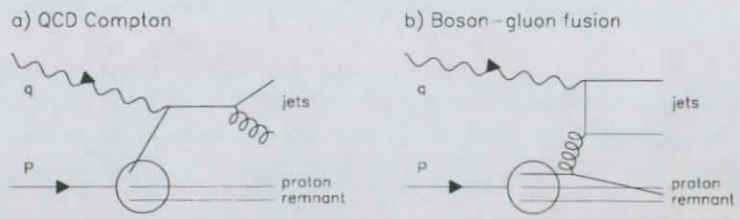

Figure 3-3 Direct photoproduction diagrams.
The photon can couple directly to the partons in the photon. Two mechanisms dominate:
a) QCD Compton: *The photon is absorbed by a quark in the proton and is emitted as a gluon.*
b) Boson Gluon Fusion: *The photon combines with a gluon from the proton, producing a quark-antiquark pair.*

The direct photon-proton cross section has been measured to be 0.25 ± 0.12 of the total photoproduction cross section [33] given two caveats. The measurement emerges from the finite-mass sum rule [31] and it assumes that the direct and VMD diffractive cross sections scale to the corresponding total cross sections. The result is consistent with the fact that VMD accounts for only ~ 80 % of the total photoproduction cross section [39]. The latter is a weak argument, since extended VMD models can account for the full total cross section by incorporating the higher mass vector mesons J/ψ and Υ, excited higher mass states of the vector mesons ρ', ρ'', ..., ω', ..., non-diagonal transitions such as $\rho p \rightarrow \rho' p$ and/or other extensions to VMD as proposed in [39] or, for example, as used in a more recent analysis by [40]. VMD photons are shadowed in nuclei, while direct photons should not be, so the ~ 20 % fraction of direct events is also consistent with the fact that only ~ 80 % of the photoproduction cross section experiences the shadowing effects [4]. Again, the case for a sizable cross section due to the direct photon is weakened by extensions to VMD which can describe the nuclear shadowing data[41]. From comparisons of γp to πp and Kp measurements, the Omega Photon Collaboration has three pieces of evidence for a direct photon component. The γp interactions are observed to have relative excesses, attributed to the direct component, of single charged particles with $p_T \geq 1.6$ GeV [42], of events with a large charged particle inclusive energy flow ($\Sigma p_T^2 > 3$ GeV^2) [43], and of ρ production for $p_T \geq 2$ GeV [44]. For $p_T \gtrsim 5$ GeV, ZEUS has observed an unambiguous signal for the direct process in the photoproduction of events with two jets [45].

The direct cross section is given by

$$\sigma_{\text{direct}}(p_o) \sim \int_{p_o^2}^{W/4} \frac{D(F_2^p)}{p_T^2} dp_T^2. \tag{3-14}$$

where p_o is not calculable. In comparison with $\sigma_{\text{hard}}(p_T^{\text{min}})$ in (3-12), $\sigma_{\text{direct}}(p_o)$ is determined by $D(F_2^p)$ which depends only on the proton structure function, and the denominator in the integrand is p_T^2, not p_T^4. The direct component is 20% of the total photoproduction cross section when $p_o = 0.5$ GeV [25] with uncertainties from the proton distribution functions and the value of the strong coupling constant. Since VMD describes the photon $\leftrightarrow$ hadron fluctuations up to $m_\phi = 1.02$ GeV, it is not unreasonable to have direct processes take over from VMD when the two partons of the scattering have total transverse momentum of $2p_o \approx m_\phi$. The p_T^{min} cut-off described earlier is the requirement for a hard scattering. With $p_o < p_T^{\text{min}}$, and the steep p_T dependence of the cross section, a large direct photon contribution to the total cross section must be dominated by low momentum transfer reactions, that is, it is a source of low p_T events.

As was the case for the anomalous photon, the direct photoproduction is governed by the QCD mass scale $\Lambda \sim 200$ MeV allowing virtual photons with $Q^2 \ll \Lambda^2$ to be treated as real photons

to good approximation. Again, as for the anomalous photon, this issue, also for high Q^2 photons, is examined in [38].

3.5 Observing the Final Hadronic System in CAL

The final hadronic systems of the $\gamma^* p$ interaction is observed by CAL of the central ZEUS detector, as introduced in Section 1.1. The acceptance of the CAL trigger and RCAL energy requirement (A_{RCAL}) is determined in Chapter 11 for events with tagged photons of 8.5 to 11.5 GeV.

Due to the momentum imbalance of the approximately 10 GeV photon and the 820 GeV proton, CAL is very asymmetric in the $\gamma^* p$ center of mass system. The effect of the boost is conveniently examined by the pseudorapidity, defined by

$$\eta \equiv -\ln \tan \theta/2, \tag{3-15}$$

which is an approximation of the rapidity of a particle,

$$y_{\text{rapidity}} \equiv \frac{1}{2} \ln \left(\frac{E + p_z}{E - p_z} \right). \tag{3-16}$$

Under a boost in the z-direction to a frame with velocity $\beta \equiv \vec{p}/E$, $y_{\text{rapidity}} \rightarrow y_{\text{rapidity}} + \tanh^{-1}\beta$. The shape of rapidity distributions is thus invariant under boosts. For the $\gamma^* p$ system in the HERA frame,

$$\beta = \frac{E_p - E_e}{E_p + E_e} = \frac{820 - 10}{820 + 10} \text{ such that } \tanh^{-1}\beta = 2.2. \tag{3-17}$$

The angle $\theta^* = 90°$ in the $\gamma^* p$ center of mass system, corresponds to $\eta = 2.2$ or equivalently $\theta = 12.6°$ in the ZEUS detector. The geometric acceptance of CAL corresponds to $23° < \theta^* < 179.6°$.

The rapidity distribution of the particles from three VMD processes is shown in Figure 3-4. All three types of processes are seen to deposit energy in RCAL. As seen in the FCAL energy distribution of the data sample in Figure 11-6, the rapidity distribution indicates that a division of the event sample into those without and those with FCAL energy can separate a sample of diffractive events from the remaining types, respectively. Though imperfect, the separation simplifies the determination of A_{RCAL}. Quantities referring to the **diffractive-like** events, $E_{\text{FCAL}} < 1$ GeV, carry the superscript FCAL<1. Quantities referring to the remaining **nondiffractive-like** events,

$E_{FCAL} \geq 1$ GeV, carry the superscript FCAL>1. For the total photoproduction cross section measurement, as given by (1-4) and (1-5), the division of events according to FCAL energy leads to

$$\frac{N_{\text{tagged php.}}}{A_{RCAL}} = \frac{N^{FCAL>1}}{A^{FCAL>1}} + \frac{N^{FCAL<1}}{A^{FCAL<1}}. \qquad (3\text{-}18)$$

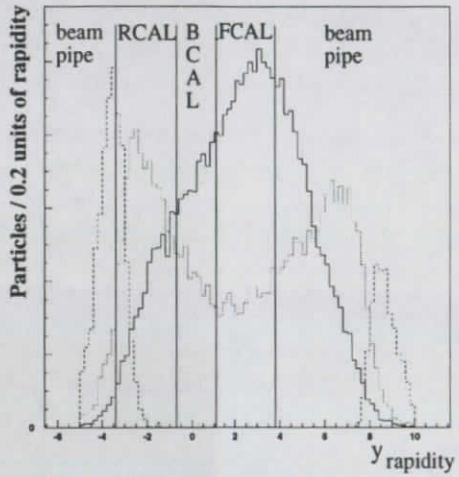

Figure 3-4 Rapidity distribution of final hadronic state particles.
The η-boundaries of the R/B/FCAL geometrical acceptance are shown (see Section 7.1).
Arbitrary normalizations have been applied to these qualitative rapidity distributions of particles from $\gamma^* p$ collisions at ZEUS involving a 10 GeV tagged photon. The distributions have been generated using the PYTHIA event generator (see Chapter 11) with its default parameters.
The decay products of the vector mesons produced in elastic diffraction (dashed line) are accepted by RCAL or escape down its beam pipe. The lightly scattered proton continues to travel in the far forward direction and escapes down the FCAL beampipe.
For double diffraction (dotted line), the particles from the diffracted photon enter mainly RCAL and BCAL, while the bulk of particles from the diffracted proton escape down the FCAL beam pipe with some observed in FCAL.
The particles of non-diffractive events (solid line) are observed everywhere in CAL, but mainly in FCAL. The distribution peaks for transverse particles in the $\gamma^* p$ center of mass system, corresponding to $\eta = 2.2$ in CAL.
Figure courtesy of Maciej Krzyzanowski.

4 Measuring Photon-Proton Cross Sections using Electron-Proton Collisions

Virtual photons from electrons in collision with protons can be used to measure the cross section of real photons in collision with protons. The validity of this equivalent photon approach requires the EPE derived in Chapter 2 and the description of the photoproduction processes given in Chapter 3.

The arguments presented here are but a summary of those by Budnev et al. in [27], the definitive paper for the application of the equivalent photon approach in two photon physics at e^+e^- and e^-e^- colliders. The discussion in [27] detailing the application to ep physics has only been recently been rediscovered for photoproduction physics at HERA. An introduction and references to the history of the equivalent photon approach may also be found in [27].

4.1 Kinematic Constraints

The $W_{\mu\nu}$ tensor of (2-43) describing the $\gamma^* p$ collision in the EPE must be well behaved as $Q^2 \to 0$. Using $P \cdot q = m_P \nu$ of (2-21) and the definition $Q^2 \equiv -q^2$ of (2-13), the requirement simplifies to:

$$[-W_2 \nu / Q^2 + W_1] / Q^2 \text{ is regular as } Q^2 \to 0. \qquad (4\text{-}1)$$

For the two independent functions $W_{1,2}(\nu, Q^2)$ of $W_{\mu\nu}$, W_1 can therefore be finite at $Q^2 = 0$, while

$$W_2 \to 0 \text{ and } [-W_2 \nu / Q^2 + W_1] \to 0 \text{ as } Q^2 \to 0. \qquad (4\text{-}2)$$

Substituting this result into the expressions in (2-57) for the transverse and longitudinal $\gamma^* p$ cross sections yields:

$$\sigma_T \to \sigma_\gamma \text{ and } \sigma_L \propto Q^2 \text{ as } Q^2 \to 0, \qquad (4\text{-}3)$$

where σ_γ is the γp cross section for real photons. As $Q^2 \to 0$, the virtual photons behave like real photons, as one would intuitively expect.

4.2 The Characteristic Scale for the Virtual Photons

The obvious result of the previous section, arising from kinematic constraints, is insufficient to show the applicability of the equivalent photon approach. The Q^2 dependence of the virtual photon cross section is required. The dependence may be approximated in terms of $Q^2/\Lambda^2_{\gamma^*}$, where Λ_{γ^*} is referred to as the characteristic scale of change. Of interest here, for the cross section

of the collision with protons, is the Q^2-dependent difference between a real photon and a transverse virtual photon,

$$|\sigma_T - \sigma_\parallel|/\sigma_\gamma \leq Q^2/\Lambda^2_{\gamma^*}, \tag{4-4}$$

and the Q^2-dependent magnitude of the longitudinal photon,

$$\sigma_L/\sigma_T \leq Q^2/\Lambda^2_{\gamma^*}. \tag{4-5}$$

The VMD photon explicitly provides its Q^2 dependence in (3-3). The characteristic scale of change for VMD photons is $\Lambda_{\gamma^*} = m_V \sim 1$ GeV. Similarly, the scale for the anomalous resolved and the direct photon is $\Lambda_{\gamma^*} = \Lambda_{QCD} \sim 0.2$ GeV from Sections 3.3 and 3.4. Therefore, as long as $Q^2 \ll \Lambda^2_{\gamma^*}$, the virtual photon is very similar to a real photon. In other words, the interactions of real photons can be well measured using virtual photons with $Q^2 \ll \Lambda^2_{\gamma^*}$. Numerical validations of the above result can be found in [17][46].

For example, for the VMD photon as given in (3-3):

$$\sigma_L/\sigma_T \sim Q^2/m_V^2. \tag{4-6}$$

The factors of y multiplying σ_L and σ_T in the EPE of (2-63) are of order unity. Therefore when determining σ_T from ep scattering, σ_L is negligible for $Q^2 \ll m_V^2 \sim 1$ GeV^2. Similarly, the Q^2 dependence of σ_T in (3-3) is obviously extremely small for $Q^2 \ll m_V^2$.

4.3 Using the EPE

Ignoring the conclusion of Section 4.2 for the moment, the equivalent photon approach would require $\sigma_T(y, Q^2)$ and $\sigma_L(y, Q^2)$ of the EPE in (2-63) to be determined using the measured ep events. With the implicit constraint $Q^2 \geq Q^2_{min}$, $\sigma_T(y, Q^2)$ would then have to be extrapolated down to $Q^2 = 0$, in order to determine the photoproduction cross section for real photons.

Fortunately, the conclusions of Section 4.2 make the equivalent photon approach much more robust, and allows for the approximations presented in Section 4.4. Namely, for virtual photons with $Q^2 \ll \Lambda^2_{\gamma^*}$, σ_L is small, as is the effect of the extrapolation to $Q^2 = 0$.

While the approximations are invaluable for manual calculations, the EPE of (2-63) is usually used where the convenience of approximation is irrelevant, for example in computer calculated cross sections or event generation. This is made possible by parametrizations of $\sigma_{T,L}(y, Q^2)$. The validity of the approximations can thus also be verified. Q^2 distributions for photoproduction, as well as $\sigma_L(y, Q^2)$ have not yet been measured at HERA energies, so the parametrizations are also based on the characteristic scales Λ_{γ^*} described in Section 4.2.

4.4 The Equivalent Photon Approximation

The comparison of ep scattering, shown in Figure 2-1, to a γp collision, shown in Figure 2-3, gave rise to the EPE. Thanks to the conclusion of Section 4.2, ep scattering with $Q^2 \ll \Lambda^2_{\gamma^*}$ can neglect the fact that the exchanged photon is not massless, nor purely transversely polarized. The ability to neglect these deviations from a real photon leads to the equivalent photon approximation (EPA) for ep scattering:

$$\frac{d^2\sigma_{ep}(y, Q^2)}{dy dQ^2} = \frac{\alpha}{2\pi}\frac{1}{Q^2}\left(\frac{1 + (1-y)^2}{y} - 2\frac{(1-y)}{y}\frac{Q^2_{min}}{Q^2}\right)\sigma^{\gamma p}_{tot}(y). \tag{4-7}$$

where $\sigma^{\gamma p}_{tot}(y)$ is the total γp cross section at the center of mass energy $W = 2\sqrt{yE_eE_p}$.

Performing the integration over Q^2, with Q^2_{max} given by the experimental conditions, within the implicit constraint $Q^2_{max} \ll \Lambda^2_{\gamma^*}$, provides the EPA in the form:

$$\frac{d\sigma_{ep}(y)}{dy} = \frac{\alpha}{2\pi}\left[\frac{1 + (1-y)^2}{y}\ln\frac{Q^2_{max}}{Q^2_{min}} - \frac{2(1-y)}{y}\left(1 - \frac{Q^2_{min}}{Q^2_{max}}\right)\right]\sigma^{\gamma p}_{tot}(y). \tag{4-8}$$

Therefore, F^e_γ of (1-5) is given.

After performing the above derivation of the EPA, corroboration was found in [47], which presented the first explicit covariant derivation of the equivalent photon approximation. As discussed below, this rediscovery of the EPA led to the demise of the expression for F^e_γ used previously for photoproduction at HERA.

4.5 The Weizsäcker-Williams Approximation

If only the ln term of (4-8) is kept, which is equivalent to ignoring the mass of the electron, the Weizsäcker-Williams approximation (WWA) results. Though the WWA survived numerous photoproduction articles in two HERA workshops [48][49], two measurements of the total photoproduction cross section at HERA using tagged ep events [14][15], and a photoproduction cross section measurement using untagged ep events [50], it should not have been used [51]. Using the WWA, instead of the EPA, introduced a -7 % and a -5 % overestimate of F^e_γ and a corresponding underestimate of the photoproduction cross sections from the tagged and untagged ep events, respectively. H1 concurs [52].

4.6 Factorization of the Acceptance

According to Section 4.2, at a given photon energy as given by y or W (see (2-28),(2-29)), the final hadronic state of tagged photoproduction has negligible Q^2 dependence. In addition, due to the small scattering angle of the electrons accepted in LUMIE, the γ^* essentially travels in the

direction of the electron beam. The range of travel is too small to significantly boost the $\gamma^* p$ system away from the beam axis. Therefore, for tagged photoproduction at a given photon energy, the final hadronic state is independent of the scattered electron as are their respective acceptances in the central ZEUS detector and in LUMIE. Returning to (1-4), this may be expressed as

$$A_{\mathrm{LUMIE*RCAL}} = A_{\mathrm{LUMIE}} A_{\mathrm{RCAL}}, \qquad (4\text{-}9)$$

where $A_{\mathrm{LUMIE*RCAL}}$ is the acceptance for events observed in coincidence in LUMIE and RCAL. Since A_{RCAL} has little W dependence in the narrow W range of this measurement, (4-9) can be used. Though not strictly required to determine the acceptance of tagged photoproduction events, the independence of the two acceptances allows each to be studied in much greater detail than would otherwise be possible.

5 The Electron-Proton Collider HERA

The Hadron Electron Ring Accelerator (HERA) [3] is the first and only electron-proton (ep) collider in the world. It is built in a tunnel of 6.3 km circumference $10-25$ m underground. The tunnel contains two separate rings. One accelerates and stores a proton beam, the other an electron beam. HERA can in principle accelerate and store positrons, instead of electrons, but this thesis is limited to electrons. The proton ring lies above the electron ring, except at the two interaction points on opposite sides of the tunnel. There the beams are brought into collision at 0° to provide ep interactions to the H1 detector [2] and to the ZEUS detector, described in Chapters 6 and 7.

The main HERA parameters are summarized in Table 5-1. The design values are given, as are the differences during the fall 1992 running period (F1992) which provided the data for this thesis. As indicated in Table 5-1, the F1992 values for some of the parameters are determined by ZEUS, as described in Chapter 8.

5.1 The Beam Energies and Polarization

The proton beam energy is limited by the strength of the magnetic field provided by the HERA superconducting dipole magnets which must contain the proton beam in its 6.336 km orbit. The magnets should be able to contain a proton beam of up to 1 TeV. The maximum electron beam energy is determined by the superconducting radio frequency (RF) accelerator cavities which replenish the energy lost by the electrons in synchrotron radiation. Enough power can be supplied by the cavities to store an electron beam of up to 35 GeV. The F1992 proton beam energy, $E_p = 820$ GeV, and electron beam energy, $E_e = 26.7$ GeV, provided ep collisions with center of mass energy, $\sqrt{s} = 296$ GeV, an order of magnitude higher than observed previously at fixed target experiments [53].

The relativistic electrons and protons essentially travel at the speed of light, $c = 3.0\times10^8$ m/s $= 30$ cm/ns.

Electrons in a storage ring can become transversely polarized by the emission of synchrotron radiation. The amount of polarization is limited by depolarization effects due to magnet misalignments and orbit errors. Utilizing special orbit corrections, polarization values close to 60% have been achieved at HERA [54]. During the luminosity runs for ZEUS and H1 no efforts were made with respect to polarization by the HERA machine group and zero polarization was consistently measured [54].

Parameters for the beams	Design		Fall 1992	
	electron	proton	electron	proton
beam energy, E_e, E_p(GeV)	30	820	26.7	820
distance between 220 buckets in 6336 m orbit	29 m or equivalently 96 ns for a 10.4 MHz crossing rate			
number of colliding bunches + e- + p-pilot bunches	~ 200 + as required		9 + 1 + 1	
revolution frequency, f (Hz)	47 317			
filling time / life time (hours)	0.25 / ~ 8	0.3 / ~ 8	~ 1 / > 4	~ 5 / > 20
polarization	≤ 92.4 %	negligible	negligible	negligible
circulating currents, I_e, I_p (mA)	58	160	0.5 - 2	
total number of particles	0.8×10^{13}	2.1×10^{13}	$0.7 - 2.6\times10^{11}$	
The following parameters all refer to the beams at the interaction point.				
crossing angle	0°			
vertex displacement x / y (mm)	0		≤ 1	
emittance, ε_x / ε_y (10^{-8} m · rad)	3.4 / 0.69	0.86 / 0.43	4 / 0.3 - 0.4	1 - 2
x Beta function, β_x (m · rad^{-1})	2 @ z = 0	10 @ z = 0	$2.2 + \frac{z^2}{2.2\text{ m}}$	$7.0 + \frac{z^2}{7.0\text{ m}}$
y Beta function, β_y (m · rad^{-1})	0.7 @ z = 0	1 @ z = 0	$1.4 + \frac{z^2}{1.4\text{ m}}$	$0.7 + \frac{z^2}{0.7\text{ m}}$
transverse size, σ_x / σ_y (mm)	0.26 / 0.07	0.29 / 0.07	0.3 / 0.07	0.4 / 0.1
angular spread, σ_x' / σ_y' (mrad)	0.13 / 0.10	0.03 / 0.1	0.13 / 0.04	0.04 / 0.15
In addition, the following parameters have had their F1992 values determined by ZEUS, as described in Chapter 8.				
luminosity, L ($cm^{-2}s^{-1}$)	1.5×10^{31}		$0.2 - 1.6\times10^{29}$	
fraction of particles in satellite bunch	0		0 - 23 %	0
beam tilt, $tilt_x$ / $tilt_y$ (mrad)	0		-3.0 - 0.0 / -1.5 - 0.0	
rms bunch length, l_e, l_p (cm)	0.8	11	0.8	25 - 55
z-vertex width, $\sigma_{z\text{-vertex}}$ (cm)	6		12 - 28	
mean z-vertex, <z-vertex> (cm)	0		-25 - +10	

Table 5-1 Summary of F1992 HERA parameters for the ZEUS experiment.

All parameters are introduced in the text. A range of values is across the F1992 runs.

5.2 Beam Fills, Beam Conditions and ZEUS Runs

The HERA proton beam requires a longer filling time and has a longer lifetime than the electron beam. Therefore the proton beam is filled before the electron beam. After tuning the beams for luminosity at the two interaction points, the ZEUS and H1 experiments may take data. The series of events collected at ZEUS is called a run. Runs are sequentially numbered for identification. A run may continue for the life of an electron beam, but situations internal to the ZEUS experiment may require a run to be prematurely ended and a new run to be started. After the electron beam has decayed and provides insufficient luminosity, the current ZEUS run is ended, the electron beam is dumped and a new electron beam is filled. Similarly, once the proton beam has decayed, the current ZEUS run is ended, the electron and proton beams are dumped and new beams are filled. The beam conditions within a fill, and therefore within a ZEUS run, are considered stable. Beam conditions across fills, and therefore across ZEUS runs, may vary.

5.3 Backgrounds at HERA

In addition to colliding with the particles in the opposing beam, the electrons and protons also collide with the gas remaining in the vacuum of the ring. When this occurs near the ZEUS interaction region the result is so-called **e-background**, accompanying the electron beam, and **p-background**, accompanying the proton beam. The beams do not have finite boundaries, instead the distribution of particles within them is characterized by long tails. Therefore an additional source of e- and p-background is due to the particles in the tails which, if sufficiently displaced from the beam axis, may collide with the beam pipe wall, magnets, collimators or other elements of the beam line.

If created far upstream of the ZEUS detector, p-background can produce muons which accompany and are nearly parallel to the proton beam. These so-called halo muons may be up to several meters off the beam axis.

Cosmic ray muons are also a source of background events to the experiments at HERA. A significant rate of cosmic muons penetrates the 25m of earth above the experimental hall and enters the ZEUS detector.

5.4 The Bunch Structure of the Beams

The particles of both beams are divided into bunches. The positions of the bunches in the beams are called buckets. The 220 evenly spaced buckets are identified by the bunch crossing number (BCN) cyclically 0 through 219. Only 29 m or 96 ns separate the buckets, providing for a 10.4 MHz bunch crossing rate.

HERA has been designed to fill nearly all of the buckets with bunches. During F1992 HERA typically filled only 9 buckets, BCN = 0, 1, ..., 8, with colliding electrons and protons bunches. Typically in BCN = 9, a so-called proton pilot bunch (p-pilot) without an opposing electron bunch provided a p-background sample. Similarly in BCN = 19, a so-called electron pilot bunch (e-pilot) without any opposing proton bunch provided an e-background sample.

5.5 Removing Backgrounds using the Pilot Bunches

Within a run, all electron bunches are assumed to share the same characteristics, other than the measured individual bunch currents. Therefore the amount of e-background observed for the e-pilot bunch is assumed to be linearly related by the electron bunch currents to the amount of e-background expected in the colliding bunches. The characteristics of the e-background events are also assumed to be the same across all electron bunches. The same argument can be made for the p-background, the p-pilot and the proton bunch currents. The HERA machine group continuously measured the currents using inductive coils and provided the results to the experiments.

5.6 The z-vertex Distribution of ep Collisions

The coordinates of the ep collision are denoted as the primary vertex of the event. Secondary vertices at the decay position of particles produced in the collision are not of interest in this thesis.

The right handed ZEUS coordinate system is prematurely introduced here, the definition will be repeated in Chapter 6. The z axis points in the direction of the proton, the y axis points up and the x axis thus points at the center of the HERA ring. The origin is at the nominal ep collision point at the center of the ZEUS detector.

The z coordinate of the primary vertex of the event is the so-called z-vertex. Within a run, the mean z-vertex distribution of the ep collisions is determined by the relative timing of the electron and proton buckets. Nominally the HERA timing is such that the mean z-vertex is at $z = 0$. During F1992, the timing was such that the mean z-vertex was in the range -25 to $+10$ cm across all the runs used in this thesis. The timing shift is the same for all buckets, since the buckets are always evenly distributed around the ring. Thus the mean z-vertex is constant for events within a single run.

Within a run, the width of the z-vertex distribution is determined by the bunch lengths. The electron bunch is much shorter than the proton bunch, so the z-vertex width is approximately half of the length of the proton bunch, since the electron and proton bunches pass through each other with each travelling at velocity c. Though the bunch lengths may change across runs, they are constant within a run.

The z-vertex distribution of events across runs have a width given by the combination of the above two effects.

5.7 Satellite Bunches

The electron bunches of F1992 were followed by satellites [55]. Each primary electron bunch was followed 8 ns later by a satellite electron bunch. The satellites are created near the beginning of the pre-accelerator chain for the electron beam. Electrons, from a 500 MeV linear accelerator, are injected and stored, nominally as a single bunch, in the PIA storage ring which has an RF frequency of 125 MHz = 1/(8 ns) [56]. The fraction of electron current in the satellite varied from 0 to 23% across runs, with an average of about 10 %.

5.8 The Expected Luminosity and the Transverse Properties of the Beam at the Interaction Point

The expected luminosity is given by

$$L_{expected} = \frac{f \sum_{i}^{\text{all bunches}} N_e^{\,i} N_p^{\,i}}{2\pi\sqrt{\sigma_{xp}^2 + \sigma_{xe}^2}\sqrt{\sigma_{yp}^2 + \sigma_{ye}^2}}. \tag{5-1}$$

The revolution frequency of HERA is

$$f = \frac{c}{\text{circumference}} = \frac{2.99792\times10^8 \text{ m/s}}{6336 \text{ m}} = 47317 \text{ Hz}. \tag{5-2}$$

The number of electrons and protons in each bunch is given by $N_e^{\,i}$ and $N_p^{\,i}$. In practice, one often assumes that in each beam all the bunches have the same number of particles. Then one can use the circulating currents in the approximation

$$\sum_{i}^{\text{all bunches}} N_e^{\,i} N_p^{\,i} = N_e N_p = \frac{I_e I_p}{ef\,ef}, \tag{5-3}$$

where e is the electron charge magnitude.

The expected luminosity of colliders usually carries a large error due to uncertainties in the denominator of (5-1). The rms transverse size in coordinate j for beam b is given by σ_{jb}. The angular spread of a beam is denoted σ_{jb}'. The emittance ϵ_{jb} and the beta function β_{jb} provide

$$\sigma_{jb} = \sqrt{\epsilon_{jb}\beta_{jb}} \text{ and } \sigma_{jb}' = \sqrt{\epsilon_{jb}/\beta_{jb}}. \tag{5-4}$$

The emittance, ε_{xe}, is the area of the phase space ellipse populated by the electrons in the beam in the x coordinate, (x, x') with $x' = dx/dz$ near $z = 0$. The other ε_{jb} are similarly defined. The beta function describes the period of particle trajectories in the phase space ellipse.

For cross section and luminosity values, the barn unit, defined as $1\ \mathrm{b} \equiv 10^{-28}\ \mathrm{m}^2$, is often used. The design luminosity at HERA can then be expressed as $L = 15\ \mu\mathrm{b}^{-1}\mathrm{s}^{-1}$.

The specific luminosity is

$$L_{specific} = f/\left(2\pi\sqrt{\sigma_{xp}^2 + \sigma_{xe}^2}\sqrt{\sigma_{yp}^2 + \sigma_{ye}^2}\right) \qquad (5\text{-}5)$$

and is independent of the number of particles in the beams.

The beam size and angular spread describe the distribution of particles in the beam. The beam itself also has two transverse properties. The mean x- and y-vertex of the beam crossing can be displaced from its nominal position at the origin. The beams nominally travel parallel to $x = y = 0$ through the interaction point. During F1992 the beams were tilted off this axis in the ranges given in Table 5-1. The tilt is given with respect to the direction of the electron beam.

5.9 Physics Rates

A crude perspective on the rate of ep events for the HERA design luminosity can be gained from Table 5-2 [57]. The rate of ep events which can be observed is of course lower, once the acceptance of the detector is taken into account, especially for VMD. Unlike the other processes which have the kinematic requirements indicated, a large fraction of the VMD events will have only low transverse momentum and little activity away from the beam pipe. With ~ 1 % of the design luminosity, F1992 had an observable ep event rate below 1 Hz.

		Rate (Hz)
Photoproduction Processes:	VMD	200
	Boson-gluon fusion ($M_{q\bar{q}} > 3$ GeV)	26
	QCD Compton ($M_{qg} > 3$ GeV, $p_T > 2$ GeV)	2
Deep Inelastic Scattering:	Neutral Current ($Q^2 > 100\ \mathrm{GeV}^2$)	0.1
	Charged Current ($Q^2 > 100\ \mathrm{GeV}^2$)	0.001

Table 5-2 Some estimated physics rates at the design luminosity of HERA.

6 The ZEUS Experiment

An overview of the ZEUS experiment [1] is presented. The sections outline for an event:

- the observation by the detector.
- the recognition by the trigger and readout by the data acquisition system.
- the reconstruction and possible selection as a physics candidate.
- the analysis within an event sample.

The final section describes the simulation of events through the above chain.

Chapter 7 will provide further details on the detector components used in this thesis, the calorimeter, the luminosity monitor, the central tracking detector, the veto wall and the C5 counter, all introduced below. Chapter 9 describes the trigger and event selection algorithms and thresholds used to collect a sample of tagged photoproduction events.

6.1 The Detector

The ZEUS detector is hermetic and multipurpose in order to make accurate measurements of the broadest possible range of ep physics. The central part of the detector is shown in Figure 6-1, and is referred to as the central ZEUS detector or simply as the central detector. The asymmetric beam energies of HERA call for an asymmetric detector. The emphasis in the direction of the proton beam generally ensures the best measurement of the kinematically boosted final state of the ep collision.

The ZEUS coordinate system is right handed, with the z axis pointing in the proton beam or forward direction; the electron beam thus points in the rear direction. The y axis points up, thus the x axis points at the center of the HERA ring. The origin is on the nominal beam axis with $z = 0$ at the center of the nominal ep collision point. The standard cylindrical coordinates include the above z, the distance to the beam axis $r \equiv \sqrt{x^2 + y^2}$ and the azimuthal angle ϕ perpendicular to the beam axis beginning in the x direction. The standard spherical coordinates include the above ϕ, the polar angle θ measured from the z direction, and the distance to the origin $\rho = \sqrt{x^2 + y^2 + z^2}$.

The beams, inside the HERA beam pipe, meet at the ZEUS interaction point (IP) at $z = 0$. Electron-proton collisions produce events with particles off the beam axis. The path of a charged particle is measured by the inner tracking chambers, comprising a vertex detector (VXD), a central tracking detector (CTD), and planar drift chambers in the forward (FTD) and rear (RTD) directions. The momentum of the charged particle determines the curvature of its path in the 1.43 T magnetic field produced by the thin superconducting solenoid (COIL) surrounding the CTD. Charged particle identification makes use of the energy loss, dE/dx, observed for the particle in the tracking chambers. For particles passing through the FTD, transition radiation detectors (TRD)

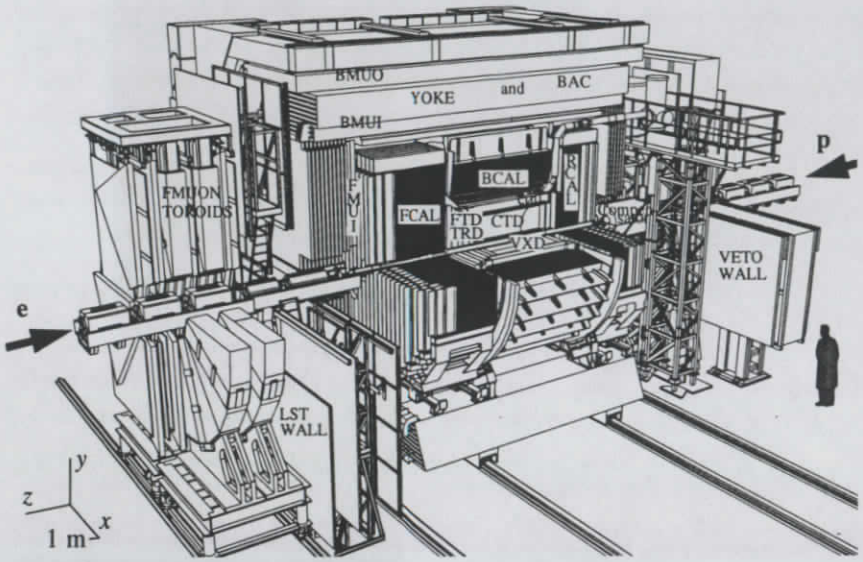

Figure 6-1 Schematic view of the central part of the ZEUS detector.
The view is from inside the HERA ring. One quarter of the detector and half of its YOKE have been cut away. The beam pipe is the symmetry axis of the 10m high, 10m wide and 20m long central detector. The proton beam travels in the positive z-direction, right to left here, with the opposing electron beam in the negative z-direction. The beams meet at the interaction point inside the VXD.

provide additional information for particle identification. The FTD, RTD and TRD were not read out in F1992. A compensating solenoid (Compensator), with a field of 5 T, corrects for any influence that the COIL may have on the colliding beams.

For most of the particles of an event, the energy is captured and measured by the high resolution calorimeter (CAL) divided into a forward (FCAL), barrel (BCAL) and rear (RCAL) part. Other than a 20 cm × 20 cm hole in each of FCAL and RCAL for the beam pipe, the finely segmented calorimeter hermetically encloses the COIL and the inner tracking chambers. A silicon pad detector with 3 cm × 3 cm segmentation at a depth of 3 radiation lengths (3 X_0) in RCAL, known as the RCAL hadron-electron separator (RHES), aids in the identification of electrons. The separation in CAL is possible because electromagnetic showers, from photons or electrons, start early and remain narrow, while hadrons typically interact later and produce wider showers. The RHES was only partially installed for F1992. Space exists for a HES in FCAL and BCAL and their installation will start in 1994.

The iron YOKE, returning the flux of the COIL, is also instrumented as the backing calorimeter (BAC); measuring hadrons not contained by the CAL. In addition, the YOKE is magnetized around the axis of the beam line, such that a muon, after passing through the CAL, has a curved path in the YOKE, allowing its momentum to be determined by the outer tracking chambers in the forward (FMUI), barrel (BMUI, BMUO) or rear (RMUI, RMUO) direction. In the forward direction, toroids, tracking chambers and limited streamer tubes (FMUON) allow the momentum of even very energetic muons to be determined.

The veto wall (VW), 87 cm of iron sandwiched by scintillator and centered at $z = -727$ cm, shields the central detector against p-background.

An assembly of scintillation counters (C5), not visible in Figure 6-1, partially surrounds the beam pipe behind RCAL[58]. C5 measures to better than 1 ns accuracy the arrival time of particles relative to the bunch crossing time. C5 therefore can recognize p-background events and uses e- and p-background events to monitor characteristics of both beams.

A beamline calorimeter, adjacent to C5, measures the energy and position of electrons scattered at small angles[58]. It is not visible in Figure 6-1 and was not read out in F1992.

In addition to the components of the central detector described above, three components are located further away from the IP along the beam line. Figure 6-2 shows the layout of the electron (LUMIE) and photon (LUMIG) calorimeters of the luminosity monitor with respect to the outgoing electron and incoming proton beams. LUMIE and LUMIG measure electrons and photons, respectively, at small angles to the electron beam direction. Such electrons and photons are produced by the Bethe-Heitler bremsstrahlung process used to determine the luminosity. Radiative ep events are another source of photons accepted by LUMIG. LUMIE also accepts the scattered electron of low Q^2 ep collisions, thus providing the sample of tagged photoproduction events of this thesis. Along the forward beamline is the leading proton spectrometer (LPS) and the forward neutron calorimeter (FNC). Six measuring stations at $z = 24, 41, 44, 63, 81, 90$ m and the proton beam line magnets make up the spectrometer which determines the momentum of forward scattered protons. Neutrons produced in the direction of the proton beam remain in the proton beam pipe until the pipe curves upward, at which point the neutrons exit the pipe into the FNC at $z = 105$ m, where their energy is measured. The installation and commissioning of the LPS and an FNC prototype began in 1993.

6.2 The Trigger and Data Acquisition System

The trigger system recognizes if an ep collision of physics interest has occurred in any given bunch crossing. If so, the data acquisition system (DAQ) reads out and archives the event. The number of background events accepted, which may share some experimental signatures with ep

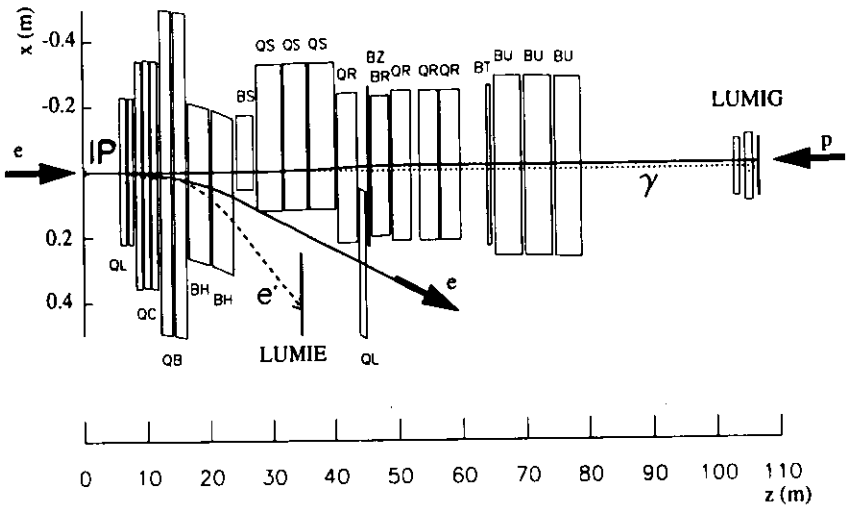

Figure 6-2 Top view of the ZEUS luminosity monitor.
The x and y axes have different scales. The IP is at x = z = 0, though the central detector is not shown. LUMIE and LUMIG are shown with respect to the beam lines and magnets. The magnets labelled Q? focus the beams, while the others, labelled B?, bend the beams. Electrons scattered within a very small angle and with only a fraction of the electron beam energy are deflected by the bending magnets out of the outgoing electron beam pipe into LUMIE. Photons produced in the electron beam direction remain in the proton beam pipe until the pipe and the proton beam curve upward, at which point the photons exit the pipe into LUMIG. The scattered electron (e') and emitted photon (γ) of a Bethe-Heitler bremsstrahlung event, $ep \rightarrow e'\gamma p$, are shown entering LUMIE and LUMIG, respectively.

events, must be kept to a minimum. ZEUS has a three level trigger integrated with the DAQ [59] in order to cope with the short 96 ns between bunch crossings, the large rate of background events, and the large volume of data for each event measured by the ZEUS detector.

6.2.1 The First Level Trigger and Pipelined Data

Signals from each component are continuously sampled and stored in pipelines with a capacity of approximately 58 crossings. Each readout channel has a separate pipeline which may be analogue, as for CAL, or digital, as for the inner tracking chambers.

The signals from each component also enter a local first level trigger (FLT). Each component FLT has 26 crossings to evaluate the data and provide the results to the global FLT (GFLT). Each FLT and the GFLT are also pipelined so that every crossing is examined. Due to the limited processing time available, the component FLT results are fairly simple quantities, usually of limited resolution. Within an additional 20 crossings, the GFLT has applied programmable thresholds and logic operations on combinations of the component FLT results to determine if any of 64 different GFLT trigger types has been satisfied. Each of the GFLT trigger types may be prescaled in order to allow for those types where the event rate exceeds the statistics required for a measurement.

The remaining crossings, approximately 58 – 26 – 20 = 12, of the data pipeline not explicitly used by the FLT, are required for communication, for the digitization and readout of the data described below, and for ambiguous triggers. The latter refers to component FLT results which apply to more than just one consecutive crossing when the component FLT time resolution is too wide to identify just a single crossing.

Dead time, during which the detector is unable to observe a bunch crossing, is monitored by the GFLT. It is a natural choice, since every bunch crossing is tracked by the GFLT which is synchronized with the HERA clock. In addition, the GFLT directly monitors the two sources of dead time. After the GFLT broadcasts the acceptance of an event to the pipeline systems, the ZEUS detector is dead for approximately 10 μs until every component has informed the GFLT that the data has been read from the stopped pipelines and has been written to buffers. The GFLT also recognizes when a higher level trigger or the readout has blocked, since events from the GFLT are no longer accepted. The latter source of dead time is not supposed to occur, provided the output rate of each stage of the trigger is less than its design limit, as given below.

The GFLT is required to accept events at a rate no higher than 1 kHz. Thus for nominal HERA operation, at most one of every 10^4 bunch crossings is accepted. At the maximum GFLT rate, the dead time should be no higher than 1 kHz · 10 μs = 1 %. The dead time is automatically accounted for in the ZEUS luminosity measurement. When the ZEUS detector is dead, the GFLT closes the gate of the luminosity monitor.

For the F1992 runs used in this thesis, the GFLT accepted events at an average rate of 5 to 30 Hz across runs. The GFLT minimized the non-beam related background by vetoing most of the HERA crossings with neither a proton nor electron bunch. The GFLT examined only 15 of the 220 HERA buckets, BCN = 11 to 17 and 21 to 218 were vetoed.

6.2.2 Data Buffers and the Second Level Trigger

The data read out from the pipelines, following digitization if analogue, is copied into data buffers 15 events deep. The copy may be zero suppressed.

The second level trigger (SLT) makes a decision on the event using the contents of the data buffers. With access to almost all of the digitized event data, the SLT can make sophisticated trigger decisions based on the full resolution of the detector. The SLT has access to some quantities,

for example CAL time measurements, that are not available to the FLT. The global SLT (GSLT) also has access to the full event information available to the GFLT.

The data buffers are distributed across many electronics crates, even within large components such as the CTD or calorimeter. Therefore, in order to examine the event and arrive at a trigger decision, the component SLTs and the GSLT are hierarchical transputer networks. This also naturally provides the implicit pipelining needed. The SLT operates most efficiently when approximately 8 events are in the data buffers. The various levels of the SLT are then busy with the different events, and the remaining 7 of the 15 buffers provide for fluctuations in the overall processing time of events. Similar to the FLT scheme, the component SLTs extract results from the event and pass these on to the GSLT, which combines the information in order to arrive at a trigger decision.

The GSLT may output at most a 100 Hz event rate, requiring a factor 10 reduction from the GFLT rate. The bulk of this reduction is due to the recognition and rejection of background events, rather than through more restrictive ep event selection.

6.2.3 The Event Builder

After the GSLT has accepted an event, the corresponding data in the buffers is collected within each component and formatted in a ZEBRA [60] structure. A structure is also filled with the event information of the GSLT, including its copy of the GFLT information. The structures are read out by the event builder (EVB), which combines them within the ADAMO [61] format. The raw event, containing the complete observations by the detector and trigger in approximately 0.1 Mbyte, is then written to one of the third level trigger computers.

6.2.4 The Third Level Trigger

The third level trigger (TLT) is a farm of 30 computers running identical copies of a reconstruction and trigger program. The TLT provides for event rate reduction beyond that of the SLT by using a more sophisticated analysis possible for three reasons: the TLT has more time available per event; furthermore, the complete event data is available and it is given to a single TLT computer, allowing standard Fortran analysis codes to be developed. In fact, some of the codes derive from the off-line analysis codes described below. In comparison, any SLT algorithm is constrained by the fact that not all of the data is available and by the communication limits between the transputers of the SLT network.

The 100 Hz SLT rate must be reduced by the TLT to a 5 Hz output event rate. Accepted events have the results of the TLT algorithms appended, and are archived.

6.2.5 Archived Raw Events

An event accepted by the TLT is read back from its TLT computer and is sent from the ZEUS experimental hall to the DESY mainframe computer, which writes the event onto an IBM cartridge tape. At this point the event has left the on-line environment, and is available for off-line analysis.

Approximately 0.5 Mbyte/s may be archived leading to the explicit limit of 5 Hz on the TLT output rate. There is also an implicit limit to minimize the volume of unnecessary data recorded, since it has to be managed, processed, and analyzed. The 5 Hz rate was sufficient to record all ep physics at F1992 luminosity (see Section 5.9). At full HERA luminosity, kinematic ranges of some physics classes have to be rejected or prescaled by the trigger.

6.3 Reconstruction and Event Selection

Every archived event passes through the ZEUS reconstruction program ZEPHYR [1]. In the reconstruction, the calibration constants of the various detectors are applied to the data and then objects such as tracks and calorimeter clusters are found in the data and measured. The reconstructed data is then examined by a number of physics filters. Every filter sets a bit in the event data, indicating if the event is of interest or not. The result of the reconstruction and event selection is archived with a copy of the original raw data and is known as a reconstructed event. The event selection bits allow the events corresponding to a given filter to be quickly recognized. Since it is impractical to analyze all the archived events, the event selection is essentially a fourth level trigger, using the fully reconstructed events as input.

6.4 The Analysis Environment

An introduction to the ZEUS analysis environment, including references to the programs mentioned below, is given in [62]. The statistical analysis of an event sample generally begins in the EAZE framework which passes the events through the physicist's code which may include routines selected from the PHANTOM pool of analysis routines. A critique of the present scheme and a proposal for a higher level framework by this author may be found in [63]. The event statistics are usually recorded using the CERN HBOOK package and are then interactively analyzed using the CERN PAW program.

Two event display programs allow the physicist to scan and visualize individual events, as recorded by the detector and as reconstructed. GAZE provides a 3D representation, while LAZE specializes in 2 dimensional projections of the event.

6.5 Event Simulation

The efficiencies, acceptances, responses, dead material effects and other performance characteristics of the ZEUS experiment can be determined by passing simulated events through the experimental chain. Other methods, not relying on simulation, are of course also often possible.

Event simulation requires the particles of an event to be generated and then passed through a simulation of the detector and of the trigger. The simulated event is then passed through the same reconstruction, event selection and analysis as used for real events. An introduction to the ZEUS simulation environment, including references to the programs mentioned below, is given in [62].

The events may be generated according to a given kinematic domain of a class of ep physics or they may simply be test particles. The popular event generators for HERA physics, such as HERACLES[91], HERWIG[80], PYTHIA[79], have been integrated into ZDIS, the ZEUS event generator framework, which allows the events, and the information describing their generation, to be easily interfaced to other ZEUS programs.

MOZART tracks the particles of a generated event through the entire detector, obeying, to the significance required, the physics processes such as particle decay, secondary particle generation, energy loss and multiple scattering while simulating the signals of the active components.

ZGANA simulates the trigger, using the signals read out by the detector. ZGANA operates on real data or on the output of MOZART. Real data can be used to verify ZGANA or to investigate new triggers. MOZART data is usually passed through ZGANA in order to determine the trigger acceptance for a class of ep physics.

The simulated events are treated in the same manner as real data through the remainder of the experimental chain, namely ZEPHYR, EAZE, LAZE and GAZE.

6.5.1 Funnel: The ZEUS Simulation Facility

Funnel was originally a set of programs created by this author which allows MOZART to be run in parallel on many workstation computers. Approximately 100 such computers are in use by ZEUS at DESY and funnel uses the otherwise idle CPU time of these machines. Funnel has since been adopted by the ZEUS collaboration and has been extended to automatically pass the MOZART events through ZEPHYR and ZGANA and then be systematically archived. Funnel is also in use by ZEUS collaborators in Bonn, Tokyo, and Manitoba. Nearly all simulated events used by ZEUS, including those in its publications, have been created by funnel.

MOZART is a large, complex, CPU intensive program. ZEPHYR and ZGANA are merely large and complex. Funnel has brought two related benefits to the use of these programs. Physicists are freed from the time consuming and complex task of running these programs and instead can concentrate on the code inside the programs and the resulting events. By having the programs centrally run in a controlled environment, the results are also reproducible. A third benefit is the efficient use of existing computing resources, allowing all ZEUS simulation analyses to enjoy sufficient event statistics. Without funnel, the physics output of ZEUS would be seriously degraded.

7 The Components of the ZEUS Detector used in this Analysis

The calorimeter, the luminosity monitor, the C5 counter, the veto wall and the central tracking detector, as used in this analysis, are presented here in detail. The results and measurements obtained using these components are described in the five following chapters.

7.1 The Calorimeter

The hadronic system of the photoproduction events is measured by CAL, which is also used in the photoproduction trigger and event selection.

7.1.1 Layout

CAL [64][65] is constructed from 1 radiation length (X_0) plates of depleted uranium interleaved with plastic scintillator tiles. The thicknesses of uranium and scintillator have been chosen such that CAL is compensating, giving equal response to hadrons and electrons [66].

An overview of CAL is given in Figure 7-1. The scintillator tiles are arranged into a total of 5918 separate cells, providing fine transverse segmentation and a longitudinal division into an electromagnetic section (EMC) and two (one for RCAL) hadronic sections (HAC). Incident electromagnetic particles, electrons and photons, are contained in the EMC section, distinguishing them from hadronic particles.

FCAL and RCAL each consist of 23 upright modules adjacent on the x axis. A cut-away diagram of an FCAL module is shown in Figure 7-2. BCAL has 32 wedge-shaped modules adjacent in ϕ. The BCAL modules are rotated 2.5° off the lines of constant ϕ, minimizing the probability that a particle from the IP travels down a crack between modules. An FCAL or RCAL cell has physical boundaries that are constants in (x, y, z) cartesian coordinates. Neglecting the ϕ-rotation, BCAL EMC cell boundaries are constants in (r, θ, ϕ) cylindrical-distance and spherical-angle coordinates, while BCAL HAC cell boundaries are constants in (z, r, ϕ) cylindrical coordinates.

Each cell is read out independently on both sides of the module by a wavelength shifter (WLS) bar, which converts the blue scintillator light to green and transmits it to a photomultiplier tube (PMT) at the rear of the module.

7.1.2 Performance

Measurements with test beams [64], for approximately 2000 of the cells, determined CAL to have a sub-nanosecond time resolution and an energy resolution of $\sigma_E/E = 18\%/\sqrt{E} \oplus 1\%$

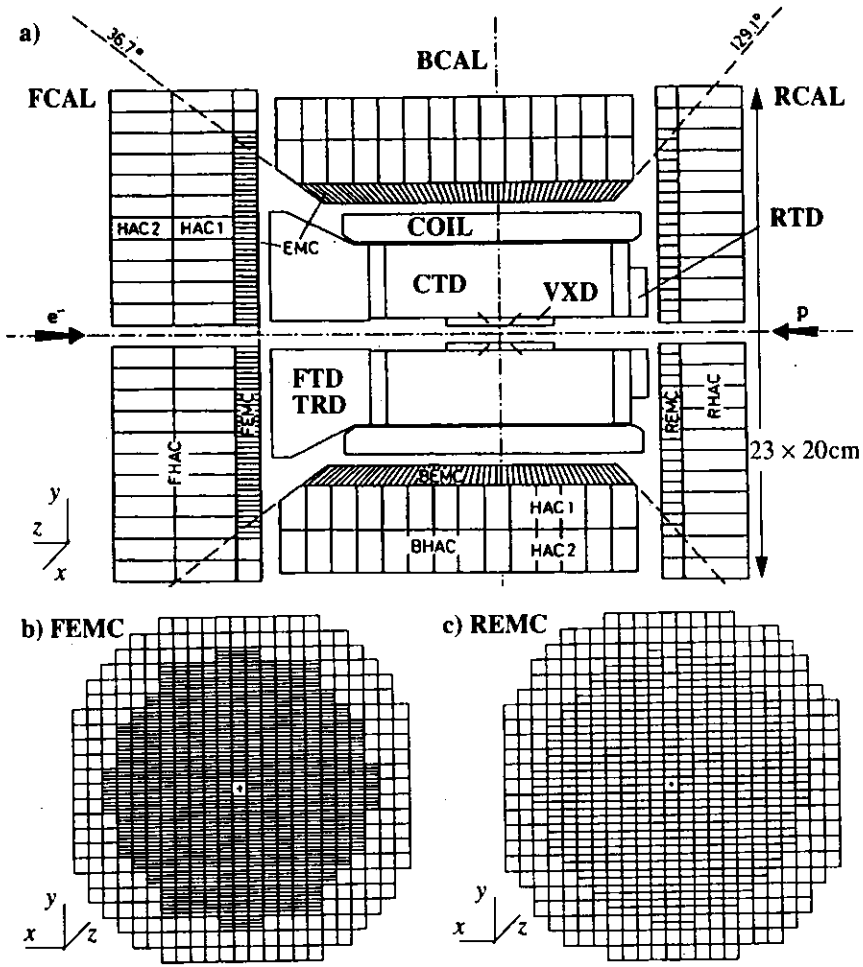

Figure 7-1 Overview of CAL and its readout segmentation.

a) *A longitudinal cut along the beam axis in the y,z-plane outlines the active depth of CAL. FCAL is bound by* $373 \le z \le 222$ cm, *RCAL by* $-148 \le z \le -234$ cm, *BCAL by* $123 \le r \le 230$ cm, *corresponding to 7.1, 5.3 and 4.0 absorption lengths, respectively. The* θ *boundaries for beampipe/FCAL, FCAL/BCAL, BCAL/RCAL, RCAL/beampipe are approximately 2°, 37°, 129°, 177°, respectively. The longitudinal segmentation into EMC and HAC sections is shown, as is the transverse segmentation of typically* 5×20 cm^2 *for FCAL and BCAL EMC cells,* 10×20 cm^2 *for RCAL EMC cells, and* 20×20 cm^2 *for the HAC cells.*

b) *and* **c)** *A transverse cut across the beam axis in the x,y-plane shows the transverse segmentation of the EMC section for FCAL and RCAL respectively. The outer EMC cells, shadowed by BCAL, have the same segmentation as the HAC cells.*

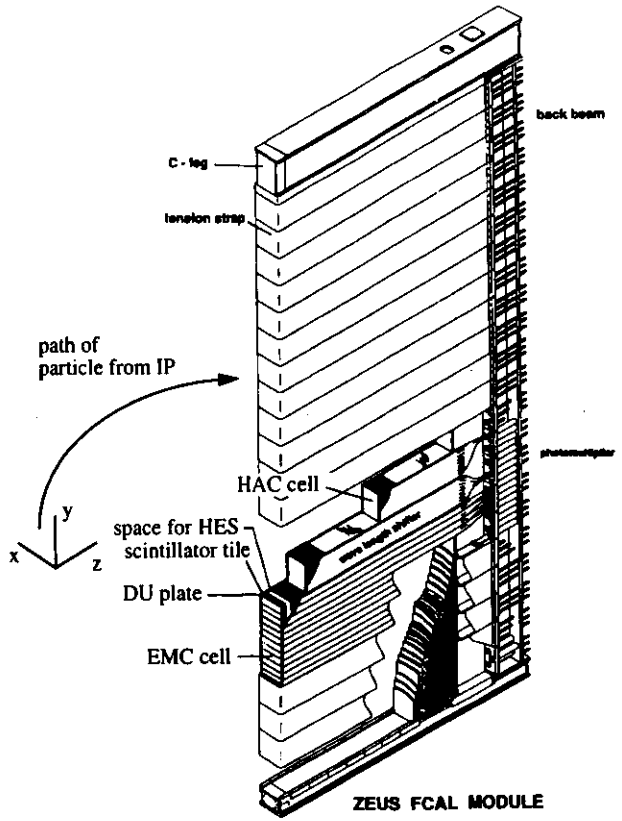

Figure 7-2 Cut-away diagram of an FCAL module.
The module is oriented as installed in the ZEUS detector. The ZEUS coordinates are shown along with a sample particle trajectory into CAL. The active volume, consisting of depleted uranium (DU) and scintillator, has width 20 cm, *height* 23 × 20 cm *and depth* 25 cm (EMC) + 128 cm (HAC) *for the module shown. Most other FCAL and RCAL modules are shorter in height (see Figure 7-1 b) and c)).*
During construction, the module is oriented such that the z-axis points down. A DU-plate, running the full height, and a row of scintillator tiles are alternately stacked onto the back beam. The module shown has 160 such sandwich layers in the HAC and 25 in the EMC. The tension straps are then affixed, followed by the C-legs, completing the mechanics of the module. The wavelength shifter bars and light guides are mounted while individual tension straps are temporarily removed. The module is then complete and may be installed into the ZEUS detector. Access to the PMTs is provided from the back beam. The FCAL HES will be slid in from the top, via an opening in the upper C-leg.

for electrons and $\sigma_E/E = 35\%/\sqrt{E} \oplus 1\%$ for hadrons (E in GeV and $\oplus$ stands for addition in quadrature). These performance characteristics, along with the uniform response throughout CAL and the calibration method discussed below, are due to the quality control and tight tolerances for the components used in the construction of CAL, such as the uranium thickness and the individual scintillator tile response. The high quality of the readout system results in the noise of a cell to be dominated by the products of uranium fission, typically below 15 MeV for EMC cells and 25 MeV for HAC cells [64]. The global effect of the noise on the energy measurement of an event is minimized in the data analysis by ignoring the EMC cells with less than 60 MeV and the HAC cells with less than 100 MeV.

The test beam results[64] also show that the uranium noise of a CAL cell, integrated to give a current, can be used for calibration. The relationship between the uranium current and the response of the cell to electrons, muons and hadrons is constant, to within 1 %, across all the cells calibrated in the test beam. For any given cell, the relationship is also constant, to within 0.5 %, over time. This constant relationship is due to the tight tolerances required for the components used in the construction of CAL. For example, for the response to electrons in the EMC cells, the tolerances on the thickness of the scintillator, the uranium and its steel cladding are such that the expected inter-cell variation for the ratio of the response to electrons and the uranium current is $\Delta(e/\mathrm{UNO})/(e/\mathrm{UNO}) = 0.6\,\%$. Since the relationship between the uranium current and the response of the cell to entering energetic particles was validated for the ~ 2000 cells calibrated in the test beam, the relationship is also used to calibrate the remaining ~ 4000 cells of CAL. In addition, before installation into the ZEUS detector, all the cells were calibrated at DESY using cosmic ray muons. Across all cells, the relationship between the uranium noise and the response to the muons is identical to within 1 % [67]. This validates the relationship for all types of particles measured by CAL, since the muon calibration tracks that of electrons and hadrons to within 1 % [64].

The above calibration accuracy of 1 % for CAL, by using the signal from the uranium radioactivity, can be appreciated when compared to the calibration of more conventional calorimeters. LUMIG and LUMIE are calibrated in situ using the HERA electron beam (see Section 8.2.2). The response of the H1 liquid argon calorimeter depends on many variable factors and is determined in detail using a Monte Carlo simulation, test beam results and measured tracks from physics events [68].

The performance of CAL for both energy and time measurements is continuously monitored by measuring for each cell the response to pedestal triggers, to charge injected to the readout electronics, and to light injected to the PMTs. The uranium noise signal is measured at least once every 8 h, which is a shorter interval than any possible 1 % variation in the gain. The results of the monitoring are used to create calibration constants. The constants which correct effects due to the readout electronics are applied on-line immediately following the digitization. The remaining

constants are applied off-line. A more complete description of the performance of CAL during F1992 is given in [69].

The solid angle coverage of CAL is 99.7 % of 4π. The only sizable inactive material internal to CAL consists of the two spokesplates supporting the BCAL modules. These do not have a large effect on the energy response. Unfortunately, the COIL and the inner tracking chambers present 1 to 6 X_0 of inactive material, depending on θ and ϕ, to particles before entering CAL. The test beam energy resolutions quoted above must thus be used with care, since they are measured without inactive material placed in front of CAL. Therefore, an accurate description of the response of CAL to the energy distribution of an event relies on an accurate description of the inactive material in MOZART.

CAL has a minor technical irritation called sparks, a spurious energetic signal due to occasional discharges between the PMT housing and WLS bar. The F1992 spark rate for the entire calorimeter was approximately 50 Hz for the 15 bunch crossings gated by the GFLT. Therefore, compared to the average crossing rate of 10.4 MHz · 15/220 = 0.71 MHz the chance of a spark in any given crossing, including that of an ep collision, is of order 10^{-4}, negligible for this analysis. Sparks are simply a source of easily recognized background events where only one PMT in the entire calorimeter, including the paired PMT reading out the same cell, claims to observe energy. The time and shape of the spark signal can provide for a more sophisticated identification.

7.1.3 Measurements on the Event

This analysis reduces to a few variables the observations of CAL on the energy distribution of an event. The zero suppression against noise described above is implicit in the definitions given here. E_{FCAL}, E_{BCAL}, E_{RCAL}, are the total energies observed in FCAL, BCAL, RCAL, respectively. Their sum is given by E_{TOT}. The transverse energy observed for the event is defined as $E_T = \sum E_i \sin\theta_i$, where i runs over all cells in CAL, E_i is the energy of a cell and θ_i is the angle from the IP to the center of the cell.

The timing information is reduced to t_{FCAL} and t_{RCAL}, the global times observed in FCAL and RCAL respectively. The time t = 0 for each of the cells, and hence also for the global time, is defined as the time at which a particle emitted from the IP reaches the cell, with negative times for particles arriving earlier, and positive times for particles arriving later. For an ep event,

$$t_{FCAL} - t_{RCAL} \sim 0 \text{ ns}. \tag{7-1}$$

Particles from a p-background event first strike RCAL at

$$t_{RCAL} \sim 2 \cdot -200 \text{ cm}/30 \text{ cm ns}^{-1} \sim -14 \text{ ns} \tag{7-2}$$

and then

$$t_{FCAL} - t_{RCAL} \sim (300 - -200 \text{ cm})/30 \text{ cm ns}^{-1} \sim 17 \text{ ns}. \tag{7-3}$$

later, strike FCAL. Similarly, e-background has the time signature $t_{FCAL} \sim 2 \cdot 300 \text{ cm}/c \sim 20$ ns and $t_{FCAL} - t_{RCAL} \sim -17$ ns. Thus, for events which deposit sufficient energy for a time measurement, CAL time can be used to identify and reject e- and p-background.

7.1.4 Trigger

The calorimeter FLT (CFLT) only makes use of the energies, and not the times, observed in the CAL cells. The F1992 CFLT [70] is just a subset of the nominal CFLT [71]. The EMC and HAC cells are grouped separately into trigger towers, typically with transverse size 20 cm × 40 cm. CAL is divided into 16 regions, as shown in Figure 7-3, with 7 × 8 trigger towers

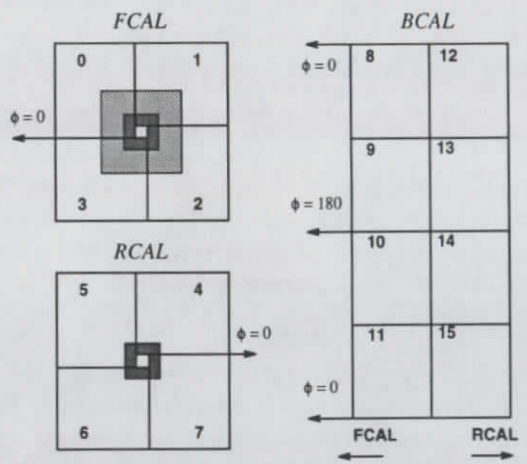

Figure 7-3 The CAL trigger regions.
The views are from the interaction point. FCAL and RCAL trigger regions correspond to four quadrants. BCAL is divided into eight regions. Each region exists separately for HAC and EMC. For FCAL and RCAL, the innermost ring of trigger towers, a 60 cm × 60 cm *area shown darkly shaded, is referred to as the beam pipe region. FCAL is further divided into a inner region, a* 140 cm × 140 cm *shown lightly shaded, and an outer region.*
Figure courtesy of Frank Chlebana.

for EMC and for HAC in each region. A trigger is issued for a region if any of its trigger towers exceeded its assigned threshold.

Beginning with ZEUS run 4145 of F1992, additional CFLT hardware allowed a second, independent, threshold to be assigned to the RCAL EMC trigger towers.

The SLT has access to the energy observed in each calorimeter cell and to the energy weighted average of the time observed for each set of 12 adjacent cells. The TLT has access to the energies and times observed by each of the two PMTs reading out each calorimeter cell.

7.2 The Luminosity Monitor

The luminosity monitor was designed to measure the Bethe-Heitler bremsstrahlung process $ep \rightarrow e'\gamma p$, described in Section 8.2.1. The experimental signature is a coincidence measurement of a photon and an electron, both at small angles to the electron beam direction, with energies adding up to the beam energy, $E_{e'} + E_{\gamma} \simeq E_e$. Thus, the ZEUS luminosity monitor consists of two electromagnetic calorimeters. One measures the bremsstrahlung photon (LUMIG), the other the bremsstrahlung electron (LUMIE). In this analysis, LUMIG also measures the photon from radiative ep events, while LUMIE also measures the scattered electron identifying the low Q^2 photoproduction events. LUMIE is used in the trigger and event selection for the photoproduction sample.

7.2.1 Layout

Photons emerging from the IP at a small angle, $\vartheta_{\gamma} \lesssim 0.5$ mrad, measured with respect to the electron beam direction, may exit the proton beam pipe at $z = -92.5$ m through a 0.1 X_0 Cu-Be window. The photons then pass through a 1.0 X_0 carbon absorber at $z = -103$ m and through a 1.0 X_0 Pb absorber at $z = z_{LUMIG} = -107$ m before entering LUMIG immediately behind the Pb. The absorbers protect LUMIG from the synchrotron radiation accompanying the electron beam.

Electrons scattered by the ep interaction within an angular range $\vartheta_{e'} \lesssim 6$ mrad, measured with respect to the electron beam direction, and within the energy range $0.2 \lesssim E_{e'}/E_e \lesssim 0.9$, are deflected by the electron beam magnets into an orbit of smaller radius than that of the electron beam. The scattered electrons emerge from the beam pipe through a thin steel window at $z = -27.3$ m and enter LUMIE at $z = -35$ m. These acceptance boundaries for the scattered electrons define the kinematic limits, $0.1 \lesssim y \lesssim 0.8$ and $Q^2 \lesssim 0.2$ already shown in Figure 2-2, for tagged photoproduction at ZEUS.

LUMIG and LUMIE are both lead scintillator sandwich calorimeters using 5.7mm thick Pb plates interleaved with 2.8mm thick SCSN38 tiles. LUMIG uses 180 mm × 180 mm plates and tiles with a total depth of 22 X_0, the corresponding LUMIE numbers are 250 mm × 250 mm and 24 X_0. An electron or photon entering LUMIE or LUMIG, respectively, produces an electromagnetic shower of secondary electrons and photons. The electrons produce scintillation light in the

tiles which is read out on two sides by a lucite wavelength shifter bar feeding a PMT. The calorimeters are identical except where noted and are quite similar to a single cell of CAL.

LUMIG has a hodoscope position detector installed at a depth of 7 X_0. There the energy deposited by the shower is at its maximum and can be observed in two orthogonal layers of 1 cm wide scintillator strips read out by silicon photodiodes. A similar position detector was installed in LUMIE following the F1992 running period.

7.2.2 Performance

Using an electron test beam with energy range 1 to 6 GeV, the measured energy resolution of LUMIG and LUMIE is $\sigma_E = 18\% \cdot \sqrt{E}$, E in GeV, with 1 % uniformity in the fiducial volume and better than 1 % response linearity. For LUMIG, the above resolution does not include the effect of the synchrotron radiation absorbers. The absorbers degrade the energy measurement, especially for incoming photons with less than 5 GeV. The test beam results also showed that photons above 5 GeV have their impact position on LUMIG determined by the hodoscope to better than 0.3 cm resolution.

Both calorimeters were continuously monitored by measurements of the pedestal signal, and of the response to charge injected to the readout electronics and to light injected to the PMTs. The absolute energy calibration of the LUMIG and LUMIE calorimeters, as well as their respective acceptances for electron and photons are determined in situ as described in Chapter 8.

7.2.3 Measurements on an Event

The signals observed in LUMIG are fed to analogue to digital converters (ADC). The energy deposited in LUMIG, approximately in the range $E_{LUMIG} \sim 0 - 40$ GeV, has a linear correspondence to the ADC counts, $0 \leq ADC_{LUMIG} \leq 255$, expressed as

$$E_{LUMIG} = gain_{LUMIG} \sqrt{(ADC^{+}_{LUMIG} - pedestal^{+}_{LUMIG}) \cdot (ADC^{-}_{LUMIG} - pedestal^{-}_{LUMIG})}, \qquad (7\text{-}4)$$

where + and - superscripts for the two PMTs, $pedestal_{LUMIG}$ is an offset and $gain_{LUMIG}$ is for the conversion to GeV. The same relationship holds between E_{LUMIE} and ADC_{LUMIE}. The determination of the absolute calibration between energy and ADC counts is described in Chapter 8.

The impact position for photons entering the LUMIG, as measured by the position detector, is given by x_{LUMIG} and y_{LUMIG} in terms of the ZEUS coordinate system.

7.2.4 Trigger

ADC_{LUMIG} and ADC_{LUMIE} are available on-line to all trigger levels. The energy calibration and hence E_{LUMIE} and E_{LUMIG} are available off-line to the event selection and analysis.

7.2.5 Environmental Records

In addition to the readout of events described in Section 6.2.3, ZEUS archives so-called environmental records. These describe the conditions of the experiment. In order to determine the luminosity, the luminosity monitor measures aspects of almost every bunch crossing. This information is collected and archived approximately every 10 seconds as a luminosity environmental record.

7.3 C5

C5 measures the arrival time of particles predominantly from e- and p-background. C5 has three applications. In the first, it identifies individual events as p-background which are thus denoted as **C5-background**. In this analysis, the C5-background, a subset of the p-background, is used to verify the treatment of the p-background (see Section 10.4.3).

The more important analysis function of C5 is its ability to determine characteristics of the beams using the distribution of arrival times of particles from e- and p-background (see Section 8.1). The e- and p-background rates are large, allowing detailed information on the beams to be accurately extracted. In its third application, C5 is the main on-line background monitor while ZEUS is collecting data.

7.3.1 Layout

C5, situated at $z = -315$ cm, is an assembly of four scintillator counters in two U-shaped planes which are separated by 0.3 cm of lead. The planes are perpendicular to the beampipe and partially surround it [58]. Each scintillator is read out by a PMT. Only energetic particles are of interest, so only signals coinciding on opposite sides of the lead sheet are used. Additional lead sheets in front of and behind C5 protect it from synchrotron radiation.

7.3.2 Measurements on an Event

C5-background is in time with the proton beam, $2 \cdot -315 \text{ cm}/30 \text{ cm ns}^{-1} = -21$ ns before particles arriving from the beam crossing at the IP.

For the runs used in this analysis, the C5 rate, as measured by the GFLT, was 200 to 400 Hz, of which the major fraction was due to C5-background (see Figure 8-1). The F1992 p-bunch crossing rate was 10.4 MHz $\cdot$ 10/200 $\approx$ 500 kHz. Therefore less than 0.1 % of

p-bunches were accompanied by C5-background and thus the number of accidentally misidentified ep events is negligible.

Although the identification of an event as C5-background is available at the GFLT, this identification is only used in the analysis of the event sample, as described in Chapter 10.

7.4 The Veto Wall

The VW, centered at $z = -727$ cm, shields the central detector against p-background. The majority of particles entering the iron wall are absorbed, the remaining particles, passing through the wall and on to the central detector, are signalled and denoted here as **VW-background**. The VW-background is used in the same manner as the C5-background described above, namely to verify the treatment of p-background.

7.4.1 Layout

The VW is an 800 cm (width in x) $\times$ 900 cm (height in y) $\times$ 87 cm (depth in z) iron wall sandwiched by two layers of scintillator. The VW is positioned to cover the shadow of the HERA tunnel exit to the ZEUS Hall. The HERA beam elements pass through an 80 cm $\times$ 80 cm hole near the center of the wall. The p-background passing though the hole must be recognized by other ZEUS components.

Each side of the VW is covered by an arrangement of 48 scintillator strips. Each scintillator strip has a length of 260 cm, width of 33 cm, and thickness of 2 cm. Each scintillator strip is read out on both ends by a light guide and PMT.

7.4.2 Measurements on an Event

The comments on the VW-background measurement are essentially identical for the C5-background. VW-background requires a coincidence of signals from scintillator strips on opposite sides of the VW. The signals precede those of particles arriving from the IP by $2 \cdot -727 \text{ cm}/30 \text{ cm ns}^{-1} \sim -48$ ns. The GFLT VW rate was 100 to 500 Hz. Therefore, a negligible number of ep events were accidentally misidentified as VW-background.

7.5 The CTD

The CTD records the tracks of charged particles. The tracks can be extrapolated toward the beam axis and have their information combined in order to determine the primary vertex of the event. As described in Section 11.2.1, the z-vertex distribution, as determined by the CTD for the photoproduction event sample, is corroborated by the distribution predicted by C5. In the off-line analysis, the CTD was also used to identify and reject cosmic muons.

Perhaps a more important function of the CTD for this analysis, and certainly a more interesting aspect, is its contribution to the visualization of the events in the LAZE or GAZE displays.

7.5.1 Layout

The CTD is a drift chamber with 4096 sense wires in 9 cylindrical superlayers. The superlayers are divided azimuthally into cells, each with 8 sense wires and a maximum drift time of 500 ns. The superlayers are consecutively numbered, the innermost is 1, the outermost is 9. The five odd numbered superlayers have wires parallel to the beam axis. The other four have wires at a $\sim 5°$ stereo angle, providing z-by-stereo measurement and a roughly equal resolution of the polar and azimuthal angles θ and ϕ.

7.5.2 Performance

During F1992, only z-by-timing readout electronics of the axial superlayers 1, 3, 5 was present, limiting track hit resolution to 4 cm in z and 0.1 cm in ϕ. The measured z-vertex of the event, z-vertex_{CTD}, has a resolution of $\sigma_z = 2$ cm. The transverse coordinates of the vertex are measured with resolution $\sigma_x = \sigma_y = 0.6$ cm.

8 The Experimental Conditions for ZEUS at HERA

This chapter describes characteristics of the F1992 HERA beams relevant to this thesis, including the determination of the luminosity delivered to the ZEUS experiment. Effects which must be taken into account for the photoproduction trigger and event selection algorithms are introduced. The performance of the ZEUS luminosity monitor and of the C5 counter is described, since they are used to determine the HERA beam characteristics.

8.1 C5 Observations on the HERA beams

The C5 measurement of the time distributions of particles from the e- and p-background allows the HERA bunch structure and timing to be determined. The technique and its F1992 results are described in [55]. The particles of e- and p-background observed by C5 are assumed to have the same distribution along the beam axis as the electrons and protons in the beams. The C5 time spectrum, shown for a typical run in Figure 8-1, observes the proton bunch, the electron bunch, and the electron satellite bunch. A single spectrum was recorded for each run, combining data from all colliding and pilot bunches, which are assumed to share the same bunch structure.

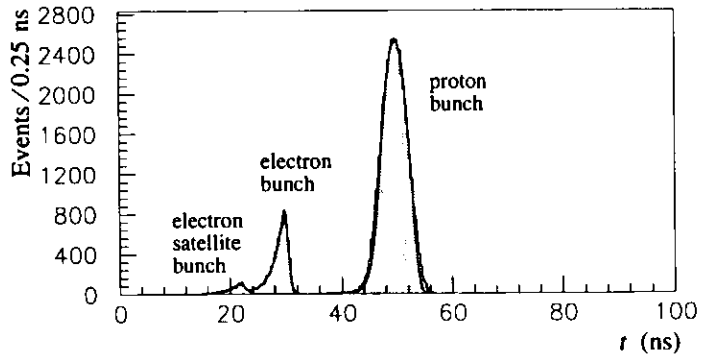

Figure 8-1 The C5 time spectrum of run 4211.
The C5 time runs backwards, it decreases as time progresses.
The proton bunch, seen in the peak (t_p = 49 ns, rms_p = 1.8 ns), arrives at C5 first.
The electron bunch, with its events in the peak (t_e = 30 ns, rms_e = 0.7 ns), is followed by the electron satellite bunch, in the small peak at (t_{sat} = 22 ns).
In this typical run, the fraction of electrons in the satellite bunch is 11 %.

The electron bunch, of length l_e, passes by C5 in $l_e/c = 0.03$ ns which is much narrower than the width of the C5 electron peak, rms_e. Therefore, rms_e is a measure of the C5 timing res-

olution. Since the width of the proton peak, rms_p, is much greater than that of the electron, rms_p is a measure of the proton bunch length.

Particles from the electron bunch have the same timing at C5 as particles from an ep event. Therefore, Figure 8-1 graphically demonstrates how cleanly C5 identifies C5-background.

8.1.1 The Electron Satellite Bunch

The electron satellite and proton bunches meet near $z - 8\ \text{ns} \cdot c/2 - 120\ \text{cm}$. The resulting ep collisions are too far from the IP to be well measured by the detector and to have a well understood acceptance. The ep events are therefore removed from the data sample by timing and vertex cuts as described in Sections 9.4.2 and 10.5. The luminosity due to the electron satellite bunch is also removed, as described in Section 8.3, using the fraction of electrons in the satellite bunch as determined on a run by run basis.

8.1.2 The Width and Mean Position of the z-vertex

The z-vertex distribution of the ep collisions is required for two reasons. It determines the requirements of the timing cut of CAL. It is also required to determine the acceptance in CAL for the final hadronic system of the ep interaction. As shown in Figure 11-1, the acceptance can have a strong z-dependence.

The width of the z-vertex distribution is half the length of the proton bunch, $rms_p \cdot c/2$. The electron bunch, arriving at time t_e at C5, and the proton bunch, arriving at t_p, meet each other at the midpoint of t_p and t_e away from the position of C5. The mean z-vertex is thus given by $(t_p - t_e)\, c/2 - 315\ \text{cm}$.

The distributions of the z-vertex determined by C5 for each run, weighted by the satellite corrected integrated luminosity, are combined to predict the z-vertex distribution for F1992. The resulting distribution is presented in Figure 11-2, where its shape compares well with the distribution of the z-vertex determined by the CTD. In order for the mean of the C5 and CTD distributions to agree, the C5 position must be taken as $z = -310\ \text{cm}$ instead of $-315\ \text{cm}$. The mean z-vertex determined by C5 has a total systematic uncertainty of 5 cm and an RMS uncertainty of 1.8 cm per run [55]. Therefore the mean of the z-vertex distribution determined by the CTD is expected to be more accurate than that of C5.

8.2 The Luminosity Monitor

The performance of the ZEUS luminosity monitor [72] is in part measured using the HERA beams and is in part dependent on the condition of the beams. Tagging the photoproduction electron in LUMIE requires a well understood energy calibration and electron acceptance. The photon

acceptance of LUMIG is required for the determination of both the luminosity and for the acceptance of radiative events.

8.2.1 The Bethe-Heitler Bremsstrahlung Process

Bethe-Heitler bremsstrahlung [73], $ep \rightarrow e'\gamma p$, is the most frequent inelastic process at HERA. Its cross section is given by

$$\frac{d\sigma}{dE_k} = 4\alpha r_e^2 \frac{E_l}{E_k E_e}\left(\frac{E_e}{E_l} + \frac{E_l}{E_e} - \frac{2}{3}\right)\left(\ln\frac{4E_p E_e E_l}{m_p m_e E_k} - \frac{1}{2}\right), \tag{8-1}$$

which is accurate to better than 1 % for the events observed in the luminosity monitor. The variables E_e, E_l, E_p, m_e, m_p have been defined in Table 2-1. The fine structure constant is $\alpha \approx 1/137$ and the classical radius of the electron is r_e. The photon energy is $E_k = E_e - E_l$ to excellent approximation, since almost no momentum is exchanged with the proton. The angle of the emitted photon, ϑ_k, with respect to the incoming electron follows the distribution [74]

$$\frac{d\sigma}{d\vartheta_k} \sim \frac{\vartheta_k}{\left((m_e/E_e)^2 + \vartheta_k^2\right)^2}, \tag{8-2}$$

which peaks near $m_e/E_e \approx 0.019$ mrad. Therefore the bremsstrahlung photon, and the scattered electron balancing the transverse momentum of the photon, exit at very small angles with respect to the incoming electron.

The bremsstrahlung of electrons on the residual gas in the HERA ring, the e-background for bremsstrahlung, has very similar kinematics. Details for the situation at HERA may be found in [75].

8.2.2 Measurement of Photon and Electron Energies

The energy response of LUMIG and LUMIE are calibrated in situ using the Bethe-Heitler process. As described below, the bremsstrahlung photon acceptance in LUMIG is well understood and near 100 %. This allows LUMIG to be calibrated by fitting the observed $\text{ADC}_{\text{LUMIG}}$ spectrum to that expected by MOZART. The result of such a fit is shown in Figure 8-2. The fit is performed using only $\text{ADC}_{\text{LUMIG}}$ above 120 counts, since this endpoint fit is most sensitive to the calibration.

LUMIE is calibrated by requiring that the observed energy for the final state $e'\gamma$ has the electron beam energy, $E_{\text{LUMIG}} + E_{\text{LUMIE}} = E_e = 26.7\ \text{GeV}$. The scatter plot in Figure 8-3 of energies observed demonstrates the correlation when the electron and the photon are both accepted in LUMIE and LUMIG, respectively. The electron and photon are either accepted and

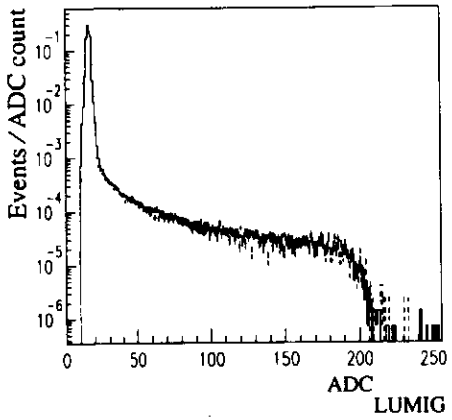

Figure 8-2 The bremsstrahlung photon spectrum in LUMIG.
The measured (solid) and simulated (dashed) spectrum for the bremsstrahlung photon in ADC counts as observed by LUMIG.

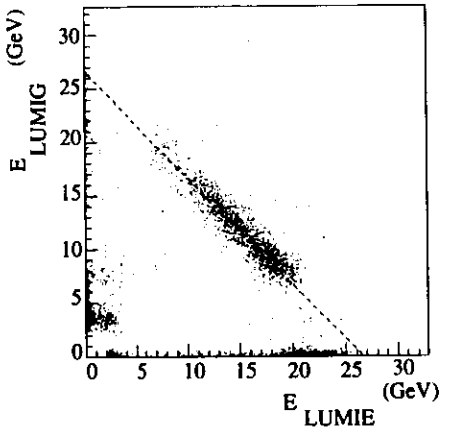

Figure 8-3 Scatter plot of energies measured for bremsstrahlung photons and electrons.
The dashed line, given by $E_{LUMIG} + E_{LUMIE} = E_e = 26.7$ GeV, *shows that the electron beam energy is carried by the bremsstrahlung electron and photon.*
Events along the axes had only the electron or the photon accepted by the luminosity monitor.
The hole at the origin is due to the -2 GeV *threshold required for* E_{LUMIE} *or* E_{LUMIG}.

well-measured by LUMIE and LUMIG, respectively, or are not accepted at all, as seen by the events along the axes. This also holds for the measurement of the scattered electron of tagged photoproduction.

The calibrations are performed on a run by run basis, in order to remove gain instabilities of the PMTs, of order 2 %, due to variations in temperature and beam conditions. The nonlinearity in response due to the absorbers in front of LUMIG is taken into account. The calibrations are correct to within 2 %. The remaining uncertainty is mainly due to possible non-linearities in the response of the calorimeters.

8.2.3 The Photon Acceptance in LUMIG

The acceptance of photons in LUMIG is dominantly determined by the aperture for LUMIG, the beam tilt, the angular spread of the electron beam and the effect of the absorbers in front of LUMIG. A scatter plot of measured photon impact positions on LUMIG is shown in Figure 8-4. The geometric acceptance of LUMIG for photons from the IP has boundaries determined by the HERA beam elements.

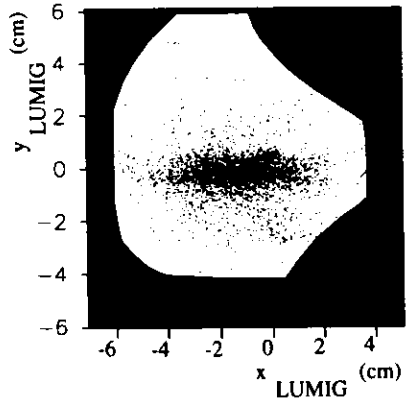

Figure 8-4 The impact position on LUMIG measured for bremsstrahlung photons.
The full face of LUMIG extends from -9 cm *to* 9 cm *in both x and y.*
Only a fraction of the face, the unshaded area, is visible from the IP.
The shaded area is shadowed by beamline magnets.

The distribution in Figure 8-4 is centered horizontally at $x_{\mathrm{LUMIG}} \approx -1$ cm. The x and y vertex of the colliding beams is displaced by at most 1 mm from the origin. Therefore, the displacement of the photon impact position is due to beam tilt in x of magnitude

$$\mathrm{tilt}_x = \frac{\langle x_{\mathrm{LUMIG}} \rangle}{z_{\mathrm{LUMIG}}} \approx \frac{-1 \text{ cm}}{107 \text{ m}} = 0.1 \text{ mrad}. \qquad (8\text{-}3)$$

The beam tilts for each run in F1992 have been determined in this fashion and the range observed is given in Table 5-1.

Extrapolating from the IP to the LUMIG, the angular spread of the electron beam is $\sigma_{x'} \cdot z_{\mathrm{LUMIG}} = 1.4$ cm in x and similarly 0.4 cm in y. Including the scattering angle of the bremsstrahlung photon, which provides a width of 0.02 mrad $\cdot\, z_{\mathrm{LUMIG}} = 0.2$ cm at LUMIG, provides a good description for the width of the distribution observed in Figure 8-4. The transverse size of the beams, $\sigma_{x,y} \ll 1$ mm, has a negligible effect on the photon position in LUMIG.

For bremsstrahlung photons above 5 GeV, the acceptance determined by MOZART is 92 – 99 % with an error 5 – 1 % for large – small beam tilts. MOZART has been checked experimentally to an accuracy of 3 % by comparisons with e-gas bremsstrahlung collected at a variety of beam tilts. The effect of the absorber on the acceptance is well understood since the energy dependence of the photons behaves as expected.

In summary, the photon acceptance in LUMIG, including the energy and angle dependence, is well understood and well described by MOZART.

8.2.4 The Electron Acceptance in LUMIE

The determination of the energy and angle dependent electron acceptance in LUMIE is more difficult than that of the photon in LUMIG. The photon travels in a straight line, while the electron is transported to LUMIE by several quadrupole and dipole magnets. The determination of the acceptance by MOZART requires an accurate simulation of the geometry of the electron beam, the HERA machine elements, and LUMIE.

Bremsstrahlung events were used to validate the MOZART simulation in a limited range of electron angles. Every bremsstrahlung photon observed in LUMIG is expected to be accompanied by an electron of energy $E_e - E_{\mathrm{LUMIG}}$. The fraction of the expected electrons observed in LUMIE is the acceptance in terms of the energy $E_e - E_{\mathrm{LUMIG}}$. The result was compared to that of MOZART. The procedure was refined by using the position observed in LUMIG to determine the angle of the photon, which for these purposes is equivalent to that of the electron. By using data from beams of varying tilt, the MOZART simulation was verified in angular ranges up to 0.5 mrad, corresponding to the outermost geometrical acceptance of LUMIG.

Electrons with angle $\vartheta_e \lesssim 6$ mrad may be accepted in LUMIE. The equivalent boundary for photoproduction electrons is $Q^2 \lesssim 0.02$ GeV^2. In other words, a negligible fraction of electrons with $\vartheta_e > 6$ mrad or $Q^2 > 0.02$ GeV^2 are accepted in LUMIE. Of the photoproduction electrons accepted in LUMIE, approximately half have $\vartheta_e \leq 0.5$ mrad. Confidence in the MOZART simulation for electrons with $0.5 \lesssim \vartheta_e \lesssim 6$ mrad was obtained by being able to successfully simulate the observed photoproduction electron spectrum from a variety of beam tilts. Figure 8-5 presents the comparison of the nondiffractive-like photoproduction event sample, described in Chapter 10, and the MOZART simulation, weighted for the appropriate beam tilts at which the sample was collected.

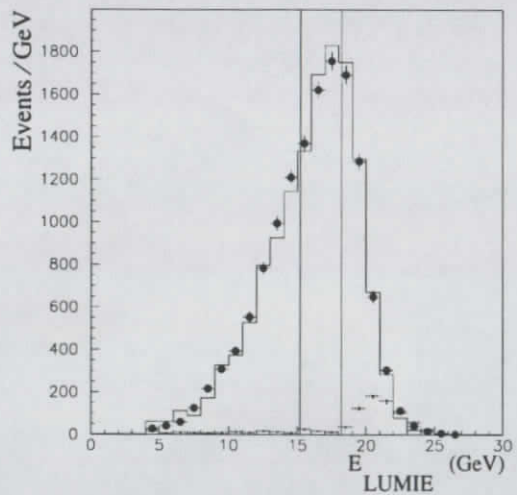

Figure 8-5 The F1992 photoproduction electron spectrum observed in LUMIE.
The data points, with statistical errors, show the measured energy spectrum for the scattered electron of the nondiffractive-like events ($E_{\mathrm{FCAL}} > 1$ GeV) with $E_{\mathrm{LUMIG}} < 1$ GeV in the photoproduction sample (see Chapter 10). Thus, within the vertical lines are the events with $15.2 < E_{\mathrm{LUMIE}} < 18.2$ GeV used for the nondiffractive-like part of the total cross section measurement (see Section 10.7).
The dotted line shows the number of background events due to accidental coincidences with bremsstrahlung (see Section 8.4 and Figure 8-6) that have been statistically removed from the photoproduction candidates in order to obtain the background-free photoproduction sample (see Section 10.4.3).
The solid line is the spectrum predicted by the MOZART simulation of the electron measurement by LUMIE. The simulation does not include the final hadronic system, hence the comparison with the nondiffractive-like sample, which has little W or E_{LUMIE} (see (2-30)) dependence for the acceptance of the final hadronic system in the central detector.

The tagged photon energy range of this thesis, 8.5 – 11.5 GeV given by $15.2 < E_{LUMIE} < 18.2$ GeV, corresponds to a region of relatively flat electron acceptance in LUMIE [72]. For events with a higher scattered electron energy, the acceptance drops rapidly and the number of background events due to accidental coincidences with bremsstrahlung increases (see Figure 8-5). For lower E_{LUMIE}, the number of events decreases, in part due to the electron acceptance in LUMIE, in part due to the nature of the flux of photons accompanying the electron (see (2-63)).

The acceptance in LUMIE for electrons from photoproduction with $Q^2 \leq 0.02$ GeV^2 and $15.2 < E_l < 18.2$ GeV is $A_{LUMIE} = 77$ % with two sources of error. The first, due to the possible 2 % energy miscalibration of LUMIE, can change the number of accepted events by 7 %, in both the event sample and in MOZART. The second source of error is due to the remaining uncertainties in MOZART. These include the beam tilt, varied by ±0.15 mrad, and the ±1 mm uncertainty in x and y for the position of the event vertex, the HERA magnets and LUMIE. Varying the above parameters within their respective ranges of uncertainty, while continuing to be able to reproduce the observed LUMIE electron spectrum, can change the acceptance by up to 5 %. The two independent systematic errors are added in quadrature for the result

$$A_{LUMIE} = 77 \pm 7 \text{ \% for } 15.2 < E_l < 18.2 \text{ GeV and } Q^2 \leq 0.02 \text{ GeV}^2. \tag{8-4}$$

The error is consistent with the level of agreement seen in Figure 8-5.

8.3 The Luminosity Measurement

The luminosity (L) is determined [72] by applying the definition

$$L = \frac{R_{ep}(E_k)}{\sigma_{ep}^{acc}(E_k)} \tag{8-5}$$

to the corresponding rate $R_{ep}(E_k)$ of ep bremsstrahlung photons observed above the energy threshold E_k and the known cross section $\sigma_{ep}^{acc}(E_k)$ corrected for the LUMIG acceptance and resolution. This is much more accurate than the determination of the expected luminosity of (5-1). For F1992 luminosities, bremsstrahlung is observed in LUMIG with negligible effects due to p-background and with manageable e-backgrounds. No coincidence with LUMIE is required to reduce the background. The acceptance in LUMIG has a smaller error than that of LUMIE, so it is more accurate to use only LUMIG.

The e-background rate R_{eA} is subtracted from the total rate $R_{colliding}$ of the colliding bunches. Following the prescription in Section 5.5 yields $R_{ep} = R_{colliding} - R_{eA}$, with

$$R_{eA} = \frac{I_e^{colliding}}{I_e^{e-pilot}} R_{e-pilot}. \tag{8-6}$$

During F1992, R_{eA}/R_{ep} was typically 0.3 and the error introduced to R_{ep} by the e-background is 2.0 %.

The beam tilt dependent photon acceptance in LUMIG and its error was determined on a run by run basis. The resulting error across F1992 is 2 %.

The uncertainty due to the resolution and energy scale of LUMIG is restricted to 2.5 % by the calibration method, test beam measurements and comparisons to MOZART. The energy calibration has also been verified by the ratio

$$\frac{R_{ep}(10 \text{ GeV})}{R_{ep}(5 \text{ GeV})} \Big/ \frac{\sigma_{ep}^{acc}(10 \text{ GeV})}{\sigma_{ep}^{acc}(5 \text{ GeV})}, \tag{8-7}$$

which has a mean of 1.000 and an rms spread of 0.005 for all runs used in this analysis. The ratio of (8-7), but not the luminosity measurement, is corrected for multiple events which occur in fewer than 1 % of the bunch crossings.

The luminosity due to the electron satellite bunch is removed. The specific luminosity at $z \approx 120$ cm is a fraction of that at $z \approx 0$. See the beta function in Table 5-1, and Section 5.8.

$$\frac{L_{specific}(z \approx 120 \text{ cm})}{L_{specific}(z \approx 0 \text{ cm})} = 0.52. \tag{8-8}$$

Therefore for F1992, 12 % of the electrons in satellite bunches produced 6.6 % of the measured luminosity. The subtraction of the luminosity due to the satellite electron bunches is done on a run by run basis. The electron satellite bunches introduce a 1.5 % systematic uncertainty to the luminosity measurement.

Errors in the count of bremsstrahlung events is estimated as 0.5 %.

Table 8-1 summarizes the contributions of the above effects to the systematic uncertainties of the luminosity measurement. Adding the errors in quadrature results in a luminosity uncertainty of 4.3 %. The final value for the integrated luminosity accompanies the description of the photoproduction event sample in Section 10.2.

Origin	Systematic Uncertainty (%)
Bethe-Heitler cross section	1.0
Subtraction of e-background	2.0
Photon acceptance	2.0
LUMIG calibration and resolution	2.5
Multiple Events	1.0
Electron Satellite Bunch	1.5
Counting Error	0.5
Total	4.3

Table 8-1 Contributions to the systematic error of the measured luminosity.

As described in Section 7.2.5, the data required to determine the luminosity is recorded in environmental records. Due to an oversight, runs did not conclude with such an environmental record. Therefore, events recorded past the last record have to be removed from any cross section determination.

8.4 Bremsstrahlung Backgrounds to Photoproduction

A high rate of bremsstrahlung, for both ep and e-background, is observed in the luminosity monitor, as shown in Figure 8-6. The rate due to other processes, including tagged photoproduction, is negligible. The high rate causes **accidental coincidences** of a bremsstrahlung event with another event in the same bunch crossing, leading to two effects.

The coinciding event may be a tagged photoproduction event, in which case E_{LUMIE} and/or E_{LUMIG} are not solely due to the ep event, but are instead inflated by the bremsstrahlung event. Due to the accidental coincidence in the tag of the photoproduction event, some of these so-called **a.c.-tagged** events may be lost from the photoproduction sample and must be taken into account in the total cross section measurement. The E_{LUMIE} and E_{LUMIG} distributions for the photoproduction sample may also have to be corrected.

If the coinciding event is not a tagged photoproduction event, the bremsstrahlung electron observed in LUMIE allows the accidental coincidence of the two events to be mistakenly identified as a tagged photoproduction event. This accidental coincidence background, so-called **a.c.-background**, must be removed from the photoproduction sample.

The E_{LUMIG} versus E_{LUMIE} spectrum for bremsstrahlung was recorded only for ZEUS runs 4272 and beyond.

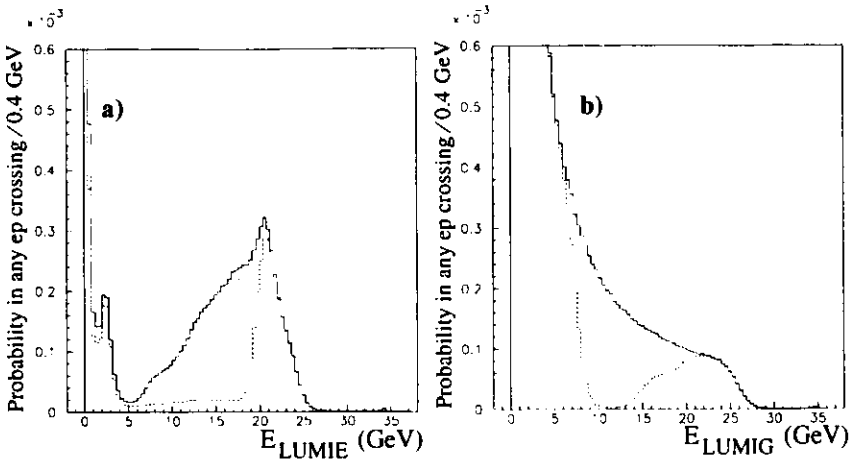

Figure 8-6 Occupancy in LUMIE and LUMIG due to bremsstrahlung.
Shown are projections onto the axes of the E_{LUMIG} *versus* E_{LUMIE} *lego plot of Figure 10-2, where a complete description of the data is given.*

a) *The probability of observing* E_{LUMIE} *due to bremsstrahlung in any given colliding bunch crossing is shown (solid line). Upon integration,* 0.8 % *of crossings have* $E_{LUMIE} > 3$ GeV. *If* $E_{LUMIG} < 1$ GeV *is required (dashed line),* 0.3 % *of crossings have* $E_{LUMIE} > 3$ GeV.

b) *The probability of observing* E_{LUMIG} *due to bremsstrahlung in any given colliding bunch crossing is shown (solid line). Upon integration,* 2.6 % *of crossings have* $E_{LUMIG} > 1$ GeV. *If* $E_{LUMIE} < 3$ GeV *is required (dashed line),* 2.2 % *of crossings have* $E_{LUMIG} > 1$ GeV.

The area between the solid and dashed lines is equivalent in the two plots and corresponds to bremsstrahlung events for which both the electron and photon are observed in the luminosity monitor.

9 The Trigger and Event Selection for Photoproduction

This chapter describes the use of the ZEUS experiment in order to trigger and select events for the measurement of the total photoproduction cross section. The resulting **selected events** are used in Chapter 10 to produce a clean, well understood **photoproduction sample**. Therefore, the selected events include not only photoproduction candidates, but also any and all events required to understand the trigger and analysis cuts and to remove the background from the sample.

9.1 Introduction

In principal, the total photoproduction cross section could be determined by observing just the scattered electron or just the hadronic system.

In LUMIE, bremsstrahlung background overwhelms any attempt to observe just the scattered electron of photoproduction. As an additional complication when ignoring the hadronic system, the cross section for the scattered electron is subject to large radiative corrections. Despite the experimental difficulties, such a measurement does have the elegance of being completely independent of the $\gamma^* p$ processes. For 1993 and onwards, the LUMIE position detector may allow the measurement in the upper part of the Q^2 range of the electron acceptance, where the bremsstrahlung background may be manageable.

The photoproduction cross section could also be measured by observing the hadronic system in the central ZEUS detector. Although the p-background would be substantial, it could in principal be removed using the prescription of Section 5.5. The center of mass energy, W, of the $\gamma^* p$ collision is poorly measured by the central detector, mainly due to particles escaping down the beam pipe. The poor resolution in W makes it difficult to determine the W dependent acceptance of the events, especially since the $\gamma^* p$ processes and their W dependent abundances have to be determined in situ (see Chapter 11). The event is identified as photoproduction by not observing the scattered electron in CAL. The electron escapes down the RCAL beam pipe (see Section 7.1.1) and may have a scattering angle up to the beam pipe boundary of RCAL, where $\vartheta_l \lesssim 3°$, corresponding to $Q^2 \lesssim 2\,(1-y)\ \mathrm{GeV}^2$ by (2-31). Therefore, in order to interpret the observed events in terms of a photoproduction cross section, the possibly large Q^2 values require assumptions which are not needed for the low Q^2 of tagged events (see Chapter 4). DIS ep events are a background which has to be identified using the electron in the central detector and excluded from the photoproduction sample. Given the above caveats, H1 has measured $\sigma_{\mathrm{tot}}^{\gamma p} = 152 \pm 34\ \mu\mathrm{b}$ for $\langle W \rangle = 183$ GeV using untagged events [15].

The measurement of this thesis requires the electron to be observed in LUMIE in coincidence with the observation of the hadronic system in the central detector. The acceptance for both observations contributes to the systematic error, but this disadvantage is greatly outweighed by the

ability of the coincidence measurement to overcome the difficulties of the above approaches. Background events are reduced to an almost negligible level (see Chapter 10). The measured electron energy provides the center of mass energy of the hadronic system observed in the central detector, allowing the physics of the hadronic system, and hence its acceptance, to be well understood (see Chapter 11). Radiative corrections are also negligible in this approach (see Chapter 12).

Some of the arguments presented below for the simplest possible trigger and event selection may seem pedantic. As seen in Table 9-3, the event selection was quite complex in the Summer 1992 and early part of the Fall 1992 luminosity periods. It was simplified following the arguments given below. In general, since the effect of every cut has to be examined and understood, the trigger and event selection should contain only cuts which are absolutely required to reduce the event rate.

9.1.1 Background Events

In addition to tagged photoproduction, two types of background events can satisfy a coincidence of activity in LUMIE and in the central detector.

The first is e-background, which can be removed following the prescription of Section 5.5 using events from the e-pilot bunch. Therefore the BCN must not be examined in either the trigger or the event selection.

The second is a.c.-background, introduced in Section 8.4. These accidental coincidences with bremsstrahlung may involve C5- and VW-background events. The information identifying VW-background and C5-background is not used in the trigger and event selection such that these independently identified background events may be used to verify the treatment of the a.c.-background (see Section 10.4.3).

9.1.2 Requirements in LUMIE

In addition to the obvious requirement that some energy be observed in LUMIE, no further requirements on the luminosity monitor should be made. The effects of the accidental coincidences (see Section 8.4) can then be examined and treated (see Chapter 10).

9.1.3 Requirements in the CAL

At first glance, photoproduction does not have an obvious experimental signature in the central detector, which distinguishes it from p-background events, like the scattered electron of DIS, or the jets of hard scattering.

For the $\gamma^* p$ center of mass energies of tagged photoproduction at ZEUS, the majority of photoproduction events are signalled by energy deposited in RCAL, as seen in the rapidity

distributions of Figure 3-4. This is a powerful criterion, since it allows CAL timing information (see Section 7.1.3) to identify and reject many of the p-background events.

A rough perspective on the RCAL energy can be gained from two examples of the kinematics of photoproduction. The examples are based on the energy of the incoming photon and the geometric acceptance of RCAL. The incoming γ^* of tagged photoproduction essentially travels in the direction of the electron beam and has energy in the range

$$E_{\gamma^*} = E_e - E_l \approx E_e - E_{LUMIE} \approx E_e - (0.2 \text{ to } 0.9)\,E_e \approx (0.1 \text{ to } 0.8)\,E_e \approx 3 \text{ to } 22 \text{ GeV}. \quad (9\text{-}1)$$

The geometrical acceptance of RCAL is restricted to $129° < \theta < 177°$, extending from the BCAL boundary to the beam pipe, respectively. Soft photoproduction processes are affected mainly by the beam pipe boundary, while hard processes are affected by the BCAL boundary.

The effect of the RCAL-beam pipe boundary is greatest for the softest photoproduction process, the elastic ρ scattering of VMD (see Section 3.2.1). Little momentum is transferred in the scattering, so the ρ exits essentially in the direction of the electron beam with the energy of the incoming γ^*. The ρ decays almost exclusively into $\pi^+\pi^-$. The transverse momentum given to the pions in the decay may allow one or both of them to be observed in RCAL. For example, if a 10 GeV $\gamma^* \rightarrow \rho$ decays transverse to the beam axis, each pion has 5 GeV of momentum in the negative z direction and a transverse momentum of $(m_\rho - 2m_\pi)/2 \approx 0.25$ GeV. Hence, each pion moves away from the electron beam direction by only $0.25/5 \approx 3°$, which is at the limit of the RCAL acceptance. Harder processes, such as inelastic diffractive scattering of the photon, producing higher mass states, create particles that are further off the beam axis and that hence have a greater acceptance in RCAL.

The effect of the RCAL-BCAL boundary is most easily examined using the hardest photoproduction process, direct photoproduction, described in Section 3.4. For any tagged photoproduction event at ZEUS, energy and momentum conservation lead to

$$2E_{\gamma^*} \approx \sum_i E_i (1 - \cos\theta_i), \quad (9\text{-}2)$$

where i runs across all CAL cells. The observed transverse energy is given by

$$E_T = \sum_i E_i \sin\theta_i. \quad (9\text{-}3)$$

When the photon couples directly to the partons of the proton, there is no photon remnant. This allows for the reasonable assumption that no particles escape down the RCAL beam pipe. In order

to simplify the argument, assume an event where all the particles observed by CAL have the same azimuthal angle θ_h. Then

$$2E_{\gamma^*} \approx E\,(1 - \cos\theta_h) \text{ and } E_T = E_{TOT}\sin\theta_h, \quad (9\text{-}4)$$

where E_{TOT} is the total energy observed in CAL. Solving for E_T gives

$$E_T = \frac{\sin\theta_h}{1 - \cos\theta_h} 2E_{\gamma^*}. \quad (9\text{-}5)$$

If the particles of the event are at the BCAL boundary then $\theta_h = 129°$ and $E_T \approx E_{\gamma^*}$. E_T increases as θ_h decreases for more forward particles. Therefore, in order for a direct photoproduction event to not place energy into RCAL, all the particles have to be forward of the BCAL boundary and $E_T \gtrsim E_{\gamma^*}$ is required. Cross sections decrease exponentially with increasing E_T. Therefore, only a small fraction of direct events, with $E_T \gtrsim E_q$, may not deposit any energy into RCAL. In a hard scattering, with a photon remnant with energy $E_{remnant}$ escaping down the RCAL beam pipe, a similar argument can be made, but with $E_T \gtrsim E_{\gamma^*} - E_{remnant}$.

9.1.4 Tagged Photoproduction Among Other Physics Measurements

The total photoproduction cross section is of course just one of the many ep physics topics investigated by ZEUS during F1992. Data for the various measurements is collected in parallel, with some parts of the trigger and event selection unique to a given measurement, while other parts are shared. The following presentation of the F1992 trigger and event selection addresses only parts relevant to the total photoproduction cross section measurement. These parts are referred to as the photoproduction trigger and event selection (PTE).

9.2 The First Level Trigger

At the GFLT, the PTE requires the coincidence

$$CFLT_{any} \cdot (ADC_{LUMIE} \geq 40). \quad (9\text{-}6)$$

The condition $CFLT_{any}$ is satisfied when at least one of the trigger towers of CAL, in any trigger region (see Section 7.1.4), observes energy above its threshold as given in Table 9-1. The effectiveness of each type of trigger region for accepting photoproduction events is shown in Table 9-2. The RCAL trigger regions provide 99 % of the photoproduction events, the BCAL regions provide 0.9 %, while the FCAL regions are irrelevant.

Approximately 14 % (2 %) of the events trigger (exclusively) in the RCAL EMC beam pipe trigger towers. The corresponding HAC numbers are 24 % (5 %). Therefore, the trigger is not critically dependent on the geometrical acceptance of RCAL near the beam pipe, which in turn

[GeV]	RCAL		BCAL	FCAL		
	Beam Pipe	Other	All	Beam Pipe	Inner	Outer
lowEMC	1	0.4	-	-	-	-
EMC	10	2.5	2.5 / 1	50	20	10
HAC	2.5	1	1	70	25	10

Table 9-1 F1992 CFLT trigger tower thresholds in each region.

All trigger towers within a given region had identical thresholds, given above in GeV. *Depending on the trigger configuration used, the BCAL EMC threshold was either* 1 *or* 2.5 GeV, *with no discernible effect on the acceptance of the PTE.*
In (9-6) of the PTE, the RCAL lowEMC threshold renders the RCAL EMC threshold redundant.

[%]	RCAL			BCAL		FCAL	
E_{FCAL} [GeV]	< 1	≥ 1	All	≥ 1	All	≥ 1	All
lowEMC	82 (69)	93 (69)	91 (69)	-	-	-	-
EMC	20 (18)	39 (29)	36 (28)	4.6 (0.5)	3.9 (0.4)	0.12 (0.04)	0.09 (0.04)
HAC	31 (19)	24 (6)	25 (8)	4.6 (0.7)	3.9 (0.4)	0.00 (0.00)	0.00 (0.00)
All	100 (100)	99 (91)	99 (92)	8.8 (1.3)	7.5 (0.9)	0.12 (0.03)	0.10 (0.02)

Table 9-2 Effectiveness of each CFLT trigger region in F1992.

For the photoproduction sample, the fraction of events, in %, which triggered in a given type of region is shown for the diffractive- and for the nondiffractive-like events.
For each pair of numbers, the first entry is the inclusive fraction of events, while the second entry, in brackets, is the fraction of events which triggered exclusively in the region.
Events which triggered in the RCAL EMC region, obviously also trigger the RCAL lowEMC region. Therefore, the exclusive fractions given for the RCAL EMC region ignore the lowEMC region and vice versa.

strongly depends on the z-vertex distribution (see Section 11.2.1) and on the properties of certain event types, for example the ρ production of Section 9.1.3.

Inefficiencies in the LUMIE FLT of (9-6) are identified in Section 10.6.1 by making use of events due to the GFLT trigger

$$\mathrm{CFLT}_{\mathrm{EMC}} \cdot \overline{\text{C5-background}} \tag{9-7}$$

where $\mathrm{CFLT}_{\mathrm{EMC}}$ corresponds to the EMC trigger regions, excluding RCAL lowEMC. The events due to (9-7) are among the selected events because the FLT trigger decision was not examined in the SLT, TLT or event selection. Other than the events of (9-7), which are explained in Section 10.6.1, none of the selected events were due to GFLT triggers other than that of (9-6).

The global CFLT efficiency and performance was monitored during F1992 by examining events triggered by other components. Detailed efficiency studies for the individual trigger regions examined the CFLT decision for each individual region. Technical limitations did not allow the PTE to independently collect the events required to examine the global CFLT efficiency. The GFLT did include the trigger

$$\mathrm{ADC}_{\mathrm{LUMIE}} > 40 \text{ prescaled by } 16384, \tag{9-8}$$

but the events collected are dominated by bremsstrahlung, which places no energy in CAL.

9.3 The Second and Third Level Trigger

The SLT and TLT provided very conservative removal of events due to calorimeter PMT sparks or due to p-background. As shown below, the algorithms are very cautious, ensuring that no ep events were misidentified and rejected as background. The TLT made no cuts, other than those discussed below, while the SLT had two additional cuts which were restricted to specific other GFLT trigger types and are hence ignored here.

9.3.1 Rejection of p-background by Calorimeter Timing

The TLT examined each event using the following quantities. For the 24 FCAL (8 RCAL) towers closest to the beam pipe, N_{FCAL} (N_{RCAL}) is the number of PMTs observing more than 1 GeV of energy. The average time observed in the N_{FCAL} (N_{RCAL}) PMTs is t_{FCAL} (t_{RCAL}). The event was identified and rejected as p-background if

$$N_{\mathrm{FCAL}} \geq 2 \text{ and } N_{\mathrm{RCAL}} \geq 2$$
$$\text{and } |t_{\mathrm{FCAL}} - t_{\mathrm{RCAL}} - 10.5| \leq 4.5 \text{ ns and } |t_{\mathrm{RCAL}} + 10.5| \leq 4.5 \text{ ns}. \tag{9-9}$$

A very similar algorithm was also applied by the SLT, but with a more conservative timing requirement:

$$|t_{\mathrm{FCAL}} - t_{\mathrm{RCAL}} - 14| \leq 6 \text{ ns and } |t_{\mathrm{RCAL}} + 14| \leq 6 \text{ ns}. \tag{9-10}$$

9.3.2 Rejection of CAL PMT Sparks

The search for sparks at the TLT was restricted to events with only a single spark candidate and where only a single CFLT trigger region, R_{CFLT}, had a trigger tower above threshold. Spark candidates are cells having $E_+ + E_- > 1.5$ GeV, but with a large energy imbalance observed between the two PMTs (+ and -) reading out the cell, $|E_+ - E_-|/|E_+ + E_-| > 0.9$. The event was identified and rejected as a spark if the spark candidate was in R_{CFLT} and if $|E\mathrm{TOT} - (E_+ + E_-)| \leq 2$ GeV.

9.4 The Event Selection

The selected events satisfied the following three requirements.

9.4.1 Signature of Tagged Photoproduction

Tagged photoproduction events are selected by requiring

$$E_{LUMIE} > 3 \text{ GeV in coincidence with } E_{RCAL} > 0.7 \text{ GeV}. \quad (9\text{-}11)$$

Thanks to this simple criterion, the selected events include those events required to create a clean and well understood photoproduction sample (see Chapter 10) and to examine radiative events (see Chapters 10 and 12). In Table 9-3, the requirement (9-11) is compared to the original event selection. The loose selection of (9-11) was possible, since the background events make up a only small fraction, $\lesssim 10\ \%$, of the selected events.

	Summer 1992 and run ≤ 4225 of F1992		run ≥ 4226 of F1992	
Quantity (GeV)	Minimum	Maximum	Minimum	Maximum
E_{LUMIE}	5.0	23	3	-
E_{LUMIG}	-1.0	23	-	-
E_{RCAL}	1.1	-	0.7	-
$E_{LUMIE} + E_{RCAL}$	5.0	32	-	-
$E_{LUMIE} + E_{LUMIG}$	5.0	23	-	-

Table 9-3 Summary of the event selection thresholds.

The event selection thresholds were changed once during the course of F1992.

9.4.2 The Timing Cut

Thanks to the RCAL energy requirement of (9-11), the time of the RCAL energy deposit can be used to strongly suppress the accidental p-background. Unlike the conservative on-line cut of (9-9) and (9-10) which rejected events with p-background timing, the event selection accepted only events with calorimeter timing consistent with an ep collision.

The FCAL time of an event is a weighted average of the times seen in the individual PMTs (t_i), that is

$$t_{FCAL} = \frac{\sum_{i}^{\text{FCAL PMTs}} t_i w(E_i)}{\sum_{i}^{\text{FCAL PMTs}} w(E_i)} \text{ with } w(E_i) = \begin{cases} 0 \text{ if } E_i < 0.15 \text{ GeV} \\ E_i \text{ if } 0.15 < E_i < 2.0 \text{ GeV} \\ 2 \text{ if } E_i > 2.0 \text{ GeV} \end{cases}. \quad (9\text{-}12)$$

The weight ($w(E_i)$), depends on the energy observed by the PMT, in order to correspond roughly to the rms error of the time measurement. The RCAL time is calculated by an identical procedure. The time is undefined if none of the PMTs observe more than 0.15 GeV of energy.

If the RCAL time is defined, the event is selected only if

$$|t_{RCAL}| < 6.4 \text{ ns}. \quad (9\text{-}13)$$

If the FCAL and RCAL times are defined, the event is only selected if

$$|t_{FCAL} - t_{RCAL}| < 6.4 \text{ ns}. \quad (9\text{-}14)$$

9.4.3 Rejection of Cosmic and Halo Muons

Muons are approximately minimum ionizing particles, depositing energy only in the CAL cells which they travel through. In contrast to electromagnetic and hadronic particles, muons generally pass through CAL and do not shower. Therefore, events due to cosmic or halo muons are recognized as a narrow string of calorimeter cells observing energy deposited along a straight line.

If most of the energy observed by CAL for an event is contained in a string of cells, and if the projected path does not pass near the IP, the event was considered to be a cosmic muon and was not selected. The implementation was quite conservative, ensuring that no ep events were mistakenly rejected as cosmic muons. A large sample of events rejected by the algorithm were scanned by physicists in order to verify that no ep events were rejected.

9.5 Comparison of the Summer 1992 and F1992 Trigger and Event Selection

For the events used to determine $\sigma_{tot}^{\gamma p}$, the only significant difference in the PTE of the summer 1992 measurement [1] and that of F1992, as presented in this thesis, is the set of CFLT trigger thresholds used. The tagged photoproduction trigger of summer 1992 used the thresholds shown in Table 9-4. In comparison to those of F1992 (see Table 9-1), the low FCAL thresholds of summer 1992 were possible because the tagged photoproduction trigger was restricted to a few dedicated runs where all triggered events were required to coincide with energy in LUMIE. The

[GeV]	RCAL		BCAL	FCAL	
	Beam Pipe	Other	All	Beam Pipe	Other
EMC	2.5	2.5	1	10	5
HAC	10	5	1	10	5

Table 9-4 Summer 1992 photoproduction CFLT trigger tower thresholds in each region.
All trigger towers within a given region had identical thresholds, given above in GeV.

introduction of the second independent RCAL EMC thresholds (see Section 7.1.4) allowed the F1992 tagged photoproduction trigger to join the other physics triggers and thus do away with the need for dedicated runs. The analysis of the summer 1992 data showed that the RCAL thresholds could be lowered to those of F1992 without significantly increasing the rate of background events and that the thresholds could be such that most of the events are triggered away from the beampipe.

The effectiveness of each type of CFLT trigger region in summer 1992 is shown in Table 9-5. For the F1992 data of this thesis, RCAL, with its relatively low thresholds, provided almost all of the events (see Table 9-2). In summer 1992, FCAL, with its relatively low thresholds, provided for approximately half of the event sample. Therefore, the trigger for the final hadronic system differs considerably between this measurement and the previous ZEUS measurement presented in [1]. In addition, the acceptance for the final hadronic system, $A_{RCAL} = 59 \pm 9$ % in summer 1992 [1], improves to $A_{RCAL} = 76 \pm 5$ % for the F1992 thresholds (see (11-7) and (11-9)).

[%]	RCAL		BCAL	FCAL	
	Beam Pipe	Other	All	Beam Pipe	Other
EMC	30 (21)	13 (7)	13 (2)	25 (4)	8 (1)
HAC	0	0	6 (1)	54 (19)	12 (2)

Table 9-5 Effectiveness of each CFLT trigger region for summer 1992 photoproduction.
For the photoproduction trigger of summer 1992, the fraction of events, in %, which triggered in a given type of region is shown.
For each pair of numbers, the first entry is the inclusive fraction of events, while the second entry, in brackets, is the fraction of events which triggered exclusively in the region.

10 The Photoproduction Event Sample

The total photoproduction cross section measurement requires a careful treatment of the number of ep events, with a given experimental signature, observed per unit integrated luminosity. The major steps involved in collecting, refining and verifying the data are presented. Other explicit validations of the data have been made. In addition, the use of the data sample, for example for the work presented in Chapters 11, has provided many consistency checks of the data.

10.1 The Fall 1992 Running Period

In the F1992 running period of HERA, from September 20 to November 8, ZEUS recorded runs 4064 to 4678. Of these runs, 313 occurred while HERA was providing luminosity, the remainder were calibration runs and test runs. On-line, 187 runs were declared to be **ep runs**, with no major problems known for the HERA beams or for the ZEUS detector, trigger or readout. A rough perspective on the data collection effort is given in Table 10-1. In 1 million seconds of running time, ZEUS archived 4.2 million events for 30 nb^{-1} of integrated luminosity delivered by HERA.

		For the 187 ep runs		
	Total	Average	Minimum	Maximum
Duration (seconds)	1.0×10^6	5581	553	28023
Integrated Luminosity, L_{int} (μb^{-1})	3.0×10^4	158	1	1117
Archived Events, $N_{archived}$	4.2×10^6	22539	293	138951
$N_{archived}/L_{int}$ (μb)	143	198	53	878
Selected Events, $N_{selected}$	44112	236	0	1661
$N_{selected}/L_{int}$ (μb)	1.49	1.70	0	24

Table 10-1 ZEUS ep runs for F1992.

10.2 The Selected Runs

Of the 187 ep runs, only 88 runs met the off-line requirements, summarized in Table 10-2, for the total cross section measurement. The integrated luminosity for these 88 selected runs is $L_{int} = 13.36 \pm 0.57$ nb^{-1}. Subtraction of the luminosity due to the satellite electron bunches (see Section 8.3) yields

$$L_{int} = 12.66 \pm 0.54 \text{ nb}^{-1}. \qquad (10\text{-}1)$$

Requirement	Runs Excluded	L_{int} (%) Excluded
i) Proper operation of ZEUS including CAL, LUMI, CTD, COIL	24 runs for run > 4145	15
ii) Stable proton beam as determined by C5 (see Section 8.1 and [55])	run = 4595 or 4596	1
iii) Minimal event losses and/or corruption (the final 3/4 of the events of run 4287 are missing)	run = 4287	1
iv) RCAL lowEMC threshold (see Section 7.1.4)	run < 4145	7
v) Event selection without restrictions on E_{LUMIG} or E_{LUMIE} (see Table 9-3)	run < 4226	24
vi) E_{LUMIG} and E_{LUMIE} bremsstrahlung spectrum (see Section 8.4)	run < 4272	38

Table 10-2 Requirements on runs for the total cross section measurement.

Each requirement excludes the runs shown (or the number of runs for i)), and the corresponding fraction of the 30 nb^{-1} *of integrated luminosity in the 187 ep runs. The integrated luminosity lost to the analysis due to the requirements iv) through vi) should not be summed, since the requirements reject an overlapping range of runs. Requirement i) has negligible overlap with vi).*

10.3 Event Losses and Corruption

The 4.2 million events recorded by ZEUS required a large data management effort in order to be archived, reconstructed and selected for the analysis. The number of events lost or corrupted is determined by the difference in the counts of events, given in Table 10-3, between the various stages of processing.

Symbol	Type of Events Counted	see Section
$N_{archived}$	triggered and recorded by ZEUS	6.2.5
N_{ZEPHYR}	processed by ZEPHYR	6.3
$N_{selected}$	selected events	6.3
$N_{analysis}$	in the analysis	6.4

Table 10-3 Event counts.

The events lost during processing by ZEPHYR introduced the inefficiency

$$(N_{ZEPHYR} - N_{archived}) / N_{archived} = -0.3\ \%. \qquad (10\text{-}2)$$

The selected events are managed with an inefficiency

$$(N_{analysis} - N_{selected}) / N_{selected} = -0.7\ \%. \qquad (10\text{-}3)$$

An additional inefficiency of −0.1 % is due to selected events which have at least part of their data corrupted and are thus excluded from the analysis. Combining the three inefficiencies results in a reconstruction inefficiency of

$$\Delta_{reconstruction} = -1.1 \pm 0.1\ \%. \qquad (10\text{-}4)$$

10.4 Producing a Photoproduction Sample from the Selected Events

In the analysis, each selected event is assigned to one of seven samples:

- tagged photoproduction candidates.
- accidental coincidence tagged (a.c.-tagged) photoproduction events.
- unsuitable events.
- e-pilot events.
- recognized accidental coincidence background (a.c.-background) events.
- C5- and VW-background events.
- events due to the electron satellite bunch.

The individual samples are described in greater detail below. The photoproduction candidates include all events that do not belong to one of the other six samples.

The tagged photoproduction candidates (also simply called candidates from hereon), explicitly exclude the above identified background events and, as described below, are refined into a **photoproduction sample** by the statistical removal of the remaining background events. The corrections to the photoproduction sample due to the a.c.-tagged events are described.

10.4.1 Unsuitable Events

Events recorded past the last luminosity environmental record are excluded from the candidates, as required by the luminosity determination described in Section 8.3.

The candidates were re-examined, with improved algorithms, to reject events from background processes already suppressed by the trigger and event selection. 18 additional cosmic events were removed using the algorithm presented in [76]. No sparks were found.

The events due to cosmic muons or sparks are a.c.-backgrounds. The energy observed in LUMIE is due to a coinciding bremsstrahlung event. Therefore, if any additional events due to these backgrounds have not been explicitly identified and excluded from the candidates, the events will be statistically removed, as for all a.c.-backgrounds among the candidates, by the technique presented in Section 10.4.3.

10.4.2Statistical Subtraction of the e-background

Photoproduction is the dominant process in both ep and e-background interactions producing activity in the central ZEUS detector. It is therefore difficult to distinguish ep from e-background on an event by event basis. The out-going particles of e-background are Lorentz boosted in the direction of the electron beam, and are thus especially similar to diffractive ep events whose products are similarly boosted. The e-background contamination of the nondiffractive-like sample is small (see Table 10-4). For events with $E_{FCAL} > 1$ GeV, t_{FCAL} is calculable and most e-background is rejected by the timing cut of (9-14). For the above two reasons, the treatment of the e-background is presented here with respect to the diffractive-like sample. The treatment of the nondiffractive-like sample is identical.

A sample of ep interactions can be distinguished from a sample of e-background by some distributions of the measured event characteristics such as z-vertex$_{CTD}$. While ep interactions occur only in the beam crossing region, e-background occurs along the beamline with a z-vertex distribution determined by the z dependent acceptance of the event in ZEUS and of the scattered electron in LUMIE. Unfortunately, differences in the z-vertex$_{CTD}$, CAL or other distributions cannot cleanly identify and exclude all the individual e-background events from the ep photoproduction candidates.

The magnitude of e-background was approximately estimated before data taking, ensuring that it would not be the limiting factor in the measurement. It is very difficult to obtain an accurate estimate due to several requirements, including a reliable measurement of the z dependent partial pressures of the residual gases in the beam pipe and the determination of the z dependent acceptance of the scattered electron in LUMIE. Fortunately, the details of e-background can be ignored. The events can be statistically removed from the candidates using the prescription of Section 5.5. An elaboration of the technique and its application to the candidates follows.

The e-pilot bunch, with no crossing proton beam, produces only e-background events which were collected in exactly the same manner as the events of the colliding beams. The e-background of a given bunch crossing depends on the characteristics of that crossing, including:

- the electron bunch current.
- the longitudinal and lateral distribution of the electrons in the bunch.
- the properties of the gas in the beam pipe.
- the effect the crossing proton bunch on the gas and on the electron bunch.

The number of e-background events in a given bunch crossing is assumed to be proportional to the electron current. All other differences between bunch crossings, including those mentioned above,

have a $\lesssim 1\ \%$ effect on the e-background and are safely neglected, thanks to the large statistical error for the subtraction of e-background from the candidates (see Table 10-4).

For each run, the number of e-background events among the candidates of the colliding bunches can be determined by scaling the e-pilot events by the ratio of electron currents in the nine colliding bunches and the e-pilot bunch. Determining the number of e-background events in each ep crossing does not identify the individual events in order for them to be removed from the candidates. The e-pilot events are an unbiased representation of the e-background events in the ep crossings. Therefore, for each run, the e-background is statistically subtracted by combining the candidates and the e-pilot events. Each event in the combined sample is weighted by w_e, with:

photoproduction candidate: $$w_e = +1, \qquad (10\text{-}5)$$

e-background event from e-pilot bunch: $$w_e = -\sum_{bcn=0,8} \frac{I_e^{bcn}}{I_e^{e\text{-}pilot}}. \qquad (10\text{-}6)$$

The resulting sample is effectively free of e-background. For any distribution created from the sample, each event is entered into the distribution with its weight. The negative weight assigned to the events of the e-background sample effectively 'cancels' the e-background hidden among the photoproduction candidates.

The success of the statistical subtraction of e-background is demonstrated in Figure 10-1, where the diffractive-like sample is shown to have the correct z-vertex distribution once the e-background has been removed.

The precision of the subtraction is limited by the small number of events in the e-pilot sample. The accuracy is dominated by the values for the electron currents which are estimated to have an error of 2 to 3%. Although no direct crosscheck of the currents could be made, within the limited event statistics, a consistent e-background subtraction is obtained.

10.4.3Statistical Subtraction of the Accidental Coincidence Background

The tagged photoproduction candidates require a coincidence of activity in CAL and LUMIE. Many background processes, including untagged ep, p-background, cosmic muons and halo muons can satisfy the CAL trigger and event selection requirements, but do not place any energy into LUMIE. These events can only be mistaken for tagged photoproduction if they coincide with LUMIE energy due a bremsstrahlung event. The cosmic muons, halo muons, and p-background events are identified and excluded from the candidates to the greatest extent possible, using the event characteristics measured in the central ZEUS detector, but those that remain along with the untagged ep events are difficult to identify on an event-by-event basis as (accidental coincidence) a.c.-background among the photoproduction candidates.

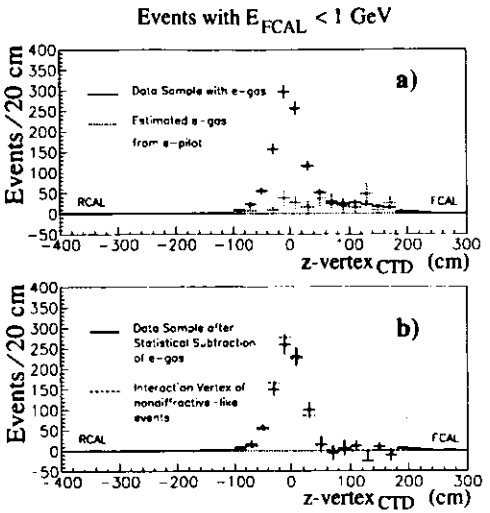

Figure 10-1 The z-vertex distribution of diffractive-like events.

a) *For the diffractive-like photoproduction candidates, the reconstructed z-vertex distribution has a long tail of events towards FCAL, due to e-background.*

b) *Following statistical subtraction, the tail is consistent with zero, and the distribution agrees well with the well-measured vertex of the nondiffractive-like sample (see Section 11.2).*

A bremsstrahlung event may have only the electron accepted in LUMIE or it may also have the radiated photon accepted in LUMIG. These two categories are respectively called e-accepted and eγ-accepted and are shown in Figure 10-2. For eγ-accepted bremsstrahlung, the electron beam energy is observed in the luminosity monitor (see Section 8.2.2), that is

$$E_{LUMIE} + E_{LUMIG} \approx E_e = 26.7\ \text{GeV}. \qquad (10\text{-}7)$$

The division of the events into e- and eγ-accepted for this analysis is shown in Figure 10-3.

For the tagged photoproduction events of this measurement, (10-7) is not true. Therefore, the so-called **recognized a.c.-background** (see Figure 10-4.), where the coinciding bremsstrahlung event is eγ-accepted, is excluded from the candidates. The remaining a.c.-background, where the coinciding bremsstrahlung event is e-accepted, cannot be distinguished from tagged photoproduction. This so-called **hidden a.c.-background** is removed from the photoproduction sample by the statistical subtraction discussed below. The recognized a.c.-tagged events of Figure 10-4 are discussed in Section 10.4.4.

The bremsstrahlung spectrum contains the statistical relationship between the eγ-accepted and the e-accepted events. From the definition of the a.c.-background, the identical statistical rela-

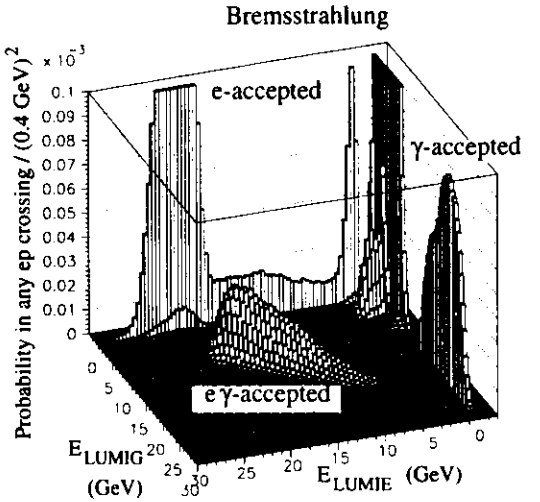

Figure 10-2 The LUMIG versus LUMIE energy spectrum for bremsstrahlung.

Shown is the weighted average, using the integrated luminosity of each run, of the absolute E_{LUMIG} *versus* E_{LUMIE} *spectra for the 88 selected runs of this analysis (see Section 10.2). Bremsstrahlung events may have the scattered electron and/or radiated photon accepted in LUMIE and LUMIG, respectively, as shown by the e-, γ- and eγ-accepted labels.*

The energetic deposits, E_{LUMIE} *or* $E_{LUMIG} \gtrsim 3$ GeV, *are due to both ep and e-background bremsstrahlung, sometimes involve more than one bremsstrahlung event per crossing, and depend on the LUMIE and LUMIG acceptances. The details of the less energetic deposits are due to a combination of bremsstrahlung, detector effects, and perhaps electrons and photons scattering on beam components before entering LUMIE and LUMIG, respectively. Electron-proton interactions other than bremsstrahlung are an insignificant part of the LUMI spectrum.*

The relative distribution among the bins near the origin is not correct since the spectrum was measured using a trigger threshold of $E_{LUMIE} \gtrsim 2$ GeV *OR* $E_{LUMIG} \gtrsim 2$ GeV.

The absolute distribution is recovered using the corresponding number of beam crossings (see Section 10.4.4.2).

tionship holds between the recognized and hidden a.c.-background, respectively. In addition, the nature of the coinciding processes in the central ZEUS detector can make no distinction between the recognized and hidden a.c.-background. In other words, the recognized a.c.-background, via the bremsstrahlung spectrum, provides the amount of hidden a.c.-background and the recognized a.c.-background is an unbiased representation of the hidden a.c.-background. Therefore, on a run-by-run basis, the hidden a.c.-background can be statistically subtracted from the photoproduction candidates by combining the candidates and the recognized a.c.-background.

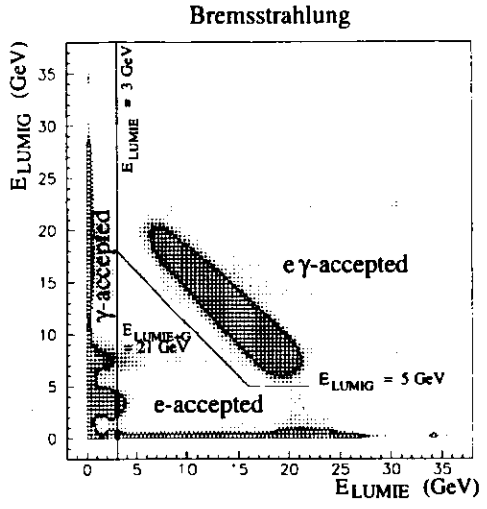

Figure 10-3 Criteria for bremsstrahlung accepted in LUMIE and/or LUMIG.
'Top-view' of Figure 10-2 shows the location of the boundary separating bremsstrahlung events according to whether the scattered electron and/or radiated photon was accepted in LUMIE and LUMIG, respectively.
The γ-accepted events are not a source of a.c.-background since they have $E_{LUMIE} < 3$ GeV *and are therefore not part of the selected sample of events (see (9-11)).*

Each event in the combined sample is weighted by w_a with:

photoproduction candidate: $$w_a = +1\,, \qquad (10\text{-}8)$$

recognized accidental coincidence: $$w_a = -N^{\text{selected events}}_{e\gamma\text{-accepted}} \times \frac{N^{\text{bremsstrahlung}}_{\text{e-accepted}}}{N^{\text{bremsstrahlung}}_{e\gamma\text{-accepted}}}\,, \qquad (10\text{-}9)$$

where $N^{\text{selected events}}_{e\gamma\text{-accepted}}$ is the number of recognized a.c.-background events (see Figure 10-4). The number of eγ- and e-accepted bremsstrahlung events is given by $N^{\text{bremsstrahlung}}_{e\gamma\text{-accepted}}$ and $N^{\text{bremsstrahlung}}_{\text{e-accepted}}$, respectively. For the statistical subtraction, the exact location of the boundary separating eγ- and e-accepted events is not important, although a reasonable subtraction requires a reasonable boundary. The boundary for this analysis allows the fraction of radiative photoproduction events to be determined (see Section 10.4.4.2). In addition to recognized a.c.-background events, $N^{\text{selected events}}_{e\gamma\text{-accepted}}$ includes a negligible number of a.c.-tagged photoproduction events (see Section 10.4.4) and radiative photoproduction events (see Chapter 12).

The recognized a.c.-background is used to subtract hidden a.c.background, which by definition has a different E_{LUMIG} versus E_{LUMIE} distribution. Therefore, in the combined sample,

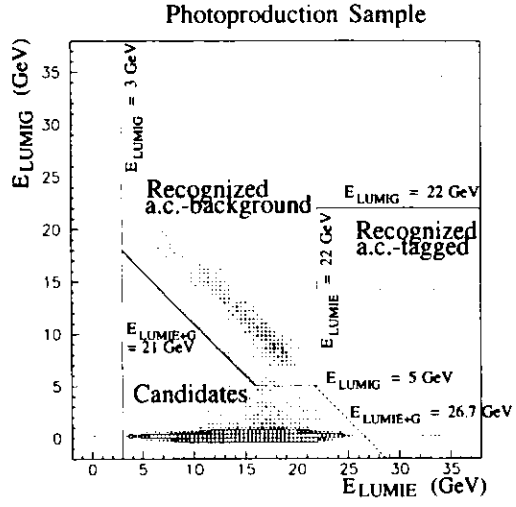

Figure 10-4 Accidentals among the selected photoproduction events.
The solid line separates the photoproduction candidates from the recognized a.c.-background. The dashed line separates the candidates from the recognized a.c.-tagged photoproduction events.

each recognized a.c.-background event has its E_{LUMIG} and E_{LUMIE} randomly reassigned according to the distribution of e-accepted bremsstrahlung. Any distribution, including E_{LUMIG} and E_{LUMIE}, for the resulting photoproduction sample is thus effectively free of hidden a.c.-background.

The success of statistical subtraction is demonstrated using the sample of C5- and VW-background events, a subset of the a.c.-background. As required, applying the above statistical subtraction to this subset results in no events remaining as shown in Figure 10-5.

The precision of the subtraction of accidentals is limited by statistics. The background events have a very large range of behavior within the central detector. Hence in the tails of some distributions, there is the small problem that bin-by-bin, the hidden a.c.-background may not be 'cancelled' exactly by the recognized a.c.-background.

10.4.4 Corrections due to the Accidental Coincidence Tagged Events

The a.c.-tagged photoproduction events are otherwise valid photoproduction events which happen to accidentally coincide with a bremsstrahlung event, leading to the two effects addressed below.

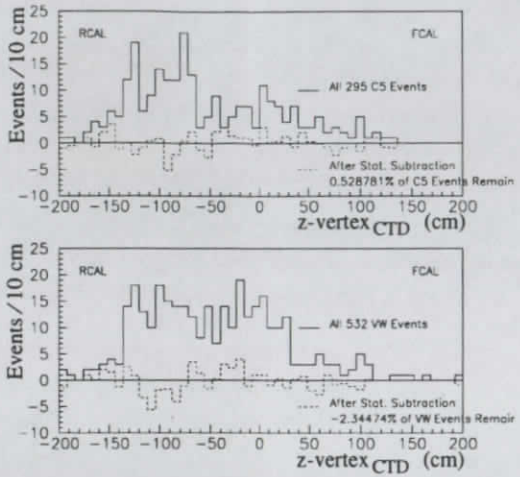

Figure 10-5 Treating C5- and VW-background as a.c.-background.
If the statistical subtraction of a.c.-background is applied to the events of the C5- and VW-background, a subset of the a.c.-background among the selected events, within statistics, all the events are removed as expected.
The z-vertex distribution demonstrates that statistical subtraction effectively removes the a.c.-background without introducing biases.

10.4.4.1a.c.-tagged events lost from the photoproduction sample

The recognized a.c.-tagged photoproduction events, seen in Figure 10-4, are lost to the photoproduction sample. They are recognized since the energy observed in the luminosity monitor exceeds the electron beam energy and can only be due to a coincidence of events, the most likely being a tagged photoproduction event and a bremsstrahlung event.

The E_{LUMIE} distributions of both tagged photoproduction (see Figure 8-5) and of bremsstrahlung (see Figure 8-6 a)) peak toward high energies. Therefore, a coincidence of tagged photoproduction with eγ- or e-accepted bremsstrahlung usually produces a recognized a.c.-tagged event, instead of migrating the event within the photoproduction sample. If the coincidence is assumed to always produce a recognized a.c.-tagged event, the data of Figure 8-6 a) predict 0.8 % as many recognized a.c.-tagged event as there are photoproduction candidates. In Figure 10-4, 0.9 % is observed. Similarly, 0.3 % as many recognized a.c.-tagged events with $E_{LUMIG} < 1$ GeV are expected and observed. This corroborates the reconstructed bremsstrahlung spectrum (see Section 10.4.4.2) and its use in this thesis. A similar result based on the E_{LUMIG} is presented in Section 12.8.

Section 10.7 presents the number of a.c.-tagged events lost from the photoproduction sample used for the total cross section measurement.

10.4.4.2a.c.-tagged events and LUMIE and LUMIG Energy Distributions

This section examines the effect of the a.c.-tagged events on the E_{LUMIG} distribution of the photoproduction sample. Although the a.c.-tagged events are a large background, the E_{LUMIG} distribution of the photoproduction sample due the radiative events can nevertheless be determined. The effect of a maximum E_{LUMIG} requirement on the photoproduction sample is also determined.

As described in the Section 10.4.4.1, E_{LUMIE} due to bremsstrahlung tends to remove the a.c.-tagged events from the photoproduction sample. Therefore, the E_{LUMIE} distribution for photoproduction is not noticeably affected by the a.c.-tagged events.

Ideally, the bremsstrahlung energy in the luminosity monitor would have been recorded for each bunch crossing. Performance limits of the luminosity monitor data acquisition system forbade this approach, instead the number of bunch crossings was counted and the bremsstrahlung events recorded satisfied

$$ADC_{LUMIG} \geq 16 \text{ OR } ADC_{LUMIE} \geq 16, \tag{10-10}$$

corresponding to

$$E_{LUMIG} \gtrsim 2 \text{ GeV} \quad \text{OR } E_{LUMIE} \gtrsim 2 \text{ GeV}. \tag{10-11}$$

In addition, some random bunch crossings, which did not have to meet (10-10) were recorded. The 'hole' in the distribution near the origin due to the trigger threshold can be seen in Figure 10-3.

In this analysis, the recorded bremsstrahlung spectrum for each run is transformed into an absolute spectrum, with one entry per bunch crossing. The ADC_{LUMIG} distribution is accurately reconstructed. Since the distribution of E_{LUMIE} is only of interest above the tagged photoproduction threshold (see (9-11)), the ADC_{LUMIE} distribution was reconstructed for $ADC_{LUMIE} \geq 16$. For simplicity, the range $ADC_{LUMIE} < 16$ is collapsed to a single entry.

The recorded ADC_{LUMIG} spectrum of ZEUS run 4499 is shown in Figure 10-6 a). The trigger threshold of 16 ADC counts is applied to the linear sum of the two PMTs of LUMIG. The spectrum used in the analysis has been smeared by corrections for pedestals and the use of the geometric mean of the ADC counts of the two PMTs (see Section 7.2.3). In addition, the distribution was technically limited to 100×100 bins for the 256×256 counts of ADC_{LUMIG} versus ADC_{LUMIE}. Again for technical reasons, a consistent set of pedestal offsets (see Section 7.2.3) could not be applied to the photoproduction sample and to the bremsstrahlung data. Therefore, the

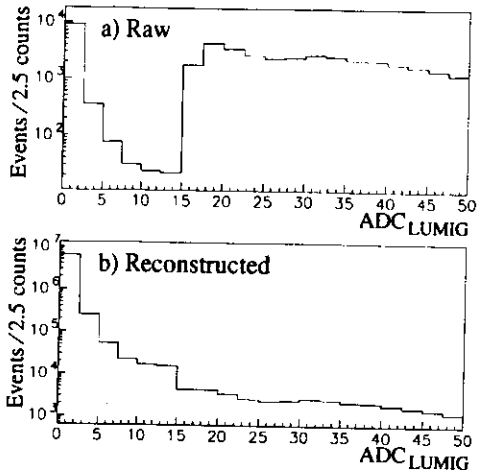

Figure 10-6 The bremsstrahlung energy spectrum in LUMIG for run 4499.
ADC_{LUMIG} *extends to 255 counts, only the region of interest is shown.*
a) *The recorded* ADC_{LUMIG} *spectrum.*
b) *The reconstructed spectrum using the bunch crossing count.*

steeply falling distribution near $E_{LUMIG} \sim 0$ may not be correct due to the migration of events across bins. From the distribution shown in Figure 10-6 a), the absolute ADC_{LUMIG} spectrum is produced by:

i) Setting the seventh bin, 15 – 17.5 ADC counts, encompassing the trigger threshold, equal to the eighth bin.

ii) Scaling the first six bins, 0 – 15 ADC counts, such that the total number of entries in the entire histogram is equal to the number of bunch crossings.

The resulting absolute distribution for run 4499 is shown in Figure 10-6 b). After converting the absolute ADC_{LUMIG} spectrum of each run to GeV, the integrated luminosity weighted reconstructed E_{LUMIG} spectrum for all the selected runs is shown in Figures 8-6, 10-2 and 10-7.

A bremsstrahlung event, as any other event, may coincide with bremsstrahlung energy in the luminosity monitor. In particular, e-accepted bremsstrahlung events, which deposit $E_{LUMIG}^{e\text{-accepted}}$ into LUMIG, will coincide with the LUMIG energy spectrum described above. The coincidence is observed with $E_{LUMIG} \geq E_{LUMIG}^{e\text{-accepted}}$. If $E_{LUMIG}^{e\text{-accepted}}$ is ignored and the entire E_{LUMIG} is attributed to the coinciding bremsstrahlung energy, an independent upper bound of the LUMIG bremsstrahlung spectrum is obtained. As seen in Figure 10-8, for $E_{LUMIG} \lesssim 4$ GeV the reconstructed spectrum agrees well with the e-accepted LUMIG spectrum. This is perhaps expected since the photon of an e-accepted bremsstrahlung event generally escapes LUMIG completely such that $E_{LUMIG}^{e\text{-accepted}} = 0$ GeV. For $E_{LUMIG} \gtrsim 4$ GeV, the e-accepted LUMIG spectrum increases due to an increasing contamination of bremsstrahlung events where both the electron and photon are accepted such that $E_{LUMIG}^{e\text{-accepted}} \neq 0$ GeV.

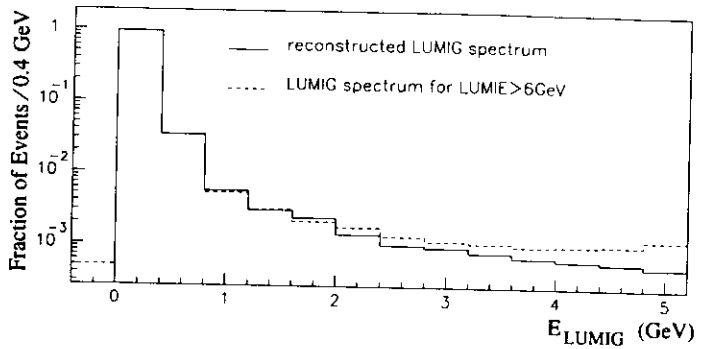

Figure 10-7 The bremsstrahlung energy spectrum in LUMIG for all selected runs.
The solid line is the weighted average, using the integrated luminosity of each run, of the reconstructed E_{LUMIG} *spectra for the 88 selected runs of this analysis (see Section 10.2).*
The dashed line is the E_{LUMIG} *distribution for e-accepted bremsstrahlung events, requiring* $E_{LUMIE} > 6$ GeV *since events at lower energies often deposit energy into LUMIG as seen in Figure 10-3 or Figure 10-4.*
See the text for the rationale of comparing the two curves.

In order to reduce the number of radiative photoproduction events in the sample, the requirement

$$E_{LUMIG} < E_{LUMIG}^{max} \tag{10-12}$$

may be imposed. Along with radiative events, (10-12) removes a.c.-tagged events. The fraction of the photoproduction sample lost as a.c.-tagged events is estimated in Figure 10-8, which shows the integrated fraction of bunch crossings with $E_{LUMIG} \geq E_{LUMIG}^{max}$ due to bremsstrahlung events. For example, requiring $E_{LUMIG} < 0.4$ GeV, in addition to removing events with a radiated photon accepted in LUMIG, would lose 6% of the photoproduction sample due to a.c.-tagged events.

The E_{LUMIG} distribution due to the radiative events among the photoproduction sample can be determined, as shown in Figure 10-9, by subtracting the fraction of the distribution due to the a.c.-tagged events, as given by the reconstructed bremsstrahlung E_{LUMIG} spectrum.

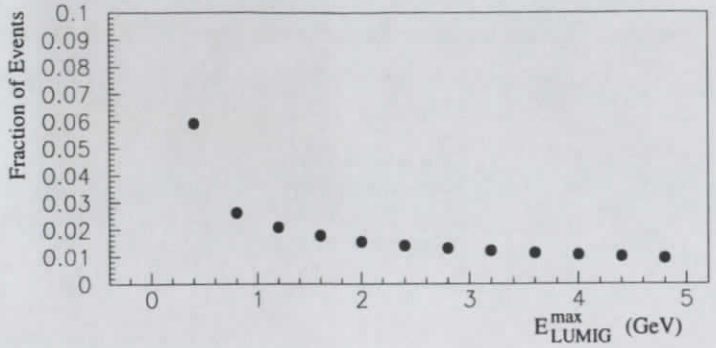

Figure 10-8 Fraction of events lost due to a LUMIG energy requirement.
Imposing a maximum energy requirement for the LUMIG loses a.c.-tagged events shown as a fraction of the events of photoproduction sample.

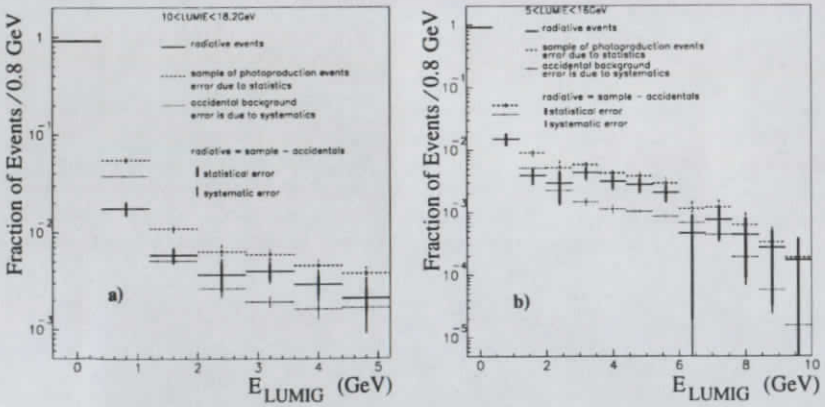

Figure 10-9 The LUMIG energy distribution for photoproduction events.
After correcting for the a.c.-tagged events, the E_{LUMIG} *distribution of the photoproduction sample is due to the photons of radiative events accepted in LUMIG. Due to the cut required to remove the recognized a.c.-background (see Figure 10-4), the distribution is shown for two ranges of* E_{LUMIE}*:*
a) *The range* $10 < E_{LUMIE} < 18.2$ GeV *has good statistics, but is limited to* $E_{LUMIG} < 5$ GeV.
b) *The range* $5 < E_{LUMIE} < 16$ GeV *allows for* $E_{LUMIG} < 10$ GeV *within the constraint of* $E_{LUMIE} + E_{LUMIG} < 21$ GeV *(see Figure 10-4).*

10.5 Excluding the Events due to the Satellite Electron Bunch

The events due to the satellite electron bunch (see Section 5.7) are excluded from the photoproduction sample as is their contribution to the luminosity measurement (see Section 8.3). The satellite electron bunch crosses the proton bunch at $z = 8$ ns $\cdot c/2 = 120$ cm. The resulting satellite events need to be excluded from the measurement because their characteristics and acceptance in the central ZEUS detector differ significantly from those of the nominal ep interactions at $z = 0$ cm.

Particles of the satellite events reach RCAL at $t_{RCAL} \sim 8$ ns. Therefore, due to the RCAL timing cut in (9-13), only a fraction of the satellite events are among the selected events. The remaining satellite events can be excluded from the photoproduction sample because they satisfy

$$t_{RCAL} > 3.5 \text{ ns AND z-vertex}_{CTD} > 50 \text{ cm} \qquad (10\text{-}13)$$

OR

$$t_{RCAL} > 5.0 \text{ ns AND z-vertex}_{CTD} \text{ could not be reconstructed.} \qquad (10\text{-}14)$$

The justification for (10-13) is shown in Figure 10-10, where the combined timing and z-vertex requirement separates the events due to the primary and satellite electron bunch. Of the events rejected by (10-14), 74 % have $E_{FCAL} < 1$ GeV. Compared to the nominal 24 % (see Table 10-4), it suggests that these events are indeed satellite events for which the FCAL beampipe has a large opening angle.

The resulting t_{RCAL} distribution for the photoproduction sample, shown in Figure 10-11, suggests that the satellite events have been successfully excluded.

10.6 Trigger and Event Selection Inefficiencies

All tagged photoproduction events satisfying the LUMIE and CAL criteria of the trigger and event selection (see Chapter 9) are expected to be among the selected events. Events may be lost due to inefficiencies of the trigger or of the event selection.

Neither the SLT, TLT nor their algorithms lost tagged photoproduction events. The only trigger inefficiency is that of the LUMIE FLT presented below.

In the event selection, the rejection of cosmic and halo muons did not mistakenly reject any tagged photoproduction events. However, as shown below, the timing requirement did.

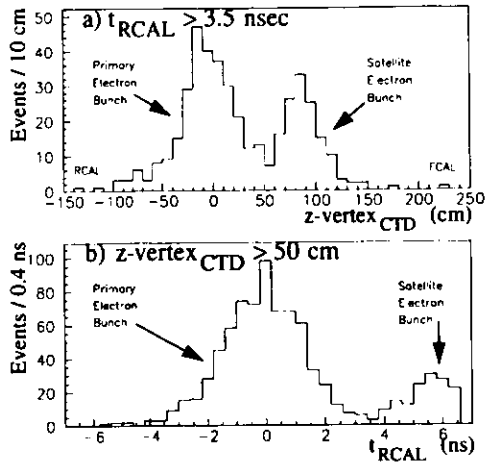

Figure 10-10 Recognizing events due to the satellite electron bunch.
The combined RCAL timing and z-vertex requirement of (10-13) provides a relatively clean separation of the events due to the primary and satellite electron bunch.
The above satellite events are those that survive the RCAL timing cut in (9-13) of the event selection. Hence, the distributions of the satellite events shown above are only the tails of the full distributions which peak at t_{RCAL} ~ 8 ns *and* z-vertex$_{CTD}$ ~ 120 cm.

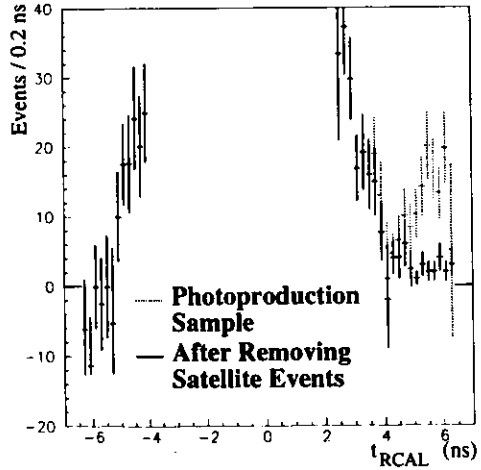

Figure 10-11 The RCAL timing distribution for the photoproduction sample.
Events with $-4 < t_{RCAL} < 2$ ns *are off-scale.*

10.6.1 Inefficiency of the LUMIE FLT

Each of the selected runs 4296, 4407, 4409, 4452 and 4453 had a temporary period of communication troubles between the GFLT and the LUMIE FLT. In runs 4296 and 4452, the period was too short to have affected the trigger performance. In the other three runs, the LUMIE FLT was inactive for a significant fraction of each run. This trigger inefficiency was flagged by events in the photoproduction sample which had not satisfied (9-6) of the GFLT and instead were triggered by (9-7). Since the ratio of events triggered by (9-7) to those triggered by (9-6) is known (see Table 9-2), the size of the inefficiency can be determined. After taking the inefficiency into account, the observed tagged photoproduction cross section of the affected runs, 4407, 4409 and 4453, agrees well with the average of the other 85 runs of the photoproduction sample. In terms of the entire photoproduction sample, the effect is a trigger inefficiency of

$$\Delta_{trigger} = -0.7 \pm 0.1\ \%. \qquad (10\text{-}15)$$

10.6.2 Inefficiency of the Timing Cut in the Event Selection

The timing cut in the event selection (see Section 9.4.2) was too restrictive and some tagged photoproduction events were lost. This is demonstrated in the scatter plot of Figure 10-12, where the boundaries of the timing cut are clearly visible for both (9-13) and (9-14).

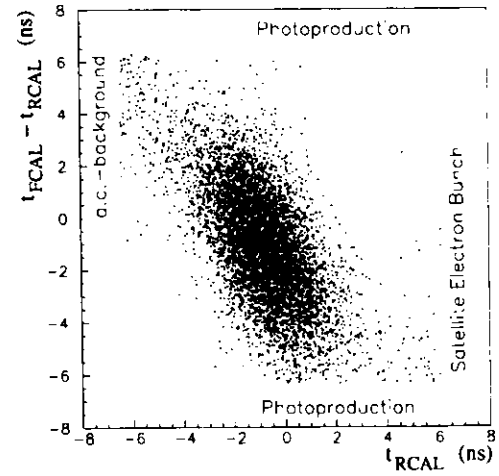

Figure 10-12 A scatter plot of the variables of the event selection timing cut.
The types of event dominantly populating the areas adjacent to the boundaries are noted.

After removing the a.c.-background and the events due to the satellite electron bunch, the tails of the t_{RCAL} distribution for the photoproduction sample, shown in Figure 10-11, are consistent with zero events. An insignificant number of events are thus expected to have been lost from the photoproduction sample by (9-13) of the event selection.

Tagged photoproduction events were lost by (9-14) of the event selection, as demonstrated in Figure 10-13, where the fraction of events lost is estimated as

$$\Delta_{selection} = -1.0 \pm 0.3\ \%. \qquad (10\text{-}16)$$

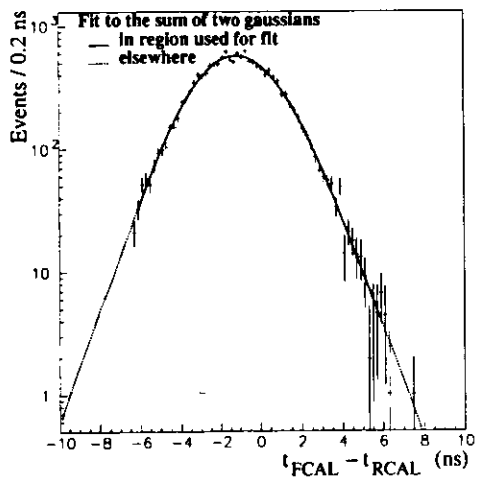

Figure 10-13 The distribution of the time difference between FCAL and RCAL.
An extrapolation of the distribution estimates that 1.0 ± 0.3 % *of the events had* $t_{FCAL} - t_{RCAL} < -6.4$ *and were lost to the photoproduction sample by (9-13).*

10.7 The Number of Photoproduction Events for the Total Cross Section Measurement

For the total cross section measurement, $N_{\text{tagged php.}}$ (see Section 1.2) is based on a subset of the photoproduction sample presented up until this point. The events in the subset have

$$15.2 < E_{LUMIE} < 18.2\ \text{GeV}, \qquad (10\text{-}17)$$

as required for the W range of the measurement. The effect of radiative photoproduction events on the exchanged photon energy (see Section 12.4) is reduced by requiring the subset to have

$$E_{LUMIG} < 1\ \text{GeV}. \qquad (10\text{-}18)$$

The number of events in the subset is presented in Table 10-4, as is the effect of the e- and a.c.-background. The subset corresponds to the integrated luminosity given in (10-1) and is accompanied by the correction factors given in (10-4), (10-15) and (10-16).

The fraction of a.c.-tagged events lost from the subset due to (10-18) is 2.6 % (see Figure 10-8). In addition, for $E_{LUMIG} < 1$ GeV, 0.3 % of the events are lost as a.c.-tagged events involving an e-accepted bremsstrahlung event (see Figure 8-6 a)). The total fraction lost is

$$\Delta_{\text{a.c.-tagged}} = -2.9 \pm 0.6\ \%. \qquad (10\text{-}19)$$

	number of events		
	$E_{FCAL} < 1$GeV	$E_{FCAL} \geq 1$GeV	all events
photoproduction candidates	1112 ± 33	4907 ± 70	6019 ± 78
e-background events	− 220 ± 48 (23)	− 19 ± 13 (2)	− 239 ± 50 (25)
a.c.-background events	− 12 ± 03 (16)	− 36 ± 05 (54)	− 48 ± 06 (70)
total	879±59	4852±72	5731±92

Table 10-4 Number of tagged photoproduction events.

The number of diffractive- and nondiffractive-like events satisfying (10-17) and (10-18) is shown. The number of e- and a.c.-background events subtracted from the photoproduction candidates is based on the number in brackets of e-pilot and recognized a.c.-background events, respectively. No correction factors have been applied. All errors shown are statistical.
Without the $E_{LUMIG} < 1$ GeV *requirement of (10-18), the total number of events is 5959, instead of 5731.*

11 The Acceptance in CAL of the Final Hadronic System

The acceptance (A_{RCAL}) of the CAL trigger and the RCAL energy requirement (see (9-6) and (9-11)) for the final hadronic system of tagged photoproduction is taken as the fraction of generated γp events which, following the MOZART simulation of their observation in the detector, are accepted by the ZGANA simulation of the above requirements (see Section 6.5). As described in Chapter 3, the exact behavior of the VMD, direct and anomalous γp interactions is not yet known at HERA energies, nor are their relative cross sections. Therefore, the composition of the generated events is adjusted, as are the event characteristics within the freedoms allowed by the individual processes, such that the distribution of energy deposited in CAL (from hereon called CAL distributions) for the accepted simulated events matches that of the measured events.

The results presented here focus on the determination of A_{RCAL} for the total cross section measurement. A more detailed presentation may be found in [77], which also includes the determination of the elastic diffractive, inelastic diffractive and non-diffractive inclusive cross sections.

11.1 The Data Sample

The significance of the comparison of the CAL distributions increases with the number of accepted simulated events and measured events used in the comparison. Therefore, the **data sample** used to determine A_{RCAL} includes the events with $15.2 < E_{LUMIE} < 18.2$ GeV from all runs which satisfy requirements i) through iv) of Table 10-2. Requirements v) and vi), which would otherwise exclude 38% of the data from the analysis, are ignored for the data sample. Requirements v) and vi) provide the ability to remove the approximately 1 % of the photoproduction candidates which are background events involving accidental coincidences with bremsstrahlung events (see Table 10-4). The effect of the neglected a.c.-background for the CAL distributions was confirmed to be negligible. In other respects, the data sample is treated identically to the subset of the photoproduction sample used to determine $N_{\text{tagged php.}}$ in Section 10.7, including the $E_{LUMIG} < 1$ GeV requirement of (10-18) and the statistical subtraction of the e-background (see Section 10.4.2).

11.2 Experimental Conditions for the Simulation

Due to the narrow energy range (8.5 – 11.5 GeV) of the tagged photons used in the cross section measurement, the event simulation simply uses 10 GeV incident photons.

The conditions described below are consistent for the runs of the photoproduction sample and the additional runs of the data sample. Therefore, the CAL acceptance determined in this chapter may be applied to $N_{\text{tagged php.}}$ determined in Section 10.7. Corroboration is given by the measured cross section, which is consistent for the photoproduction sample and the data sample,

though that of the data sample has a larger error due to the uncertainty introduced by the runs lacking the bremsstrahlung spectrum.

11.2.1 The z-vertex Distribution

The acceptance of diffractive γp interactions has a strong dependence on the z-vertex of the event (see Figure 11-1 a) and b)).Therefore, the z-vertex distribution of the simulated events must follow that of the data sample. Since the z dependence of the nondiffractive-like data sample is relatively flat (see Figure 11-1 c)), it was used to parametrize the z-vertex distribution used in the simulation [78]. As shown in Figure 11-2, the reconstructed z-vertex of the resulting simulated events agrees well with that of the data sample.

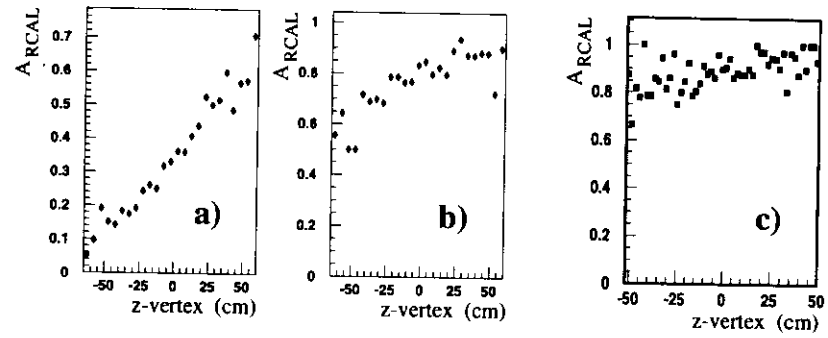

Figure 11-1 The z-vertex dependence of the acceptance in CAL.
The acceptance of the final hadronic system depends on the z-vertex of the event. The dependence is steepest for a) elastic vector meson production (see Section 11.3.1). The dependence is less pronounced for b) photon diffraction (see Section 11.3.1) and is almost flat for c) the nondiffractive events of the PYTHIA minimum bias generator (see Section 11.3.2).

The corresponding z-vertex distribution expected by C5, also shown in Figure 11-2, must be displaced by −5 cm to agree with that of the CTD (see Section 8.1.2). For the diffractive processes, the effect of shifting the z-vertex distribution by ±5 cm is included in the error of the acceptances determined in Section 11.3.1. The acceptance of nondiffractive events is affected negligibly by such a shift.

11.2.2 The Efficiency of the CFLT Trigger Towers

The CFLT trigger tower thresholds given in Table 9-1 are nominal values. Figure 11-3 shows the CFLT efficiency for the trigger towers of the RCAL EMC region, which provided the bulk of the tagged photoproduction events (see Table 9-2). The efficiency is calculated from the data sample, as permitted by the independent trigger regions. Averaged over all the trigger towers

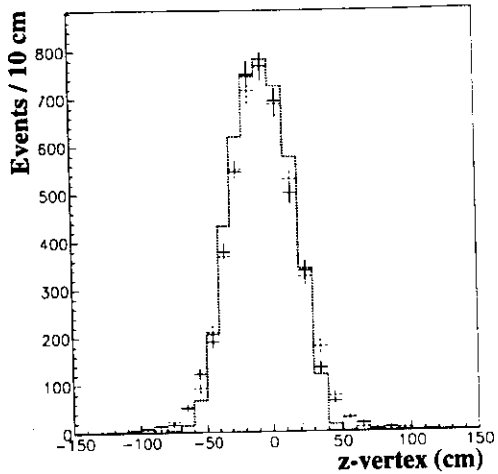

Figure 11-2 The z-vertex distribution for F1992.
The distribution of the z-vertex reconstructed by the CTD for the subset of the nondiffractive-like photoproduction sample used for the total cross section measurement (solid line, see Section 10.7) compares well with that of simulated minimum bias PYTHIA events (dashed line, see Section 11.3.2). For the corresponding selected runs (see Section 10.2), if the C5 location is taken as z = −310 cm instead of the nominal −315 cm (see Section 8.1.2), the z-vertex distribution expected by C5 (dotted line) agrees well with that determined by the CTD, which includes its measurement resolution of 2 cm *(see Section 7.5.2).*

of a region, the efficiency is not a step function at the threshold energy. It instead rises from 0 to 100 % within a range of energies observed in the individual trigger towers. The CFLT efficiency must be taken into account for the acceptance determination since a large fraction of the data sample is triggered close to the thresholds, as seen in Figure 11-4. The data sample is approximately halved if the trigger thresholds are doubled.

For technical reasons, the determination of A_{RCAL} assumes the CFLT trigger towers to be perfectly efficient and behave as step functions. A correction for the actual efficiency is applied following the determination of A_{RCAL}. The correction factor is determined in a detailed analysis of the events lost when raising the CFLT thresholds for both the data and the simulated event samples [77]. The correction factors are generally small, of order 1 %. As seen in Figure 11-4, doubling or tripling the threshold has the same effect on the data and the simulated sample, such that the measured cross section remains unchanged, even though the CFLT efficiency has been ignored.

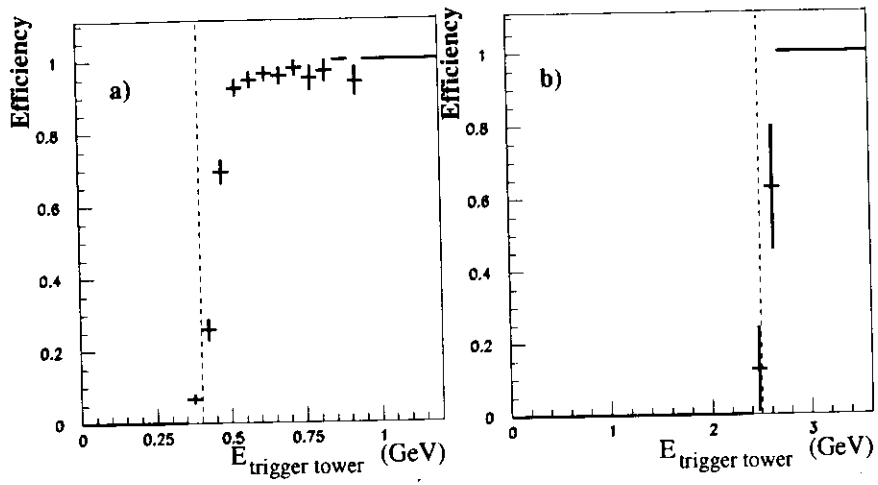

Figure 11-3 RCAL EMC trigger tower efficiencies.
Averaged over all trigger towers in the RCAL lowEMC Beam Pipe (a)) and Other (b)) regions (see Figure 7-3), the efficiency of a trigger tower with energy $E_{trigger\ tower}$ *is determined from the data sample. The dashed line shows the nominal* $E_{trigger\ tower}$ *threshold (see* Table 9-1*). Data courtesy of Danny Krakauer.*

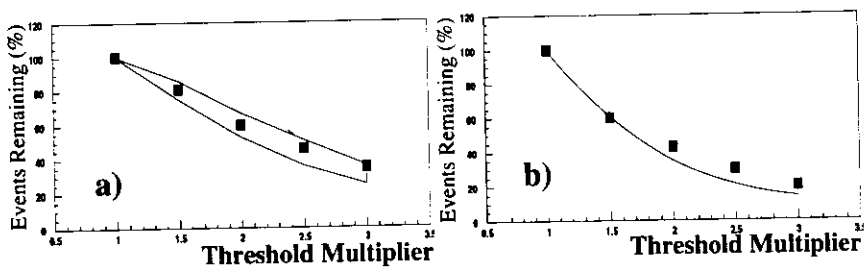

Figure 11-4 Effect on acceptance of increased CFLT trigger thresholds.
The solid squares are the fraction of events which remain, if the events are required to satisfy an increase of the original CFLT trigger tower thresholds (see Table 9-1).
The thresholds have been assumed to behave as ideal step functions.
a) *The nondiffractive-like data sample (events with* $E_{FCAL} > 1$ GeV *) behaves like the accepted simulated events of the HERWIG (upper line) and PYTHIA (lower line) minimum bias generators (see Section 11.3.2).*
b) *The diffractive-like data sample (events with* $E_{FCAL} < 1$ GeV *), behaves like the accepted simulated photon diffractive events generated by PYTHIA (see Section 11.3.1).*
Data courtesy of Maciej Krzyzanowski.

11.3 Photon-Proton Event Simulation

A variety of descriptions of γp interactions successfully lead to accepted simulated events with CAL distributions which agree with those of the data sample. The acceptance of the simulated events depends on the description of γp interactions used to generate the events. Therefore, the error on A_{RCAL} must accommodate the various successful descriptions. The following two sections respectively introduce the range of diffractive and nondiffractive processes examined, which, in combination, aim to determine A_{RCAL} for all possible successful descriptions of γp interactions.

11.3.1 Diffractive Photon-Proton Processes

The diffractive γp interactions (see Sections 3.2.1 and 3.2.2) are examined using the descriptions outlined in Table 11-1. Also given in the table is the fraction of events ($F^{FCAL<1}$) with $E_{FCAL} < 1$ GeV and the acceptance ($A^{FCAL<1}$) for those events.

diffractive process	$F^{FCAL<1}$ [%]	$A^{FCAL<1}$ [%]	generator and parameters
elastic, $\gamma^* p \to Vp$	100	31 ± 4	PYTHIA (HERWIG) relative fractions of mesons produced [4]: $\rho : \omega : \phi = 1/2.2 : 1/23.6/ : 1/18.4$ slope of t distribution: $8 \le b \le 18$ GeV^2
$\gamma^* p \to \rho p$		38	
$\gamma^* p \to \omega p$		21	
$\gamma^* p \to \phi p$		3	
inelastic			squared mass exponent: $1.0 \le a \le 1.3$ slope of t distribution: $4 \le b \le 9$ GeV^2
proton, $\gamma^* p \to VX_p$	23 – 50	37 ± 4	PYTHIA
photon, $\gamma^* p \to X_V p$	40 – 70	75	PYTHIA } see Table 11-2.
		85	Nikolaev-Zakharov }
double, $\gamma^* p \to X_V X_p$	27 – 40	82 ± 3	PYTHIA
		90 ± 5	HERWIG minimum bias (see Section 11.3.2)

Table 11-1 Characteristics of the simulated diffractive interactions.

The PYTHIA [79] event generator was used to simulate the events of the elastic processes and the results are corroborated by elastic ρ events generated by HERWIG [80].

PYTHIA was used to generate event samples for all three types of inelastic diffraction. For photon diffraction, the Nikolaev-Zakharov model [81], as implemented in [82], was also used.

Also for photon diffraction, a toy model with an isotropic decay for the diffractive system (X_V) was examined and rejected since its results cannot be accommodated by the data. Table 11-2 outlines the characteristics examined for the diffractive systems of the proton (X_p) and the vector meson (X_V).

characteristic of diffractive system	PYTHIA	Nikolaev-Zakharov
minimum mass	$M_{X_{p,\rho}} > m_{p,\rho} + 0.2$ GeV	$M_{X_V} > 1.7$ GeV
maximum mass	$M_X^2/W^2 < 0.1$ (0.05 fits the data less well)	$M_{X_V}^2/W^2 < 0.03$
decay	limited p_T string decay	model

Table 11-2 Characteristics of the outgoing diffractive system.

11.3.2 Nondiffractive Photon-Proton Processes

The generators used for the nondiffractive γp processes are taken directly from hadron-hadron physics. The HERWIG minimum bias generator, described below, creates a sample of γp events, by combining samples of $\pi^+ p$ and $\pi^- p$ events, as permitted by the additive quark model (see Section 3.2.5). The remaining generators described below are based on parton-parton interactions. Thus the structure functions, describing the distribution of partons within the interacting hadrons, are those of the photon and the proton. Table 11-3 outlines the generators used for nondiffractive γp interactions. Except for the HERWIG minimum bias generator, for reasons described below, greater than 99 % of the events from the other generators have $E_{FCAL} > 1$ GeV.

Three approaches are used to model the nondiffractive processes. In the first, an event sample of the soft component (see Section 3.2.3) is combined with an event sample from hard scattering. The soft component is generated by the PYTHIA two string model using various values for the mean transverse momentum of the resulting charged particles ($\langle p_T^{ch} \rangle$). The soft sample with $\langle p_T^{ch} \rangle = 390$ MeV fits the data sample best and is used in the remainder of the analysis. The hard component includes both the VMD (see Section 3.2.4) and anomalous photon contribution (see Section 3.3). The combination is achieved by using the DG [83] structure function for the photon, which includes both the VMD and the anomalous part (see (3-13)). Both PYTHIA and HERWIG have been used to generate event samples of the hard scattering for a reasonable range of the transverse momentum cutoff (p_T^{min}) of the original parton-parton interaction. For $p_T^{min} < 1.8$ GeV, the jet cross section approaches $\sigma_{tot}^{\gamma p}$. Although the choice of proton and photon structure functions and the value of p_T^{min} can lead to large variations for $\sigma_{tot}^{\gamma p}$, they have relatively little effect on the acceptance in CAL of the resulting final hadronic system. This can be seen for p_T^{min} in Table 11-3 and Table 11-4. For the structure functions, for example, no large differences

process	label	$A^{FCAL>1}$ [%]	generator	parameter
soft	soft	89	PYTHIA	$\langle p_T^{ch} \rangle$ = 390 MeV
		85		$\langle p_T^{ch} \rangle$ = 330 MeV
		78		$\langle p_T^{ch} \rangle$ = 270 MeV
hard	PYTHIA.1.8	90	PYTHIA	p_T^{min} = 1.8 GeV
	PYTHIA.2.0	90		p_T^{min} = 2.0 GeV
hard	HERWIG.1.5	84	HERWIG	p_T^{min} = 1.5 GeV
	HERWIG.1.7	84		p_T^{min} = 1.7 GeV
	HERWIG.2.0	84		p_T^{min} = 2.0 GeV
minimum bias	PYTHIA.min.bin	89	PYTHIA	
minimum bias	HERWIG.min.bin	95	HERWIG	

Table 11-3 Characteristics of the simulated nondiffractive interactions.

in the CAL distributions are observed if F_2^{γ} of DG is replaced by a scaled F_2^{π}, corresponding via the additive quark model to the pure VDM photon without the anomalous photon contribution.

In the second model of nondiffractive processes, the soft and hard contributions are combined in a so-called minimum bias event sample. PYTHIA generates these events using phenomenological QCD parton dynamics which include the possibility of more than one parton-parton interaction per γp interaction.

The third model, provided by HERWIG, generates minimum bias events without any dynamical ansatz and is instead based on the minimum bias $p\bar{p}$ event generator of the UA5 Collaboration [84]. For each event, the number of charged particles (n^{ch}) is taken from a negative binomial distribution (NBD). Two parameters of the NBD have been tuned such that the mean and width of the n^{ch} distribution matches that of the data sample [85]. The NBD is based on nondiffractive and double diffractive events observed by UA5. Therefore, it is not unexpected that 5 % of the HERWIG minimum bias events have $E_{FCAL} < 1$ GeV.

No direct photon component (see Section 3.4) was used in the acceptance determination. If the direct component is assumed to be responsible for 20 % of $\sigma_{tot}^{\gamma p}$, by setting the cutoff parameter $p_o = 0.5$ GeV, the resulting events have been confirmed to be similar to the low p_T events of the above three models. Therefore, even if there is a significant direct component, the acceptance of its events is correctly determined with the above models.

11.4 The Acceptance in CAL

The best description of the data sample using the simulated events is determined by minimizing the χ^2 variable where

$$\chi^2 \equiv \frac{1}{\text{bins}} \sum_{\text{bins}} \frac{(N_{\text{data}} - N_{\text{sim}})^2}{\sigma_{\text{data}}^2 + \sigma_{\text{sim}}^2}, \tag{11-1}$$

which is summed over the bins of one or more CAL distributions. N_{data} is the number of entries for the data sample in a given histogram bin of the distribution(s), with σ_{data} as the statistical error. For the simulated events the corresponding numbers are N_{sim} and σ_{sim}. The sample of accepted simulated events is normalized to have the same number of events as the data sample, that is $\sum N_{\text{data}} \equiv \sum N_{\text{sim}}$.

The χ^2 is used in this thesis as a means to compare and fit the distributions of the data sample with those of the accepted simulated events. The variety of descriptions of γp interactions, with their respective values for A_{RCAL}, which are compatible with the data sample can thus be determined. The χ^2 of the resulting fits are large, $\chi^2 = 1 - 9$. This is acceptable for this measurement, since the accepted simulated events are not expected nor required to provide an exact description of the data sample. Excellent agreement, at the level of $\chi^2 = 1$, between γp at HERA and γp of the event generators will only be achieved once ZEUS and H1 have investigated γp interactions in much greater detail and the event generators have been appropriately tuned.

11.4.1 The Diffractive-like Events

All the processes share a very similar distribution for the total RCAL energy, which thus cannot be used to identify the fractions of events in the diffractive-like data sample due to the individual diffractive processes. The radial distribution of the energy deposited in RCAL does differ between processes. Elastic scattering and proton diffraction place a vector meson into RCAL and the decay products of the vector meson are very close to the RCAL beampipe (see Section 9.1.3). From the decay of the higher mass state diffractive system, photon and double diffraction have particles which may enter RCAL well away from the beam pipe. Therefore, information on the composition of the diffractive-like data sample can be gained from the distribution of the energy weighted radius in RCAL defined as

$$R_{RCAL} \equiv \frac{\sum_{RCAL} r_{cond} E_{cond}}{\sum_{RCAL} E_{cond}}, \tag{11-2}$$

where E_{cond} is the summed energy of a condensate, an object created by combining adjacent energetic CAL cells [86]. The radial distance from the condensate to the beampipe is r_{cond}.

Within the resolution of this measurement, the R_{RCAL} distribution is the same for the elastic and the proton diffractive events. The distribution is also the same for the photon and the double diffractive events. The R_{RCAL} distribution may thus be used to determine the ratio

$$r = \frac{N_{Vp} + N_{VX}}{N_{Vp} + N_{VX} + N_{Xp} + N_{XX}}, \tag{11-3}$$

where $N_{Vp}, N_{VX}, N_{Xp}, N_{XX}$ are the number of accepted simulated elastic, proton, photon and double diffractive events, respectively. From the normalization of the simulated sample and the data samples, $N^{FCAL<1} = N_{Vp} + N_{VX} + N_{Xp} + N_{XX}$.

The R_{RCAL} distribution for the data sample and the accepted simulated events is shown in Figure 11-5. As described above, only two types of R_{RCAL} distribution exist for the diffractive events, so it is sufficient to use only a sample of elastic (Vp) and a sample of photon diffractive (Xp) events to determine r from the data.

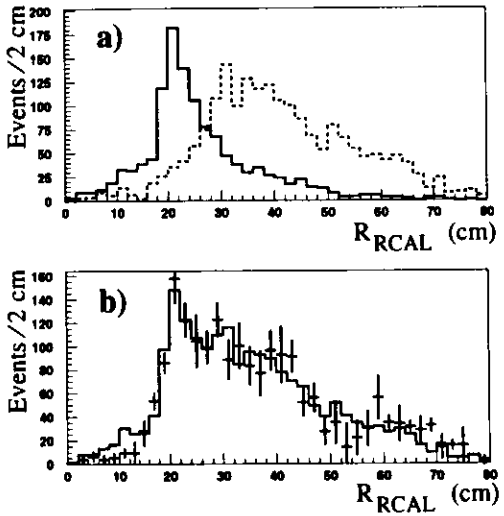

Figure 11-5 The energy weighted radius in RCAL for diffractive processes.
a) *Accepted simulated events from Vp PYTHIA (solid line) and from Xp Nikolaev-Zakharov (dashed line).*
b) *The diffractive-like sample data sample with the best fit using a mixture of Vp PYTHIA and Xp Nikolaev-Zakharov.*

Using Vp PYTHIA and Xp Nikolaev-Zakharov results in $r = 0.42 \pm 0.05$, where the error is due to the resolution of the χ^2 fit for the number of events in the data sample. Using Xp PYTHIA results in a poorer fit with $r = 0.36 \pm 0.05$. Combining the results, using the Xp PYTHIA fit as an estimate of the systematic error, provides $r = 0.42 \pm 0.05 \pm 0.06$.

The acceptance in CAL of the diffractive-like sample is defined as

$$\frac{N^{FCAL<1}}{A^{FCAL<1}} = \frac{N_{Vp}}{A_{Vp}} + \frac{N_{VX}}{A_{VX}} + \frac{N_{Xp}}{A_{Xp}} + \frac{N_{XX}}{A_{XX}}, \tag{11-4}$$

using the acceptances in CAL of the individual diffractive processes (see Table 11-1). The fit to the R_{RCAL} distribution provides $N_{Vp} + N_{VX} = 0.42N^{FCAL<1}$ and $N_{Xp} + N_{XX} = 0.58N^{FCAL<1}$. Thus, (11-4) is reduced to

$$\frac{1}{A^{FCAL<1}} = \frac{0.42}{A_V} + \frac{0.58}{A_X}, \tag{11-5}$$

where A_V lies between A_{Vp} and A_{VX}, similarly A_X lies between A_{Xp} and A_{XX}. Using the extreme values for A_V, A_X and r restricts the acceptance to $A^{FCAL<1} = 52 \pm 12\ \%$.

The analysis is taken a step further in [77] in order to determine the elastic diffractive, inelastic diffractive and non-diffractive inclusive cross sections. That analysis reasonably assumes $\sigma_{VX} = \sigma_{Xp} = 2\sigma_{XX}$ for the inelastic diffractive cross sections [26]. It also uses the fraction of diffractive events measured in the nondiffractive-like data sample (see Section 11.4.2), for which it determines an acceptance of

$$A^{FCAL>1}_{diffractive} = 67 \pm 8\ \%. \tag{11-6}$$

As stated in Section 11.2.2, the efficiency of the CFLT has been ignored up until this point. The correction factors for the efficiency of the CFLT acceptance of photon and double diffractive events is $\Delta^X_{CFLT} = -3 \pm 1\ \%$ and that of elastic and proton diffractive events is $\Delta^X_{CFLT} = -12 \pm 6\ \%$ [77]. These correction factors and the refinements in the analysis of [77] determine the acceptance in CAL of the diffractive-like data sample as $A^{FCAL<1} = 46 \pm 8\ \%$. Taking this value and the event count of Table 10-4 results in

$$\frac{N^{FCAL<1}}{A^{FCAL<1}} = \frac{879 \pm 59}{46 \pm 8\ \%} = 1922 \pm 129\ (\text{stat.}) \pm 332\ (\text{syst.}), \tag{11-7}$$

for the number of events with $E_{FCAL} < 1$ GeV, after correcting for the CAL acceptance.

11.4.2 The Nondiffractive-like Events

For a nondiffractive-like event, the energy deposited in FCAL has little to no correlation with that deposited in BCAL[77]. Therefore, the E_{FCAL} and E_{BCAL} distributions have been used to best fit the accepted simulated events to the data sample.

Proton diffractive events from PYTHIA (see Section 11.3.1) have been added to each of the three models of nondiffractive processes outlined in Section 11.3.2. Within the resolution of the χ^2 fit to the E_{FCAL} and E_{BCAL} distributions, proton diffraction has been verified to be representative of photon and double diffraction which may also have $E_{FCAL} > 1$ GeV (see Table 11-1). The acceptance for the diffractive events in the nondiffractive-like sample is given in (11-6).

The results of the fit, given in Table 11-4, are the fraction of accepted simulated events due

simulated sample	fraction [%]	$A^{FCAL>1}$ [%]	χ^2				
			FCAL	BCAL	RCAL	E_T	Avg.
soft + PYTHIA.1.8 + diff.	16 + 70 + 14	85	3.4	3.2	2.6	9.1	4.6
soft + PYTHIA.2.0 + diff.	21 + 66 + 13	86	2.3	2.1	3.8	8.1	4.1
soft + HERWIG.1.5 + diff.	21 + 73 + 6	83	2.5	8.0	5.5	3.0	4.8
soft + HERWIG.1.7 + diff.	20 + 73 + 7	83	3.0	5.8	6.6	2.2	4.4
soft + HERWIG.2.0 + diff.	32 + 62 + 6	84	3.3	4.7	3.9	2.0	3.5
PYTHIA.min.bin + diff.	92 + 8	86	2.6	2.8	3.2	2.3	2.7
HERWIG.min.bin + diff.	100 + 0	95	1.3	3.9	2.2	1.0	2.1

Table 11-4 Descriptions of the nondiffractive-like data sample.

The individual processes of the samples are described in Section 11.3.2.
The diff. process refers to the proton diffractive events described in the text.

to the different processes in each model. The values of χ^2 are determined for the E_{RCAL} and E_T distributions, but are not used in the fit.

The best fit to the data sample, shown in Figure 11-6, results from the PYTHIA and HERWIG minimum bias generators. Photon-proton interactions are thus very similar to hadron-hadron interactions.

The models which describe photoproduction in terms of a soft and a hard component generally result in poorer fits to the data sample than those of the minimum bias generators. The resulting large fraction of events due to the hard processes (62 – 73 %) is due to the relatively low p_T^{min} used in their generation, which yields relatively soft events. The large fraction of hard processes favored by the fit thus does not indicate a large difference between γp and πp processes.

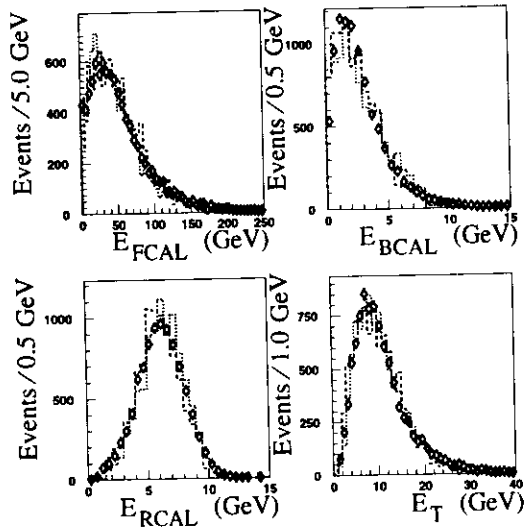

Figure 11-6 Energy distributions in CAL for the nondiffractive-like data sample.
The data sample (diamonds) compares well with the simulated samples from the HERWIG (dotted) and PYTHIA (dashed) minimum bias event generators. The PYTHIA sample also contains an explicit 8 % fraction of diffractive events (see Table 11-4).
The E_{FCAL} distribution for these nondiffractive-like events is well separated from the diffractive-like events with $E_{FCAL} < 1$ GeV.
The energies displayed are not corrected for the inactive material in front of the calorimeter, nor for particles escaping down the beam pipe.

From the fits, 6 – 14 % of the nondiffractive-like data sample is due to diffractive events. As described in Section 11.3.2, the HERWIG minimum bias generator implicitly includes diffractive events, hence the lack of an explicit diffractive component in the result of the fit.

Table 11-4 also shows the acceptance in CAL for each model, as calculated using the fractions of processes determined by the fit, the acceptances in Table 11-3 for the nondiffractive processes and the acceptance for the diffractive process in (11-6). For example, for the first model in Table 11-4,

$$\frac{1}{A^{FCAL>1}} = \frac{0.16}{0.89} + \frac{0.70}{0.90} + \frac{0.14}{0.65} = \frac{1}{0.85}. \qquad (11\text{-}8)$$

The first five examples in Table 11-4 of nondiffractive-like event simulation, using a combination of soft and hard components, show the effect on $A^{FCAL>1}$ under various assumptions for the mini-jet model. The five examples result in very similar values for $A^{FCAL>1}$. As a whole, they should probably treated with the significance attached to each of the results from the two minimum bias generators. Especially since the minimum bias generators, based on two different principles, both provide for a better description of the data, as seen by the χ^2 values in Table 11-4. Accommodating the range of values given in Table 11-4, the acceptance in CAL of the nondiffractive-like data sample is $A^{FCAL>1} = 89 \pm 6\ \%$.

As for the diffractive-like sample, the efficiency of the CFLT trigger thresholds has been ignored up until this point. The correction factor for the efficiency of the CFLT acceptance for the nondiffractive-like data sample is $\Delta_{CFLT} = -2 \pm 1\ \%$ [77], resulting in $A^{FCAL>1} = 87 \pm 6\ \%$. The event count in Table 10-4 provides

$$\frac{N^{FCAL>1}}{A^{FCAL>1}} = \frac{4852 \pm 72}{87 \pm 6\ \%} = 5577 \pm 83\ (\text{stat.}) \pm 385\ (\text{syst.}). \qquad (11\text{-}9)$$

for the number of events with $E_{FCAL} > 1$ GeV, after correcting for the CAL acceptance.

12 Radiative Corrections

The cross section for the interaction of particles is usually given for just the Born term. This provides considerable simplification, allowing experimental results to be easily compared and to be interpreted with respect to theory. In order to describe the interaction completely, higher order terms are required in addition to the Born term. Some of the higher order terms involve the radiation of a photon. In order to extract the Born term, the measured cross section has to be corrected for the higher order terms. This procedure is called radiative corrections.

12.1 Beyond the Born Term for Electron-Proton Scattering

In addition to the Born term, shown in Figure 2-1, ep scattering occurs via higher order terms; examples are given in Figure 12-1. This chapter will focus on the corrections at the lepton vertex, although other terms that can be safely neglected will first be addressed.

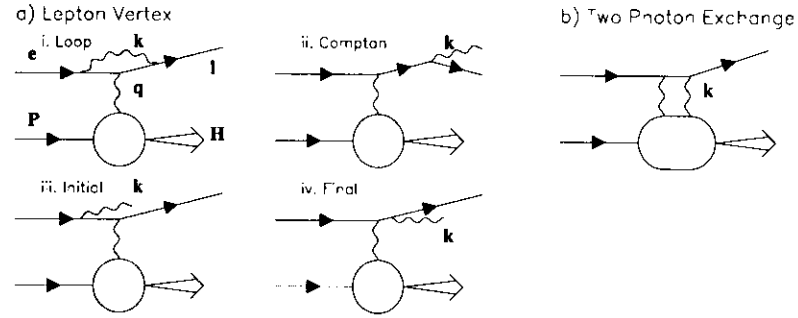

Figure 12-1 Examples of higher order terms for ep scattering.
In addition to the particles, e, P, l, q and the final hadronic state H of the Born term (see Section 2.1), higher order terms can involve additional photons, denoted k in the diagrams.
a) *Radiative corrections at the lepton vertex include:*
i. Virtual photon loops.
ii. Compton scattering dominantly at $Q^2 \approx 0$,
where the electron 'scatters' from an almost real photon originating from the proton.
iii. (iv.) Photons emitted parallel or close to the incoming (outgoing) electron, so-called initial (final) state radiation.
b) *In higher order terms, the electron and proton may exchange more than one photon. The Born term uses the one-photon exchange (OPE) approximation.*

Only QED corrections are addressed. Corrections from the weak force are negligible for the low momentum transfer, $Q^2 \ll 1\ \text{GeV}^2$, of tagged photoproduction (see Section 2.3).

In analogy to QED radiative corrections, in principle one could talk of QCD radiative corrections, for example the emission of a gluon from a quark. In practice, QCD corrections are folded into the description of the photon-proton vertex and the final hadronic system.

Figure 12-1 does not include examples of higher order terms with an additional photon at the proton vertex. These terms can be neglected for low Q^2 ep scattering since radiative corrections decrease with increasing mass of the fermion and $m_e/m_p \sim 1/1836$. This argument begins to break down for deep inelastic scattering at higher Q^2 where the parton content of the proton is involved in the collision, although radiative corrections at the lepton vertex continue to dominate.

A critique of the one-photon exchange (OPE) approximation is given in [4]. Two measurements can be used to verify the approximation. Firstly, if the two photon contribution is significant, the e^-p and e^+p cross sections are not equal. A measurement at $0.5 < Q^2 < 20\ \mathrm{GeV}^2$ showed no indication of two photon exchange at the one or two percent level. The measurement can also be made at HERA, in its entire accessible Q^2 range including photoproduction, once data is available from the planned e^+p operation. The OPE provides the dependence of the cross sections on W, Q^2 and ϑ_l. At a given W and Q^2, the differential cross section should fall on the line $A + B\tan^2(\vartheta_l/2)$ where A and B are measurements of the transverse and longitudinal components of the cross section at that W and Q^2. The second validation of the OPE searches for deviations from the above linear relationship. The measurement is difficult and requires data from several beam energies. Until evidence for a sizable contribution due to two photon exchange is found, it is justifiably neglected in ep analyses, including this one.

12.2 The Radiative Terms

The calculation of radiative corrections at the lepton vertex involves much more than just the four diagrams of Figure 12-1 a). Infrared divergencies, self-energies and interferences have to be correctly treated. Nevertheless, the description of the emitted photons as Compton, initial and final is justified [87]. The radiative cross section is dominated by the term

$$\frac{I}{k\cdot e} + \frac{F}{k\cdot l} + \frac{C}{q^2}, \qquad (12\text{-}1)$$

where I, F and C are slowly varying functions of the kinematic variables.

Initial and final state photon emission thus peaks as $k\cdot e \to 0$ and $k\cdot l \to 0$, respectively. Therefore, the photons are soft, their distribution peaks as $k \to 0$, and they are collinear with the incoming and outgoing electrons, since the respective dot products are then minimized.

Compton scattering dominates as $q^2 \to 0$. Since $e - l = q + k$, the result is $k \to e - l$. Therefore, the exchanged photon has minimal energy, while the hard emitted photon carries most of the energy difference between the incoming and outgoing electron.

For tagged photoproduction, the scattered electron, and thus nearly all the radiated photons, are nearly collinear with the incoming electron. The exchanged and radiated photons share the energy from the scattering of the electron. The radiative cross section has the property

$$\sigma_{\text{radiative}}(q = a, k = b) \approx \sigma_{\text{radiative}}(q = b, k = a), \qquad (12\text{-}2)$$

where energy and momentum conservation requires $e - l = a + b$. The exchanged photon is almost real and thus the lepton vertex is indifferent to which of the two photons is the exchanged photon and which is the radiated photon. This is demonstrated in Figure 12-2, using the Monte Carlo sample of events described in Section 12.8. Despite the fact that the proton vertex is involved in

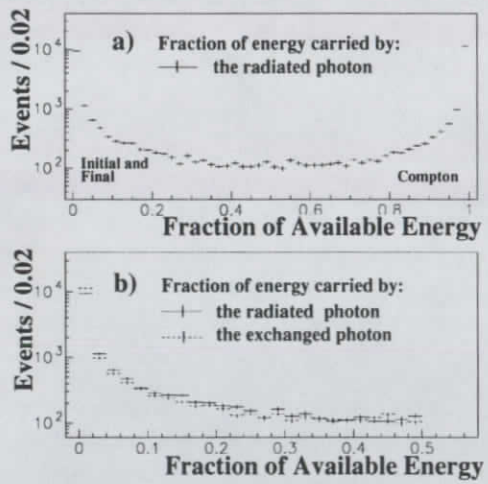

Figure 12-2 Symmetric energy distributions for the exchanged and radiated photon.
For radiative events in low Q^2 inelastic ep scattering, the energy made available by the scattered electron, $E_e - E_l$, is distributed nearly symmetrically between the radiated and the exchanged photon. Only radiated photons with $E_k > 0.35$ MeV are included in the distribution, since this energy requirement is implicit for the exchanged photons of inelastic ep scattering at HERA.

a) *The distribution of radiated photons shows the peak due to the initial and final state radiation along with the peak due to the Compton term.*

b) *The exchanged photon carries the remaining fraction of energy.*
Folding the distribution in a) at 0.5, shows the roughly symmetric energy distribution between the radiated and the exchanged photon.
The symmetry is not exact due to the virtuality of the exchanged photon and the neglected energy dependence of the photon-proton cross section.

The error bars are due to the statistics of the Monte Carlo sample described in Section 12.8.

the events, the demonstration succeeds because the photon-proton cross section has little dependence on the photon energy. In addition, inelastic photon-proton collisions require a minimum a center of mass energy of $m_p + m_\pi = 1.072$ GeV. The exchanged photon energy must therefore be at least 0.35 MeV in the collision with an 820 GeV proton at HERA. The 0.35 MeV requirement must also be imposed on the radiated photon to demonstrate the approximate symmetry.

12.3 Radiative Corrections

The cross section including the higher order corrections is denoted as the **complete** cross section. It is the theoretical model of the experimentally measured one. Radiative corrections are the difference between the Born and complete cross section.

The difference is expressed by the radiative corrections factor η defined by

$$\eta \equiv \frac{\sigma_{\text{Born}}^{\text{theory}}}{\sigma_{\text{complete}}^{\text{theory}}} \text{ and used as } \sigma_{\text{Born}}^{\text{measured}} = \eta\sigma^{\text{experiment}} \qquad (12\text{-}3)$$

in order to estimate the Born cross section using the experimental data [88]. The accuracy of η obviously depends on the description of the experiment used to determine $\sigma_{\text{Born}}^{\text{theory}}$ and $\sigma_{\text{complete}}^{\text{theory}}$, the theoretically expected cross sections in the apparatus for the Born term and for the complete terms.

The radiative corrections factor is often given in terms of δ, defined as

$$\eta^{-1} \equiv 1 + \delta, \text{ such that } \delta = \frac{\sigma_{\text{complete}}^{\text{theory}}}{\sigma_{\text{Born}}^{\text{theory}}} - 1 \text{ and } \sigma_{\text{Born}}^{\text{measured}} = \frac{\sigma^{\text{experiment}}}{1+\delta}. \qquad (12\text{-}4)$$

12.4 Radiative Corrections for Tagged Photoproduction

For low Q^2 ep scattering, only QED radiative corrections at the lepton vertex need be considered in addition to the Born term. The corrections have two effects for the measurement of tagged photoproduction in ep collisions.

The EPE, derived in Chapter 2, is based only on the Born term. The complete terms are required for an exact description of the flux of photons accompanying the electron. This is the first effect.

For non-radiative events, the definition $q \equiv e - l$ allows the exchanged photon to be tagged by the electron. The second effect of radiative corrections is the introduction of uncertainty about the exchanged photon if it is tagged only by the scattered electron. The emitted photon, k, of the radiative events causes the momentum of the exchanged photon to be given by $q = e - l - k$.

For the complete cross section, the scattered electron is insufficient to definitively tag the exchanged photon.

12.5 Avoiding the Higher Order Terms

The final result of the tagged photoproduction measurement is expressed in terms of the Born cross section. The best possible measurement should result by using only events due to the Born term. To the greatest extent possible, the events of the higher order terms should be excluded from the measurement. Although events due to the non-radiative higher order terms cannot be distinguished from those of the Born term, the radiative events can to some extent be recognized. Their exclusion from the measurement minimizes the effect of radiative corrections.

The double differential cross section for the scattered electron, in the region of acceptance of the LUMI electron calorimeter (LUMIE) as described in Section 7.2.1, has radiative corrections of $1 \lesssim \delta \lesssim 40$ % depending on y and Q^2 [89]. Such a measurement, using only the scattered electron information, includes events from all terms, demonstrating that the higher order terms are comparable in magnitude to the Born term in some regions of phase space.

The radiative events are most obviously recognized by observing the emitted photon. For low Q^2 ep collisions, the emitted photons are collinear with the incoming electron as described in Section 12.2. Therefore at ZEUS, the emitted photons have a high acceptance in the LUMI photon calorimeter (LUMIG). In fact, the photoproduction event sample of this thesis already has a cut involving the energy observed in LUMIG (E_{LUMIG}). The cut removes the accidental coincidence background and is described in Section 10.4.3 and is shown in Figure 10-4. The effectiveness of the E_{LUMIG} cut to minimize the radiative corrections obviously depends on the LUMIG acceptance for the emitted photons.

The momentum of the exchanged photon is also defined by $q \equiv P - H$, using the incoming proton and the outgoing hadronic system. In the kinematic domain of this thesis, this definition is not practical to measure the exchanged photon using the central detector. For tagged photoproduction, however, requirements for the hadronic system can restrict the phase space of the emitted photon by the relation $P - H = e - l - k$. In fact, the radiative corrections to the photoproduction event sample already benefit from such a restriction. The photoproduction event sample contains only events with $E_{\text{RCAL}} > 700$ MeV. As described in Chapter 9, this cut rejects most backgrounds, while accepting most photoproduction events. From energy and momentum conservation, the RCAL energy requirement effectively requires the energy of the exchanged photon to be $E_q \gtrsim 700$ MeV. Therefore, for a given tagged scattered electron, l, the emitted photon, k, has its energy roughly restricted by $E_l + E_k < E_e - 0.7$ GeV.

The LUMIG and RCAL requirements described above for the photoproduction sample will be referred to in the remainder of this chapter as the **experimental conditions**. As will be shown below, they are well suited to minimizing the radiative corrections, by rejecting radiative events. Obviously all non-radiative events will satisfy the conditions.

12.6 Determining the Radiative Corrections

Radiative corrections on low Q^2 ep scattering can be factored into their effects on the 'outgoing' particles at the lepton vertex, the exchanged photon and the scattered electron. A Monte Carlo simulation of the emitted photons introduced by the radiative corrections can be compared to their measurement in order to corroborate the calculation of the complete terms. The corrections have to be determined using the best possible description of the experiment.

Radiative corrections may be determined with two techniques. The analytical formulae for the cross section as given by the Born term and as given by the complete terms may be compared in a given region of phase space. For experimental measurements, this comparison is usually of limited use. The expressions are difficult to solve analytically, since the proton vertex is described by parametrization and the desired region of phase space may require complicated functions of the kinematic variables. More importantly, experiments and their measurements cannot usually be well described in terms of analytic functions. Therefore, the radiative corrections determined are only as accurate as the estimated description of the experiment.

The second and more powerful technique follows the Monte Carlo method, generating events according to the full differential cross section within the kinematic boundaries of interest. By generating an event sample according to the Born term and a sample according to the complete terms, the radiative corrections for any distribution in any region of phase space may be examined. More importantly, the generated events can be passed through simulation code describing the complete experiment. In this way, the effect of radiative corrections on any measurement can be determined.

12.7 Results from a Previous Study

Radiative corrections to the total photoproduction cross section measurement at ZEUS have been estimated previously by Charchula and Gajewski in [89]. A short summary of this CG study and its results is given here along with two comments.

Two computer programs were used to determine the results independently. The ALLM [17] parametrization for $\sigma_{T,L}^{\gamma^* p}(y, Q^2)$, the transverse and longitudinal double differential virtual photon proton cross section, was used in both programs to describe the photon-proton vertex. TERAD91 [90] is a semi-analytical program based on formulae obtained analytically. HERACLES4.2 [91] is a Monte Carlo event generator following the full differential cross section. Both

of these programs originated for the study of radiative corrections to deep inelastic ep scattering, that is, for $Q^2 \gg 1\ \mathrm{GeV}^2$, where their results have been extensively and successfully compared. The programs were modified, by their respective authors, to extend their range of validity to the photoproduction region. The CG study shows that the two programs agree in the photoproduction region. This provides confidence in the correctness of the programs in this region.

The kinematic domain of the CG study is

$$10 \le E_l \le 16\ \mathrm{GeV} \text{ and } Q^2 \le 1.5\times10^{-2}\ \mathrm{GeV}^2, \qquad (12\text{-}5)$$

covering the range of scattering angles of electrons accepted by LUMIE (see Section 7.2.1). The requirement $Q^2 \ge Q^2_{min}$ is implicit.

LUMIG is assumed to be able to detect all emitted photons with energy $E_k \ge 0.5$ GeV and scattering angle $\vartheta_k \le 0.5$ mrad. The central detector is assumed to accept only events with a final hadronic system satisfying $W \ge 60$ GeV. Although not explicitly stated in the paper, the cut on W corresponds to the condition $E_q \ge 1.1$ GeV for the energy of the exchanged photon. This cutoff value for the exchanged photon was chosen following the argument given in Section 12.5, except that the requirement on E_{RCAL} is $E_{RCAL} > 1.1$ GeV rather than 0.7 GeV. This cut was used in the first measurement of the total photoproduction cross section at ZEUS [14].

If LUMIG is used to reject radiative events, according to the acceptance given above, and if the central detector accepts only events with $W \ge 60$ GeV, the radiative corrections are shown to be a constant $\delta = -1$ % across the range of E_l given in (12-5).

Also under the above conditions, for a scattered electron with energy $E_l = 13.6$ GeV, the radiative corrections are shown to be restricted to $-4 \le \delta \le 0$ % for any point in the Q^2 range of (12-5). Similar behavior is reported for the entire E_l range of (12-5). The LUMIE acceptance varies steeply with Q^2. Although not explicitly stated in the CG paper, the determination of only a slight Q^2 dependence for the radiative corrections permits the implicit assumption of the study that the acceptance of the scattered electron is not affected by radiative corrections.

12.8 Studying the Lepton Vertex with the Luminosity Monitor

The outgoing particles at the lepton vertex of low Q^2 ep scattering, the scattered electron and the occasional emitted photon, may be observed in LUMIE and LUMIG, respectively. The ZEUS detector simulation program MOZART was used to determine the radiative corrections to this measurement. In contrast to the CG study, with its assumptions and rough parametrization of the detector, the radiative correction are directly determined, within the validity of MOZART. The

predicted spectra of radiative photons observed in LUMIG were also determined and are presented in Section 12.9 in a comparison with the data.

It was not necessary to simulate the final hadronic system of the ep collision. As in the CG study, the central detector was assumed to accept only events with a minimum energy for exchanged photon, $E_q \geq E_q^{min}$.

The events were generated with HERACLES4.1 [92] modified by the authors to extend its range of validity to the photoproduction region. Similar to the CG study, the events are within the kinematic region

$$4.4 < E_l < 22.2 \text{ GeV and } x < 1.08 \times 10^{-6}, \qquad (12\text{-}6)$$

with ALLM describing the virtual photon-proton interaction. While HERACLES4.2 does, HERACLES4.1 unfortunately does not include the Q^2_{min}/Q^2 term of the EPE (see Section 4.5). The omission of this term is assumed not to significantly influence the validity of the results presented here. For example, the HERACLES4.1 events do reproduce the results of the CG study which used HERACLES4.2.

Results in this subsection are presented for the kinematic region used to determine the total cross section. The electron energy measured in LUMIE (E_{LUMIE}) is in the range $15.2 < E_{LUMIE} < 18.2$ GeV. The entire E_l range of (12-6) exhibits similar behavior. As described in Section 12.5, many of the radiative events do not survive the experimental conditions. This leads to small radiative corrections,

$$\delta = -0.2\ \% \text{ for } 15.2 < E_{LUMIE} < 18.2 \text{ GeV}. \qquad (12\text{-}7)$$

The radiative corrections dependence on the observed LUMIE energy and on three generator level variables is shown in Figure 12-3. The four distributions demonstrate that the corrections are not disturbingly large in any part of the various kinematic regions.

The effect of an explicit $E_{LUMIG} < E^{max}_{LUMIG}$ cut is shown in Figure 12-4. For the photoproduction events of the total cross section measurement (see Section 10.7),

$$\delta = -1.8\ \% \text{ for } E^{max}_{LUMIG} = 1 \text{ GeV}. \qquad (12\text{-}8)$$

The cut also removes non-radiative events which accidentally coincide with energy deposited by bremsstrahlung photons into LUMIG, the so-called a.c.-tagged events described in Section 10.4.4. The additional fraction of a.c.-tagged events expected to be lost is $-2.6 - -0.9 = -1.7$ % from Figure 10-8. The expected total change in the number of events due to $E^{max}_{LUMIG} = 1$ GeV of $-1.7 - (1.8 - 0.2) = -3.3$ % agrees well with the observed value of $(5731 - 5959)/5959 = -3.8$ % (see Table 10-4). The disagreement of $3.8 - 3.3 = 0.5$ % is

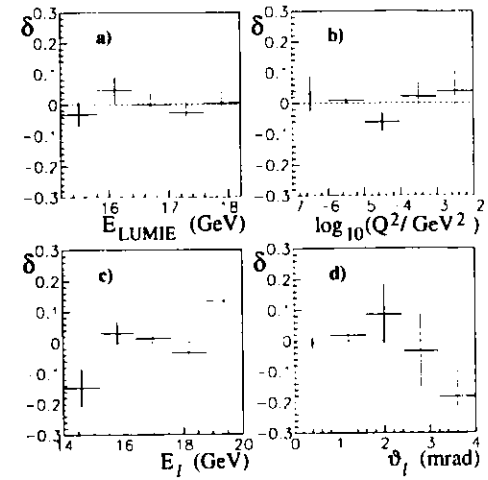

Figure 12-3 Radiative corrections for tagged electrons.
The corrections are for electrons measured in LUMIE with $15.2 < E_{LUMIE} < 18.2$ GeV *from events satisfying the experimental conditions described in Section 12.5.*
The expected effect of radiative corrections is shown for one measurement:
a) E_{LUMIE}, *the energy of the scattered electron measured in LUMIE.*
and for 3 variables, available from the event generator, describing the event:
b) Q^2, *the momentum transferred by the exchanged photon.*
c) E_l, *the energy of the scattered electron.*
d) ϑ_l, *the angle of the scattered electron.*

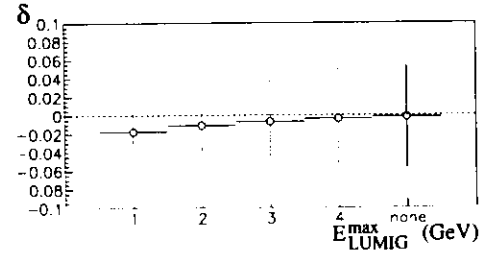

Figure 12-4 Dependence of radiative corrections on the observed radiated photons.
The effect on δ *from a cut* $E_{LUMIG} < E^{max}_{LUMIG}$, *in addition to the experimental conditions.*
The point labelled "none" shows δ *without any additional LUMIG cut.*

used as the error on δ in (12-8). The indication that more events are lost in reality to radiative corrections than is calculated here, agrees with the expectations of the following paragraph.

The experimental conditions require $E_{RCAL} > 700$ MeV and implicitly that the event has been triggered. The acceptance of the event in the central detector by the trigger and event selection, as described in Chapter 9, depends on the exchanged photon energy. This dependence has been ignored in determining the radiative corrections. All events with exchanged photon energy $E_q \geq E_q^{min}$ have been assumed to have been accepted. In Figure 12-5 the radiative corrections show only a slight dependence on E_q^{min}. Therefore, for the results presented here, the $E_q \geq 700$ MeV requirement is a sufficiently accurate description of the experimental conditions for the outgoing hadronic system. In reality E_q^{min} must be effectively higher, such that δ (see Figure 12-5) must decrease. A more accurate determination of the radiative corrections would require the hadronic system of the ep collision to be generated for radiative events and processed through the detector and trigger simulation programs.

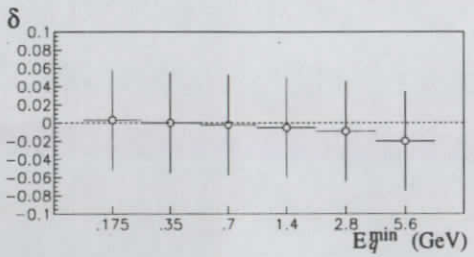

Figure 12-5 Dependence of radiative corrections on the exchanged photons.
The dependence of δ *on the minimum exchanged photon energy requirement,* $E_q \geq E_q^{min}$, *of the experimental conditions.* $E_q^{min} = 700$ MeV *is the default value.*
If the condition $E_{LUMIG}^{max} = 1$ GeV *is applied, the shape of the distribution is not changed, but* δ *in each bin is reduced by approximately* 1.6 %.

12.9 The Measured and Predicted LUMIG Energy Distribution

The measured E_{LUMIG} distribution of the photoproduction event sample, presumably due to radiative events was determined in Section 10.4.4 and is shown in Figure 10-9. The theoretical expectation for the distribution is determined using the Monte Carlo event sample described in the preceding section. The data and the expected distributions are presented in Figure 12-6 for comparison. The value in the second bin, with $0.4 < E_{LUMIG} < 1.2$ GeV, is not reliable due to the treatment of the ADC_{LUMIG} pedestal (see Section 10.4.4.2). A minor caveat is that for such low energy photons, the effect of the synchrotron radiation absorbers in front of LUMIG may not be ideally simulated in MOZART. While the errors associated with the data are large, the distributions are in good agreement. This provides strong confidence in the correctness of the theoretical input, including HERACLES and MOZART, in determining radiative corrections within the experimental conditions.

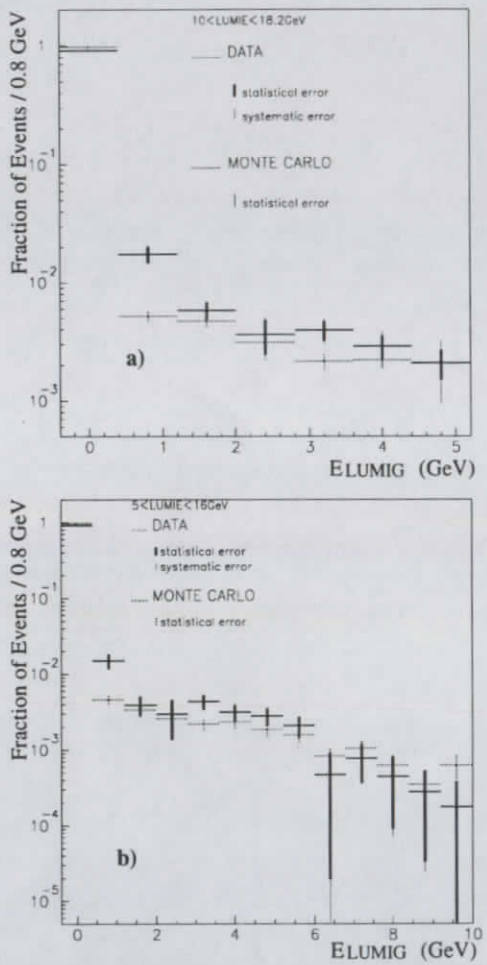

Figure 12-6 The measured and the predicted LUMIG energy distribution.
The distribution marked DATA is the result presented in Figure 10-9. The distribution marked MONTE CARLO (MC) is determined from the event sample described in Section 12.8, using events meeting the experimental requirements described in Section 12.5. The errors on the MC prediction are statistical. Two regions of energy in LUMIE are shown:
a) $10 < E_{LUMIE} < 18.2$ GeV *and* **b)** $5 < E_{LUMIE} < 16$ GeV.

12.10 Summary

A detailed detector simulation shows that the radiative corrections are $\delta = -1.8 \pm 0.5$ % for the tagged photoproduction sample of the total cross section measurement. The accuracy of this result should not be significantly affected by the lack of a detailed simulation for the outgoing hadronic system. The effect of introducing a maximum allowed LUMIG energy is presented and corroborated by the data. Within the allowed kinematic region, the distribution of tagged photoproduction events, as determined by the Born term and the experimental conditions, is not significantly changed by radiative corrections. The expected energy distribution in LUMIG due to radiative events agrees with the measurement.

13 The Total Photoproduction Cross Section

Table 13-1 summarizes the values determined in the previous chapters for the terms of (1-4), the expression for the measured electron-proton cross section. The measured total cross section for ep interactions with $Q^2 \leq 0.02$ GeV^2 and $167 < W < 194$ GeV is

$$\sigma^{ep}_{\text{measured}} = 830 \pm 17 \text{ (stat.)} \pm 102 \text{ (syst.) nb}. \qquad (13\text{-}1)$$

	see	stat. error [%]	syst. error [%]
$N^{\text{FCAL<1}}/A^{\text{FCAL<1}} = 1922 \pm 129 \pm 332$	(11-7)	1.7	4.4
$N^{\text{FCAL>1}}/A^{\text{FCAL>1}} = 5577 \pm 83 \pm 385$	(11-9)	1.1	5.1
$A_{\text{LUMIE}} = 77 \pm 7$ %	(8-4)		9.2
$L_{\text{int}} = 12.66 \pm 0.54$ nb^{-1}	(10-1)		4.3
$\delta = -1.8 \pm 0.5$ %	(12-8)		0.5
$\Delta = -5.6 \pm 0.7$ %			0.7
from: $\Delta_{\text{reconstruction}} = -1.1 \pm 0.1$ %	(10-4)		
$\Delta_{\text{trigger}} = -0.7 \pm 0.1$ %	(10-15)		
$\Delta_{\text{selection}} = -1.0 \pm 0.3$ %	(10-16)		
$\Delta_{\text{a.c.-tagged}} = -2.9 \pm 0.6$ %	(10-19)		

Table 13-1 Summary of the electron-proton cross section measurement.

The contribution of each term to the error of $\sigma^{ep}_{\text{measured}}$ *is shown in the last two columns. The terms correspond to* $15.2 < E_{\text{LUMIE}} < 18.2$ GeV, $E_{\text{LUMIG}} < 1$ GeV, *and* $Q^2 \leq 0.02$ GeV^2.

The total photoproduction cross section is given by (1-5) as $\sigma^{\gamma p}_{\text{tot}} = \sigma^{ep}_{\text{measured}}/F^{e}_{\gamma}$. For the y range of this measurement, $\sigma^{\gamma p}_{\text{tot}}$ and the acceptance for the ep events have only a small y dependence which can be neglected. Therefore, (4-8) simply provides

$$F^{e}_{\gamma} = \frac{\alpha}{2\pi} \int_{y_{min}}^{y_{max}} dy \frac{1+(1-y)^2}{y} \ln \frac{Q^2_{max}}{Q^2_{min}} - \frac{2(1-y)}{y} \left(1 - \frac{Q^2_{min}}{Q^2_{max}}\right), \qquad (13\text{-}2)$$

The range of measured scattered electron energies, $15.2 < E_{\text{LUMIE}} < 18.2$ GeV, provides y_{min} and y_{max}. $Q^2_{max} = 0.02$ GeV^2 corresponds to that used to determine the acceptance of the scattered electron in LUMIE. Q^2_{min} is the kinematic limit discussed in Section 2.2. Performing the integration results in $F^{e}_{\gamma} = 0.005818$.

Therefore, the total photoproduction cross section for $167 < W < 194$ GeV is

$$\sigma^{\gamma p}_{\text{tot}} = 143 \pm 3 \text{ (stat.)} \pm 18 \text{ (syst.) } \mu\text{b}. \qquad (13\text{-}3)$$

14 Conclusions and Outlook

The results of this thesis provide an important new measurement of the total photon-proton cross section at high energy. The measurement is consistent with the original measurements by ZEUS[14] and H1[15] and with the recent new measurement by H1[93], as shown in Figure 14-1.

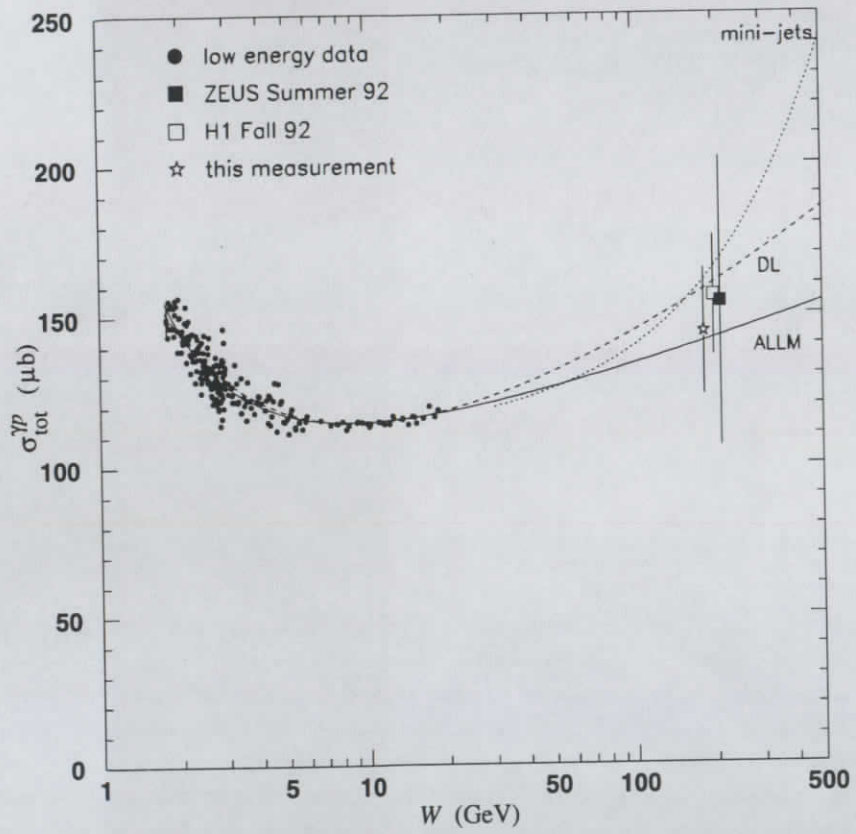

Figure 14-1 Total photon-proton cross section as a function of center of mass energy. *The measurements at low energies [4] (full circles) are shown with the original measurement by ZEUS (closed square) and the recent new measurement by H1 (open square). Also shown are the predictions of the DL [16][6] (dashed line) and ALLM [17] (solid line) parametrizations as well as a minijet model prediction (dotted line, see Sections 3.2.4 and 3.3) using* $p_T^{\min} = 2$ GeV *and the DG [83] parametrization of the photon structure function.*

With a much smaller error than the original ZEUS measurement, the present measurement has benefitted from:

- the use of the correct photon flux (see Section 4.5).
- a detailed treatment of the electron acceptance in LUMIE (see Section 8.2.4).
- a significantly different trigger for the final hadronic system with a larger acceptance (see Section 9.5).
- a much larger event sample (see Section 10.7).
- a complete treatment of backgrounds and inefficiencies (see Chapter 10).
- a detailed treatment of the acceptance of the final hadronic system in CAL (see Chapter 11).
- the experimental corroboration of the radiative corrections (see Section 12.9).

This thesis provides two strong indications that the dominantly hadronlike behavior of the photon in γp interactions extends up to $W \sim 180$ GeV. Firstly, the final hadronic system observed in CAL can be well represented by the Monte Carlo event generators of hadron-hadron physics (see Chapter 11). Secondly, the agreement of $\sigma_{\text{tot}}^{\gamma p}$ with the Regge theory based predictions of DL [16] and ALLM [17], as shown in Figure 14-1, indicates that γp interactions up to $W \sim 180$ GeV have a total cross section behavior similar to that of hadron-hadron interactions.

Also seen in Figure 14-1 is an example of the ability of mini-jet models [18][35][94] to accommodate the $\sigma_{\text{tot}}^{\gamma p}$ measurement. Although the HERA result is able to constrain the mini-jet model parameter $p_T^{\min} \gtrsim 1$ GeV [94] and may be able to constrain the parton distributions of the photon [18], detailed studies of the hadronic final state are required to understand the mini-jet contribution to γp interactions [94]. Although this measurement definitely rules out a rapid rise for $\sigma_{\text{tot}}^{\gamma p}$, as permitted by the mini-jet models, it does not rule out a sizable minijet contribution to the total cross section. As argued in [95], an increase in the mini-jet contribution to the hadron-hadron total cross section is expected to be compensated by a reduction in the cross section of the other processes.

As seen in Table 13-1, a further improved measurement of $\sigma_{\text{tot}}^{\gamma p}$ will require an improved determination of the integrated luminosity, the acceptance of the scattered electron in LUMIE and the acceptance of the final hadronic system in CAL. Changes in the experimental setup of the luminosity monitor, some of which were in effect for 1993 data taking, are expected to eventually result in an accuracy of 2 % for the luminosity measurement [72]. The addition of the LUMIE position monitor for 1993 data taking (see Section 7.2.1) provides a powerful tool to further the understanding of LUMIE and its acceptance, allowing the error on A_{LUMIE} to be reduced. At the time of submission of this thesis, the 1993 running period of HERA has just finished, with ZEUS recording half a million photoproduction candidates. This huge data sample, measured with an

almost completely instrumented CTD, should allow γp interactions at HERA energies to become much better understood, placing constraints such as transverse momentum and multiplicity distributions on the event generators. The narrower range of descriptions of γp interactions will lead to smaller errors for the acceptance in CAL of the final hadronic system.

Due to the hadronic structure of the photon, photoproduction at HERA provides the highest energy hadron-hadron interactions for measurement, after proton-antiproton colliders. As ZEUS and H1 come to fully understand their detectors and observations, this new and unique experimental perspective will provide valuable input to the theory of hadronic interactions. Theories and models that at present can only be tested at proton-antiproton machines can also be tested in proton-vector meson collisions. In addition, results from HERA are awaited from all interactions with the proton involving the point-like photon, presently measured and understood for only the photoproduction of high p_T jets and for the high Q^2 photons of deep inelastic scattering. With the above results, HERA should help arrive at a coherent and complete explanation of the apparent duality of the photon as an extended hadron-like state and as a point-like particle.

15 References

[1] The ZEUS Detector, Status Report 1993, ed. U. Holm (Feb. 1993).

[2] H1 Collab., I. Abt et al., The H1 Detector at HERA, DESY 93-103 (1993).

[3] R. Brinkmann, DESY HERA 88-03 (1988).

[4] T. H. Bauer, R. D. Spital, D. R. Yennie, F. M. Pipken, *Rev. Mod. Phys.* **50** (1978) 261.

[5] P. D. B. Collins, *Introduction to Regge Theory*, Cambridge University Press (1977);
P. D. B. Collins, A. D. Martin, *Hadron Interactions* (Graduate Student Series in Physics), Adam Hilger Ltd, Bristol (1984).

[6] A. Donnachie, P. V. Landshoff, *Phys. Lett.* **B296** (1992) 227.

[7] D. O. Caldwell et al., *Phys. Rev. Lett.* **40** (1978) 1222.

[8] M. Samorski, W. Stamm, *Astrophys. J.* **268** (1983) L17;
M. Samorski, W. Stamm in *18th International Cosmic Ray Conference, Bangalore, India, 1983, Conference Papers*, ed. N. Durgaprusad et al., (Tata Institute of Fundamental Research, Bombay, 1983) Vol. 11, p. 244;
J. M. Bonnet-Bidaud, G. Chardin, *Phys. Rep.* **170** (1988) 325.

[9] B. L. Dingus et al., *Phys. Rev. Lett.* **61** (1988) 1906.

[10] T. Dzikowski, J. Gawin, B. Grochalska, J. Wdowczyk, *J. Phys. G: Nucl. Phys.* **9** (1983) 459;
S. Sinha et al., Tata Institute of Fundamental Research Report No. OG 4.6-23;
V. V. Alexeenko et al., presented at *III VHE Gamma Ray Astronomy Workshop, Crimea, U.S.S.R., 1989* (unpublished).

[11] T. C. Weekes, *Phys. Rep.* **160** (1988) 1;
J. A. Goodman, *Nucl. Phys. B (Proc. Suppl.)* **14A** (1990) 84.

[12] F. Halzen, E. Zas, *Nucl. Phys. B (Proc. Suppl.)* **14A** (1990) 60.

[13] J. C. Collins, G. A. Landinsky, *Phys. Rev.* **D43** (1991) 2847;
R. S. Fletcher, T. K. Gaisser, F. Halzen, *Phys. Rev.* **D45** (1992) 377, 3279 (Erratum);
J. R. Forshaw, J. K. Storrow, *Phys. Lett.* **B268** (1991) 116;
G. Schuler, J. Terron, CERN-TH.6415/92 (1992);
M. Drees, F. Halzen, *Phys. Rev. Lett.* **61** (1988) 275;
R. Ghandi, I. Sarcevic, *Phys. Rev.* **D44** (1991) 10.

[14] ZEUS Collaboration, M. Derrick et al., *Phys.Lett.* B293 (1992) 465.

[15] H1 Collab., T. Ahmed et al., *Phys. Lett.* B299 (1993) 469.

[16] A. Donachie, P. V. Landshoff, *Nucl. Phys.* **B244** (1984) 322;
P. V. Landshoff, *Nucl. Phys. B (Proc. Suppl.)* **18C** (1990) 211.

[17] H. Abramowicz, E. Levin, A. Levy, U. Maor, *Phys. Lett.* **B269** (1991) 465.

[18] K. Honjo et al., *Phys. Rev.* **D48** (1993) 1048.

[19] E. Fermi, Z. *Phys.* **29** (1924) 315.

[20] C. F. v. Weizsäcker, Z. *Phys.* **88** (1934) 612;
E. J. Williams, *Phys. Rev.* **45** (1934) 729.

[21] R. H. Dalitz, D. R. Yennie, *Phys. Rev.* **105** (1957) 1598.

[22] F. J. Gilman, *Phys. Rev.* **167** (1967) 1365.

[23] L. N. Hand, *Phys. Rev.* **120** (1963) 1834.

[24] J. J. Sakurai, *Phys. Rev. Lett.* **22** (1969) 981.

[25] G. A. Schuler, T. Sjöstrand, *Phys. Lett.* **B300** (1993) 169.

[26] G. A. Schuler, T. Sjöstrand, CERN-TH.6796/93 (1993).

[27] V. M. Budnev, I. F. Ginzburg, G. V. Meledin, V. G. Serbo, *Phys. Rep.* **15C** (1975) 181.

[28] V. N. Baier, V. S. Fadin, *Sov. Phys. JETP* **34** (1972) 253.

[29] W. D. Shambroom et al., *Phys. Rev.* **D26** (1982) 1.

[30] N. N. Achasov, V. A. Karnekov, *Sov. J. Nucl. Phys.* **38** (1983) 736.

[31] K. Goulianos, *Phys. Rep.* **101** (1983) 170.

[32] S. Levonian, Low and Medium p_T Photoproduction at HERA, in DESY 93-077 (1993).

[33] T. J. Chapin et al., *Phys. Rev.* **D31** (1985) 17.

[34] UA1 collab., C. Albajar et al., *Nucl. Phys.* **B309** (1988) 405.

[35] R. S. Fletcher, T. K. Gaisser, F. Halzen, *Phys. Lett.* **B298** (1993) 442.

[36] E. M. Levin, L. L. Frankfurt, A. F. Ioffe, *JETP Letters* **2** (1965) 65;
H. J. Lipkin, F. Scheck, *Phys. Rev. Lett.* **16** (1966) 71.

[37] E. Witten, *Nucl. Phys.* **B120** (1977) 189.

[38] F. M. Borzumati, G. A. Schuler, DESY 92-078 (1992).

[39] J. J. Sakurai, D. Schildknecht, *Phys. Lett.* **B40** (1972) 121.

[40] L. B. Bezrukov, E. V. Bugaev, *Sov. J. Nucl. Phys.* **32** (1980) 847.

[41] G. Shaw, *Phys. Rev.* **D47** (1993) R3676.

[42] WA69 Collab., R. J. Apsimon et al., Z. *Phys.* **C43** (1989) 63.

[43] WA69 Collab., R. J. Apsimon et al., Z. *Phys.* **C46** (1990) 35.

[44] WA69 Collab., R. J. Apsimon et al., Z. *Phys.* **C53** (1992) 581.

[45] ZEUS Collaboration, M. Derrick et al., DESY 93-151 (1993), submitted to *Phys. Lett.* **B**.

[46] A. I. Lebedev, in [49] p. 613.

[47] V. N. Gribov, V. A. Kolkunov, L. B. Okun, V. M. Shekhter, *Sov. Phys. JETP* **14** (1962) 1308.

[48] *Proceedings of the HERA Workshop*, ed. R. D. Peccei (**DESY**, Hamburg, 1987).

[49] *Proceedings of the Workshop "Physics at HERA"*, ed. W. Buchmüller, G. Ingelman (**DESY**, Hamburg, 1992).

[50] H1 Collab., I. Abt et al., DESY 93-100 (1993).

[51] B. Burow, Measuring the Total Photoproduction Cross-Section from Electron Proton Collisions using the Weizsäcker-Williams Approximation, ZEUS Note 93-081 (1993).

[52] A. Rostovtsev, V. Soloshenko, Corrections to the Weizsäcker-Williams Approximation of Photon Flux in ep Collisions, H1-08/93-309 (1993).

[53] J. I. Friedman, H. W. Kendall, *Ann. Rev. Nucl. Science* **22** (1972) 203.

[54] D. P. Barber et al., *NIM* **A329** (1993) 79.

[55] J.A. Crittenden, M. Nakahata, K. Piotrzkowski, Results of Analysis of the C5 Detector Time Distributions for the Fall 1992 Running Period. ZEUS Note 93-041 (1993).

[56] B. H. Wiik in [49] p.1.

[57] S. J. de Jong, The ZEUS Second Level Trigger: Physics Simulation, Design and Implemaentation, Ph. D. Thesis Univ. van Amsterdam (1990).

[58] W. Schott et al., The ZEUS Background Radiation Monitor (BRM), ZEUS Note 93-002 (1993).

[59] W. Smith et al., The ZEUS Trigger System, ZEUS Note 89-084.

[60] R. Brun, J. Zoll, ZEBRA User Guide, *CERN Computer Center Program Library* **Q100** (1987).

[61] S. M. Fisher, P. Palazzi, The ADAMO Data System Version 3.2 (1992).

[62] L. Köpke, The ZEUS Primer, ZEUS Note 93-006.

[63] B. Burow, ZA: ZA for Analysis, ZEUS Note 93-102 (1993).

[64] ZEUS Calorimeter Group, A. Andresen et al., *NIM* **A309** (1991) 101.

[65] ZEUS Barrel Calorimeter Group, M. Derrick et al., *NIM* **A309** (1991) 77.

[66] ZEUS Calorimeter Group, U. Behrens et al., *NIM* **A289** (1990) 115.

[67] U. Behrens et al., DESY 93-121 (1993).

[68] H1 Calorimeter Group, B. Andrieu et al., DESY 93-078 (1993).

[69] R. Yoshida, DESY 92-159 (1992).

[70] W. H. Smith et al., ZEUS Calorimeter First Level Trigger Operation, ZEUS Note 92-103 (1992).

[71] W. H. Smith et al., ZEUS Calorimeter First Level Trigger, ZEUS Note 89-085 (1989).

[72] K. Piotrzkowski, Experimental Aspects of the Luminosity Measurement in the ZEUS Experiment, Ph. D. Thesis, Institute of Nuclear Physics, Krakow, Poland (1993) available as Internal Report DESY F35D-93-06 October 1993.

[73] H. Bethe, W. Heitler, *Proc. Roy. Soc.* **A146** (1934) 83.

[74] R. L. Gluckstern, M. L. Hull, Phys. Rev. 90 (1953) 1026.

[75] J. A. Andruszkow et al., DESY 92-066 (1992).

[76] D. Bandyopadhyay, MUTRIG: A TLT Muon Finder, ZEUS Note 93-013 (1993).

[77] M. Krzyzanowski, ZEUS Note 93-XXX in preparation.

[78] H. Abramowicz et al., A Determination of F_2 with the 1992 Data, ZEUS Note 93-078 (1993).

[79] T. Sjöstrand, *Z. Phys.* **C42** (1989) 301;
H.-U. Bengtsson, T. Sjöstrand, *Comp. Phys. Commun.* **46** (1987) 43.

[80] B. R. Webber, *Ann. Rev. Nucl. Science* **36** (1986) 253;
G. Marchesini et al., *Comp. Phys. Commun.* **67** (1992) 465.

[81] N. N. Nikolaev, B. G. Zakharov, *Z. Phys.* **C53** (1992) 331.

[82] P. Bruni, G. Ingelman, A. Solano in [49] p.363;
A. Solano, STUDIO DI PROCESSI DIFFRATTIVI AD HERA,
Ph. D. Thesis, Università degli Studi di Torino, Facoltà di Scienze Matematiche, Fisiche e Naturali, Torino, Italy (1993).

[83] M. Drees, K. Grassie, Z. Phys. C28 (1985) 451.

[84] UA5 Collaboration, G. J. Alner et al., *Nucl. Phys.* **B291** (1987) 445.

[85] M. Kasprzak, Simulation of Non-diffractive Photoproduction Events, ZEUS Note 93-098 (1993).

[86] P. de Jong, Status of the Uranium Calorimeter Reconstruction Software, ZEUS Note 92-019 (1992).

[87] H. Spiesberger, *Nucl. Phys.* **B29A** (1992) 221.

[88] D. Bardin et al., *Nucl. Phys.* **B29A** (1992) 209.

[89] K. Charchula, J. Gajewski, DESY 92-173 (1992).

[90] A. Akhundov, D. Bardin, L. Kalinovskaya, T. Riemann in [49] p.1285.

[91] A. Kwiatkowski, H.-J. Möhring, H. Spiesberger, *Comp. Phys. Commun.* **69** (1992) 155.

[92] A. Kwiatkowski, H.-J. Möhring, H. Spiesberger in [49] p.1294.

[93] J. Dainton, in *Proceedings of the XVI International Symposium on Lepton and Photon Interactions at High Energy, Cornell U., Ithaca, New York, 1993*, (to be published).

[94] J. R. Forshaw, J. K. Storrow, M/C-TH 93/13 or RAL-93-030.

[95] M. Jacob, P. V. Landshoff, *Mod. Phys. Lett.* **A1** (1987) 766.

Glossary

Terms and acronyms frequently used in this presentation:		Introduced in Section:
EPE	equivalent photon expression	2.5
diffractive-like events	events with $E_{FCAL} < 1$ GeV	3.5
nondiffractive-like events	events with $E_{FCAL} \geq 1$ GeV	3.5
F1992	the fall 1992 running period of HERA	5
e-background	background created by the electron beam	5.3
p-background	background created by the proton beam	5.3
BCN	bunch crossing number	5.4
e-pilot bunch	electron bunch without an opposing proton bunch	5.4
p-pilot bunch	proton bunch without an opposing electron bunch	5.4
C5-background	p-background identified by C5	7.3
VW-background	p-background identified by the VW	7.4
a.c.-tagged	tagged photoproduction which accidentally coincides with bremsstrahlung in LUMIE and/or LUMIG	8.4
a.c.-background	background mistakenly identified as tagged photoproduction due to an accidental coincidence with bremsstrahlung in LUMIE	8.4
selected events	the sample of events resulting from the trigger and event selection	9
photoproduction sample	the sample after removing the background from the selected events	9
PTE	photoproduction trigger and event selection	9.1.4
e-accepted	bremsstrahlung with electron accepted in LUMIE	10.4.3
eγ-accepted	bremsstrahlung with electron accepted in LUMIE and photon accepted in LUMIG	10.4.3
recognized a.c.-background	a.c.-background identified by the bremsstrahlung energy in LUMIG	10.4.3
hidden a.c.-background	a.c.-background not identified due to the lack of bremsstrahlung energy in LUMIG	10.4.3
data sample	the events used to determine the acceptance in CAL of the final hadronic system	11.1

Names and acronyms associated with the ZEUS detector:		Introduced in Section:
IP	interaction point	6.1
CTD	central tracking detector	6.1
COIL	superconducting solenoid surrounding the CTD	6.1
CAL	high resolution calorimeter	6.1
FCAL / BCAL / RCAL	forward / barrel / rear part of CAL	6.1
VW	veto wall	6.1
C5	assembly of scintillation counters near the beam pipe behind RCAL	6.1
LUMIE	electron calorimeter of the luminosity monitor	6.1
LUMIG	photon calorimeter of the luminosity monitor	6.1
FLT / SLT / TLT	first / second / third level trigger	6.2
GFLT / GSLT	global FLT / SLT	6.2
ZEPHYR	the ZEUS event reconstruction program	6.3
MOZART	the ZEUS detector simulation program	6.5
ZGANA	the ZEUS trigger simulation program	6.5
EMC	electromagnetic section of CAL	7.1.1
HAC	hadronic section of CAL	7.1.1
CFLT	CAL FLT	7.1.4